EFFECT OF BUILD ORIENTATION OF ANISOTROPIC BEHAVIOR IN DIRECT ENERGY DEPOSITION BUILT COMPONENTS

A Thesis Presented to The Academic Faculty

By

Samuel L. Kersten

In Partial Fulfillment
of the Requirements for the Degree
Master of Science in the
George W. Woodruff School of Mechanical Engineering

Georgia Institute of Technology
May 2020

EFFECT OF BUILD ORIENTATION OF ANISOTROPIC BEHAVIOR IN DIRECT ENERGY DEPOSITION BUILT COMPONENTS

Approved by:

Dr. Tomas Kurfess, Advisor
School of Mechanical Engineering
Georgia Institute of Technology

Dr. Tommy Tucker
Chief Executive Officer
Tucker Innovations Incorporated

Dr. Christopher Saldana
School of Mechanical Engineering
Georgia Institute of Technology

Dr. Katherine Fu
School of Mechanical Engineering
Georgia Institute of Technology

Date Approved: April 24, 2020

ACKNOWLEDGEMENTS

I would like to sincerely thank my advisor, Dr. Thomas Kurfess, for helping and guiding me through each stage of this process. I truly could not have done this without his continuous support.

I would also like thank the other members of my thesis committee, as well my lab mates. What we do truly takes a team effort and I have learned so much working with everyone and am eternally grateful.

Lastly, to my friends, family, and partner, Emily, you have done nothing but encourage and empower me to continue in my work, and this project would not have been possible without you all.

Table of Contents

LIST OF TABLES

LIST OF FIGURES

LIST OF COMMONLY USED TERMS AND SYMBOLS

AM	Additive manufacturing
ANOVA	Analysis of variance
CAD	Computer-aided design
CNC	Computer numeric control
CT	Computed tomography
FDM	Fused deposition modeling
DED	Directed energy deposition
DMD	Direct metal deposition
DMLS	Direct metal laser sintering
DOF	Degree-of-freedom / Degrees-of-freedom
E	Young's modulus
EDM	Electron discharge machining
FCC	Face-centered cubic
G	Temperature gradient
HAZ	Heat affected zone
HWD	Hot-wire deposition
LENS	Laser engineered net-shaping
LM	Layered manufacturing
LOF	Lack of fusion
L-PBF	Laser powder bed fusion
NC	Numerical control
R	Growth rate
RSM	Response surface methodology
S	Solidification rate
SEM	Scanning electron microscopy
SS	Stainless steel
SLM	Selective laser melting
SLS	Selective laser sintering
SM	Subtractive manufacturing
σ_{YS}	Yield stress
σ_{UTS}	Ultimate tensile strength

SUMMARY

Hybrid manufacturing integrates complementary subtractive and additive manufacturing processes into a single machine tool. Seamless integration of conventional subtractive machining and direct energy deposition (DED) allows for the production of complex, net-shape metallic components in a single manufacturing system. Hybrid manufacturing has the potential to improve repair processes and reimagine the production of new components by minimizing material waste, reducing cycle times, and expanding design flexibility. However, a major obstacle to the wide-scale acceptance of DED technology is a limited understanding of defect formation within the novel microstructures produced in DED, their relation to process parameters, and effect on resultant mechanical properties. For example, it has been shown in the literature that simple process decisions, such as changing the build orientation, can result in a 25% variation in yield strength between the vertical and horizontal orientations.

In this study, the effects of layer orientation on the mechanical properties of hybrid 316L stainless steel (SS) components fabricated via a DED additive manufacturing process are investigated. Quasi-static tensile tests are conducted on "bi-metallic" wrought and DED 316L SS specimens fabricated in orientation increments of 15° with respect to the loading direction. Specimens are tested in their as-built condition without any post-process heat treatment. Young's Modulus (E), yield strength (σ_{YS}), ultimate tensile strength (σ_{UTS}), and maximum elongation are measured, and it is found that the presence of internal defects, particularly interlayer porosity, plays a dominating role in governing many of the mechanical properties measured. In extremely low porosity components, microstructure may dominate anisotropic performance. In the presence of interlayer porosity, however, the 0° orientation is subject to lower stiffness and elongation, whereas higher angle orientations experience higher yield strength and greater ductility.

CHAPTER 1: INTRODUCTION

Dubbed “Hybrid Manufacturing”, the integration of additive manufacturing (AM) and subtractive manufacturing (SM) into a single machine platform has the potential to revolutionize the way in which engineers design and manufacture products. By combining the two technologies into one machine tool, it becomes possible to seamlessly alternate between material removal and material deposition throughout the build process. The effects of various material removal processes on the final mechanical properties of the produced parts has been studied for centuries. However, by comparison, layer-based additive manufacturing processes such as Directed Energy Deposition (DED) still have significant work that needs to be done to understand the impact of how the different methods and techniques used to deposit and fuse material change the mechanical, thermal, electrical, properties of the final part. AM refers to processes where parts and features are constructed by adding material incrementally to the substrate or parent material. In DED, as in other AM processes, one layer is fused to the material below, thus, in the as-built state, it is likely that the mechanical properties of the part are anisotropic in nature. Of interest is how the orientation of the layers in relation to the axes of applied stresses alter the mechanical performance of the part in the direction of interest.

Many different types of additive processes exist that utilize a huge range of materials including polymers, metals, and biomaterials – fused-deposition modeling (FDM), selective laser sintering (SLS), stereolithography, laser powder bed fusion (L-PBF), DED, etc. Most of these processes are layer-based, in that one discrete layer is bonded to the layers below and, in that manner, features are constructed step-by-step. AM provides engineers with increased geometric flexibility to design and manufacture part geometries that are either not possible or cost prohibitive utilizing traditional manufacturing methods. Common examples include components with internal conformal cooling channels, topology-optimized designs, and lattice structures. AM has been extremely successful in the

area of rapid prototyping. It reduces the need to use costly and long lead time molds and other work holding fixtures traditionally required to create near-net shape and complete parts, allowing engineers to rapidly iterate their designs, thereby reducing the time to market.

Compared to other additive manufacturing processes, such as L-PBF or SLS, DED material can be deposited with greater degrees-of-freedom using multi-axis coordinated motion; DED is not limited to depositing on planar surfaces. While in the coaxial cladding configuration, the nozzle should remain normal or nearly normal to the substrate surface; the substrate itself can be positioned in many different alignments and the surface geometry can not only be non-planar but can also be extremely complex.

DED is a popular AM process used for producing complex geometric features and generating surface coatings on components. It has been selected as the AM process of choice for many applications due to the ease with which the process can be retrofit onto various motion platforms, such as Computer Numeric Control (CNC) equipment and high degree-of-freedom robotic manipulators. DED is used heavily in the manufacturing of large components such as tooling for forging dies [1], repair of high-value components [2], and hardfacing – a metalworking technique whereby a harder, more wear-resistant material is applied to the surface of a part to extend its lifecycle [3]. Generally, in all of the aforementioned applications, the goal is to produce fully dense components that are sufficiently bonded to the substrate and meet the geometric and functional performance requirements of the components' intended end-use.

For most applications, however, AM parts often require a certain amount of post-processing in the form of machining, grinding, polishing, and etching, among others. Currently, AM process have been shown to be limited in their ability to achieve the geometric accuracy, tolerances, and surface finish of other processes. When coupled with conventional CNC machining operations, there is increased flexibility for the engineer to design the manufacturing process, with the goal of reducing

production time and material costs, while achieving a high-quality, repeatable process. A major challenge for many companies utilizing additive manufacturing is how to fixture the part for additional material removal operations, like when working with castings. Hybrid machines provide the opportunity to reduce set up time between operations, reduce occupation of valuable floor space needed for multiple pieces of capital equipment, and allow for parts to be produced with internally-machined features that would otherwise be inaccessible [4]. The concept of developing a seamless, automated process from loading raw materials into a workstation to unloading a finished part has often been referred to as "done-in-one" manufacturing. Hybrid manufacturing systems have been implemented successfully in a variety of industries, including but not limited to automotive, aerospace, and mining, to build parts, tooling, and perform repair processes [5].

Rapid prototyping is a family of manufacturing processes that allow products to be produced fast and relatively inexpensively. The advantage of rapid prototyping is that it allows for quick iteration during the early stages of a product's development. DED and hybrid manufacturing are tools that, along with other layer-based AM processes, aid engineers in producing complex net-shape parts without the costly tooling and fixturing that is usually required during full-scale production. While most AM processes are near net-shape, combining DED with CNC machining provides the additional benefit of making parts with production-level surfaces finishes and tolerances.

In hardfacing applications, the added material is usually selected based on improved mechanical and thermal properties such as high hardness or enhanced wear performance over the base metal – especially at elevated temperatures. Hardfacing lowers component costs because cheaper materials can be used to make up the bulk volume of the part, while the critical surfaces are coated with more expensive materials in order to achieve the necessary surface properties. Often the coating material is much more expensive or difficult to process. Popular surface coatings, such as Stellite-6 and other cobalt-alloys often used as a material in cutting tools, are challenging and slow to

machine, making them less ideal for working with in large volumes. Hardfacing can be performed to refurbish part faces as they wear from normal use or as a value-added operation conducted in order to extend the lifecycle of a given component. The surfaces are then finish-machined to realize the necessary geometric and surface finish requirements.

Another application for DED and hybrid manufacturing is in the area of component repair. Many high-value components, such as tooling or turbine blades, are extremely expensive to produce, as well as suffering from long lead times [6]. Significant cost and time savings can be realized if, instead of procuring new, replacement parts from a supplier, components can be repaired and returned to service. Hybrid manufacturing also unlocks the option of fixing errors that occur during subtractive and additive manufacturing by cutback machining or filling voids and gouges that may occur during either process.

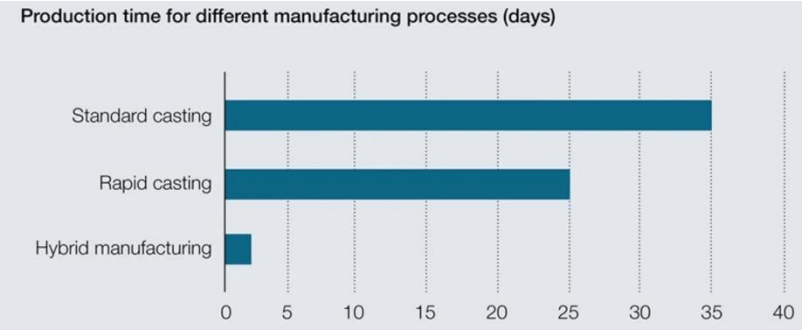

Figure 1: *Production time for different manufacturing processes (days) [6]*

In addition to the aforementioned use cases, hybrid manufacturing enhances traditional methods of production. Features can be added on, protruding from the exterior surface from a part, that, if machined from billet, would be costly, as most of the material would be scrapped in the form of chips. In some high buy-to-fly ratio aerospace components, 90% of the material is scrapped in this manner [7]. There is also the advantage of being able to initially machine features that may later become inaccessible to a cutting tool as additional material is built up; this process avoids the

potential issue associated with traditional methods of needing to produce multiple sub-components that are then affixed to each other through mechanical fasters or another joining process.

In all of the applications, whether it be repair, hardfacing, or producing a wrought-DED multi-material component, the part should generally perform equally or better than the traditionally manufactured part by meeting all of the required mechanical, thermal, and/or electrical requirements. A part subject to DED processing can be broken down into three main regions: substrate, interface, and deposit region. DED parts are subjected to high temperatures and thermal gradients; it is important to consider how the base material responds to the intense localized heat that results from the additive process. Just outside the deposition track there exists a region of the substrate that is subject to high heat—the heat affected zone (HAZ). Many process parameters influence the outcome of the additive process. If two dissimilar metals are being fused together, the bonding strength of the substrate and deposited material is largely determined by the material compatibility [8]. In addition to the localized mixing of two similar or dissimilar metals, the geometry of the interface should be designed to enhance performance by taking into consideration the component loading conditions. Material and process parameter selection should consider the compatibility of the AM and parent material, and, in some cases, a buffer material might be necessary [9].

Aside from material selection – including the size and form of the feedstock – most process variables influence the complex thermal history of the part, including tool path planning, laser power, and scanning speed. Some of the many decisions that go into building a successful part include:

- Material selection (compatibility, powder size, response to heat, etc.)
- Toolpath design (spiral, zig zag, overlap, dwelling, etc.)
- Interface preparation and geometry (surface condition, geometry, etc.)
- Tunable build parameters (laser power density, traverse rate, material delivery, spot size)

- Substrate pre-heating, interpass, and post-process temperatures

Significant research has already been pursued in this area with regards to build parameter selection, effect of powder geometry, toolpath design, build direction, and their effects on mechanical and wear properties. It has been shown in the literature that, due to the unique rapid heating and cooling cycles present in most AM processes and its layer-based manufacturing method, that anisotropic material properties often exist in components produced using these technologies. However, most previous work is concerned with fully wrought material, fully AM material, or the wear characteristics of a surface coating. While some studies have investigated the effects of build orientation in DED steel specimens, they tend to be restricted to 0°, 45°, and 90° orientations. There has been little investigation as to how build orientation affects mechanical properties of hybrid wrought-AM components including the interfacial bonding strength. A major obstacle to the wide-scale acceptance of DED technology is a limited understanding of defect formation within the novel microstructures produced, their relation to process parameters, and effect on resultant mechanical properties. It has been shown that a simple process decision, such as changing the build orientation, produces up to a 25% variation in yield strength between the vertical and horizontal orientations in as-built components.

This study investigates the effects of layer orientation on the mechanical properties of 316L stainless steel (SS) fabricated via a DED additive manufacturing process. Quasi-static tensile tests are conducted on DED 316L SS specimens fabricated in orientation increments of 0°, 15°, and 30° with respect to the uniaxial loading direction. Specimens are tested in their as-built condition, without any post-process heat treatments. Young's Modulus (E), yield strength (σ_{YS}), ultimate tensile strength (σ_{UTS}), and maximum elongation are measured, and it is found that the presence of internal defects, particularly interlayer porosity, play a dominating role in governing many of the mechanical properties measured. In extremely dense, low porosity components, microstructure may dominate

anisotropic performance. In the presence of interlayer porosity, however, the 0° orientation is subject to lower stiffness and elongation, whereas higher angle orientations experience higher yield strength and greater ductility.

CHAPTER 2: BACKGROUND

2.1 Brief History of Directed Energy Deposition and Hybrid Manufacturing

2.1.1 Development of Laser Cladding and DED

The development of the high-power gas laser in 1975 made industrial processes with lasers, such as cutting, welding, and metal hardening, possible in the latter part of that decade. The first known use of a laser cladding process was conducted by Gnanamuthu at Rockwell International Corporation in the late 1970s, using a preplaced powder [10]. Shortly after, different researchers sought to develop and improve upon the process. In the 1980s, Steen and Weerasinghe introduced laser cladding by powder injection [11]. Mazumder's research team at University of Illinois Urbana-Champaign contributed significantly to the field by developing the initial models and studying the mechanisms of the process [12]. They tested the potential cladibility, as well as wear and corrosion resistance, of many metals and ceramics. Even ahead of academic projects, Rolls-Royce was reportedly using laser cladding in 1981, hardfacing Nimonic turbine blade interlock shrouds for the RB-211 jet engine [13]. In 1983, Pratt and Whitney followed suit with another hard-facing application, coating the nickel-based alloy turbines of JT8 and JT9 engines [14]. Automotive companies, such as Fiat, Toyota, and Mercedes Benz began using laser cladding in the 1980s, as well, to coat engine valve seats [13] [15]. In this decade, laser cladding also showed much promise for the component repair industry – it had already been proven to be successful in the repair of the H-dimension of worn turbine vanes, the tip of the turbine blade, and turbine bolts [16]. To support the increasing demand and accepted use in industry, companies such as Avco Everett Metalworking Lasers Inc. and United Technologies Industrial Laser Inc. were established.

In the 1990s, laser cladding received a great deal of attention with the development and growth of rapid prototyping and other layer-based manufacturing processes. "Stereolithography", a method using photopolymerization to accurately fabricate, visualize, and iterate new designs directly from 3D Computer-Aided Design (CAD) models, was patented in 1986. While most rapid prototyping

systems used polymers and photopolymers, commercial companies needed a way to rapidly fabric features in metal. Mazumder's group expanded on their cladding research and introduced what is now called DMD or "direct metal deposition" [17]. They licensed the technology to Precision Optical Manufacturing Inc. for automotive mold and die fabrication. Sandia National Laboratories began conducting research in laser near-net shaping and eventually patented the technology under the name "Laser Engineered Net-Shaping"", or LENS for short [18]. Under Steen, The University of Liverpool contributed significantly to the field of direct laser manufacturing [19]. A research group at the University of Waterloo also researched the development of intelligent laser cladding systems, using sophisticated modeling techniques and knowledge-based controllers to process feedback control [20].

2.1.2 Development of Hybrid Manufacturing

While AM offers enhanced geometric flexibility and possibilities of high material utilization – up to 100% with HWD [21] – it still suffers from relatively long cycles times, poor surface finish, and limited accuracy. Conventional material removal processes, such as CNC machining, are able to achieve low cycle times (through high material removal rates), surface roughness of R_a 0.4-6.3 μm in average applications, and average tolerances of 50-12.5 ± mm x 10^{-3} and less than 5 ± mm x 10^{-3} under special operating conditions [22]. Surface finishes for AM processes are characteristically grainy, with measured roughness on the order of a few tens to a few hundred microns, depending on the process; it is often likened in general appearance to precision casting technology results [23].

Parts produced by AM often require post-processing operations such as machining, grinding, polishing, electro-chemical etching, and others in order to be integrated into an assembly [24]. By combining AM and CNC machining, engineers can leverage the advantages of each manufacturing process. Multi-tasking machine tools are being further-enhanced to offer multiple manufacturing processes, improving production capabilities and moving towards the "done-in-one" model of

manufacturing [25]. The first research in integrating blown powder laser DED into a CNC machining system took place in the mid-to-late 1990s by Klocke and Wirtz [26]. Also, in the 1990s ,the Laser Aided Manufacturing Processes Laboratory housed within the University of Missouri at Rolla, developed a hybrid 5-axis laser deposition/CNC machining process where they outfitted a Rofin-Sanar 025 laser deposition system, consisting of a laser and a powder feeder, onto a Fadal VMC3016L CNC machining center [27].

At the International Manufacturing Technology Show in 2016, Mazak Corporation unveiled its own "hybrid multi-tasking" machine tool, a VC-500AM [28]. Based on the VCU 5-axis series, Mazak outfitted a VCU-500 5-axis milling machine with an Oerlikon powder feed system, IPG Photonics laser unit, and Hybrid Manufacturing Technologies deposition head. The 2018 show featured the next iteration of Mazak's hybrid milling machines, demonstrating the capabilities of its VC-500A/5X AM HWD [29]. Instead of using powder feedstock, the VC-500A/5X AM HWD was developed as a "hot-wire" machine based on technology developed in conjunction with Lincoln Electric Corporation. Currently, a VC-500A/5X AM HWD is stationed at Oak Ridge National Laboratory, Knoxville, Tennessee, where continued research in laser hot-wire deposition is taking place. A comprehensive list of hybrid manufacturing systems is outline in ***Table 1***. The list is sourced from a survey paper of hybrid manufacturing technologies by Lorenz et. al. presented at the 2015 Solid Freeform Fabrication Symposium [21].

Table 1: *Survey of Hybrid Manufacturing Systems*

Date	Process name	Institute/Company	Machine tool type	Process head mounting position
1996	Combined Metal Build Up (CMB)	Fraunhofer Institute of Production Technology & Fraunhofer Institute of Laser Technology	3-axis vertical	Fixed to side of spindle
1990's	Laser Aided Manufacturing Process (LAMP)	University of Missouri	5-axis vertical	Fixed to side of spindle
2000	Selective Laser Cladding (SLC) and milling	National Taiwan University of Science and Technology	3-axis vertical	Fixed optics (separate station)
2004	Hybrid Manufacturing	Joanneum Research Forschungsgesellsc haft mbH, Austria	5-axis vertical	Fixed to side of spindle
2006	System and method for fabricating and repairing part	Southern Methodist University	Multi-axis	Attached to a robot
2008	Hybrid Manufacturing	De Montfort University & The Manufacturing Technology Centre	3-axis vertical	In spindle stored in tool magazine
September 2013	Hybrid Manufacturing	Hamuel & Hybrid Manufacturing Technologies	Retrofit to any machining platform	In spindle stored in tool magazine
December 2013	Hybrid Manufacturing	DMG Mori	5-axis vertical	In spindle stored in own compartment
November 2014	Hybrid Multitasking	Mazak & Hybrid Manufacturing Technology	5-axis horizontal	In spindle stored in tool magazine
April 2015	Additive Manufacturing	WFL Millturn Technologies	5-axis slantbed lathe	Unknown
May 2015	LENS®	Optomec	Retrofit to any machine platform	Fixed to side of spindle
June 2015	Hybrid Manufacturing	ELB & Hybrid Manufacturing Technologies	millGrind Creep Feed 5 axis	Fixed to side of spindle

2.2 Directed Energy Deposition and Hybrid Manufacturing

2.2.1 Equipment

A DED system is composed of four main subsystems: heat source, material delivery mechanism, motion/position control, and a computer control system. There are many different configurations of DED systems. The chosen configuration depends on the desired application: generating surface coatings versus complete parts, precise features versus high deposition rates, material selection, etc. These decisions influence considerations such as motion platform, machine volume, deposition nozzle, laser type, and feedstock delivery method.

Laser DED systems utilize laser beams, with beam and/or fiber delivery, along with focusing optics, providing highly controllable energy to localized areas of the substrate. Lasers have become popular for hybrid systems for their flexibility and robustness. Depending on the laser source of choice, it can achieve wall-plug efficiencies as high as 40%, coupling efficiency – defined as energy absorption by the substrate – from 5% to over 40% depending on wavelength and substrate material, and powers easily ranging from 100 to 4000W. Lasers are available with various spot sizes ranging from 50 microns to 25mm. They can be operated in non-vacuum environments – as opposed to electron beam heat sources – thus making large volume builds possible or be used in portable systems. An additional advantage is the high energy density, so the HAZ and workpiece distortion is limited as compared to other thermal processes, such as plasma-arc DED. Lasers also have the benefit that their motion can be precisely controlled using CNC technology and robotics for use in harsh environments and for high-accuracy work.

The laser utilized in this study is a YLS-CUT-1000 produced by IPG Photonics. It is an ytterbium fiber laser capable of continuous-wave output power ranging from 100 to 1000W; the output wavelength is 1070 ± 10 nm. The unit is capable of at least 40% wall-plug efficiency depending on the mode of operation. The YLS system is a single TEM_{00} mode system; TEM_{00} is the lowest-order, fundamental transverse gaussian mode. Thus, no nodes are present in the output beam's transverse intensity distribution.

As mentioned, the feedstock for metal DED can take the form of either wire or powder. Small features requiring little to no post-processing may benefit from using small diameter powder feedstock, as powder diameters tend to be much smaller than standard gage welding wire. While wire feedstock has the advantages of being significantly safer to handle than powder, the potential to utilize 100% of the material, and fewer challenges associated with processing and feeding the material, it is only available in limited sizing and not all metals can be fed into the melt pool using a

wire configuration. Additionally, by using multiple hoppers, the powder can be blended in-situ to create new alloys and functionally graded components.

DED by powder suffers from poor material utilization and over-spray. The powder catchment efficiency – the ratio of powder supplied to fused powder – can never reach 100% and may be less than 50% in certain configurations [21]. The unused powder not only poses an economic problem as the wasted powder most likely cannot be recycled and drives up the cost of the process, but the powder also contaminates the machine. Using powdered metal carries significant environmental health and safety concerns necessitating the use of proper personal protective equipment and necessary precautions to prevent uncontrolled thermal events. Understanding the hazards involved and how to mitigate them is especially true when working with high explosion index metals such as titanium and aluminum [30].

In a gravity-based powder feeder system, the powder is gravity-fed through a reduced orifice, similar to sand in an hourglass, into a rotating metering disk. The disk contains a small channel that fills with powder and carries the powder from the spreader bar to the suction bar. Back pressure is used to force the powder through the suction bar, and the fluidized powder is transported via carrier gas through the plumbing to the deposition nozzle exit. The size of the powder feeder mechanical components, amount of back pressure, and rotational speed of the disk can be finely tuned to control the mass flow rate and velocity of the powder particles. A schematic of the Twin-150 Multipurpose powder feeder used in this study is shown in **Figure 2**.

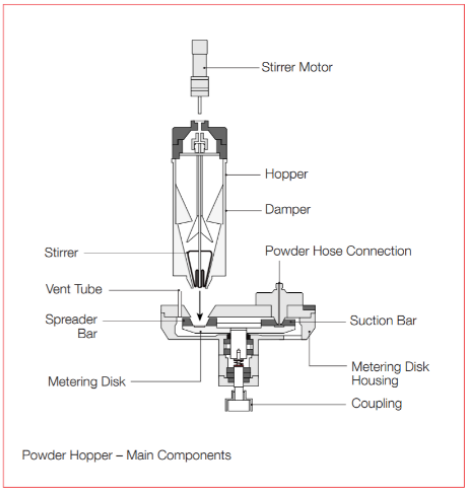

Figure 2: *Schematic of Oerlikon Twin-150 Powder Feeder*

The Mazak VC-500 AM machine is equipped with an Oerlikon Twin-150 multipurpose powder feeder. The Twin-150 is designed to operate as a multipurpose standalone unit for processes such as plasma, High Velocity Oxygen Fuel coating, laser cladding, and powder-fed additive manufacturing. The controller is also capable of integration into an existing machine through profibus communication protocol. The unit is designed to operate with Argon or Nitrogen carrier gas and can utilize powder hopper capacities of 1.1L, 1.5L and 5.0L. For the builds conducted in this research, the 5.0L hopper is used.

The deposition head is responsible for shaping and directing the powder flow to the process region, as well as shrouding the process zone in shielding gas to maintain an inert environment until the metal sufficiently cools. As gravity effects powder delivery, delivery to the melt pool generally works best when the deposition head is located above the melt pool so that gravity acts parallel to the powder stream. Powders can be fed from the side (in side-cladding) or in line with the laser (co-axial configuration). The injection ports may be oriented in 90° and 120° increments, or in an annular configuration around the inner laser nozzle. The Hybrid Manufacturing Technologies nozzle configuration in use is the S3 Sidemount System-Model 3935.

To enable the realization of a 3D structure built with DED, the nozzle and workpiece must be able to move in relation to one another. The motion platform may take the form of a machine tool or a higher degree-of-freedom system such as a robotic arm. The positional control of the laser and powder delivery nozzle is realized through the operation of the Mazak VC-500 5-axis hybrid machine tool and its Mazatrol SmoothX controller. The machine tool used for this work, designed by Mazak Corporation, is one of the first of its kind. The machine is adapted from the VCU-500 A/5x vertical machining center. The machine is equipped with a trunnion-style BC-style rotary axes and has a working volume of 505 x 505 x 510 mm^3. The maximum workpiece diameter that can be accommodated is 500 mm and the maximum workpiece height is 305 mm.

The DED system is retrofit onto the VCU frame, so that the powder feeding and laser units are located next to and behind the machine, respectively. The DED nozzle and column containing the optics, powder, and gas delivery, are coupled to the milling spindle for its XYZ motion. However, the deposition head is also capable of independent motion in the +Z or -Z direction on its own W-axis. The table's BC rotary axes manipulate the rotary orientations of the component.

The inputs to the motion control system are paths that the motion platform follows. The motion of the axes are controlled using G-code that is downloaded to and interpreted by the controller of the machine. G-code is a numerical control (NC) programming language, which contains commands that tell the machine tool how to make a part. The commands are contained in blocks executed in sequential order; each block contains an alpha-numeric code that tells the machine how to move or to execute any number of other necessary auxiliary functions. The internal trajectory planner of the machine determines the exact manner in which blocks of G-Code are executed. The laser deposition mode is activated through a macro program, which shifts the drive point of the machine from the spindle face to the nozzle tip plus the desired standoff distance. This action is accomplished through a series of offsets that shift the workpiece coordinate system, the table center of rotation, and the tool

offset. The distance between the spindle face and deposition head are stored in a series of PLC parameters on the controller.

The deposition parameters are set using a macro subprogram executed within the main NC program. The macro sets the laser power, nozzle gas flow rate, shielding gas flow rate, duty cycle of the powder feeder metering disk, and the carrier gas flow rate. Once the nominal settings have been set, the gas flow and hoppers can be toggled on and off as single blocks of G-code. The hoppers may be turned on individually or they can be operated simultaneously to achieve various mixtures of different feedstock. The other DED process parameter of primary importance – traverse speed – may be set once, modally, at the beginning of the program, or may be regulated per block.

The current VC-500 hybrid DED system is controlled in a time-invariant, open-loop manner. The process control that takes place is not based on feedback from the process itself. Ongoing work is being done to incorporate more process feedback into the control of the machine including melt pool size monitoring, process zone temperature monitoring, and layer height monitoring. Information from the process monitoring instrumentation will then direct minor deviations from the nominal settings to yield the desirable control outputs.

Generating the toolpath for the machine to follow is often carried out in a path planning software. While simple toolpaths may be written by hand, in order to generate a component of any appreciable complexity – especially when coordinated multi-axis motion is required – a path planning software is necessary. One of the major benefits of additive manufacturing and DED is that complex geometries with limited geometric constraints may be produced that cannot be manufactured using a conventional method such as machining. This process requires that engineers employee CAD software tools to accurately model complex features and surfaces using geometric modeling tools. The CAD models may be modelled discretely in mesh or voxel forms, which are used extensively for rapid prototyping and stereolithography. Other modeling paradigms include boundary

representation (BReps), which describe the topological and geometric relationship between components (point, curve, surface and vertices, edges, faces), and Constructive Solid Geometry (CSG), which consists of solid geometric primitives that are combined using various Boolean operations to create a final shape.

The different modeling methods have various benefits and limitations, but regardless of the method, the geometry is then used to generate the desired toolpaths in order to realize the final geometry of the component. In most AM and layer-based manufacturing scenarios, the path planning is performed in a Slicer, which dissects the part into 2D cross-sections based on desired layer thickness, and then a tool-path strategy is chosen to deposit or fuse material throughout the slice. The machine is then incremented in the z-axis and the process is repeated.

2.2.2 Process

An understanding of the underlying physics of the complete DED process is critical to reducing process development timeline, moving towards a closed-loop automated system, and successfully implementing DED and the use of hybrid machine tools in industry. In DED, it is possible to produce parts of the same net shape but with different properties. For example, two parts could be produced that are geometrically alike, but one part is manufactured with different spacing between adjacent tracks. This difference might cause some internal porosity to exist, unbeknownst to the manufacturer, making the part not fulfill its designed lifecycle. Another example is with melt pool solidification rates, which largely depend on the laser power and scanning velocity used. Again, while two parts may look identical, two different solidification rates will result in two different microstructures.

The coaxial blown powder DED process consists of several different complex steps. One complicating factor is that the process consists of numerous different interactions that take place

between the laser, powder stream, substrate, nozzle, carrier, and shielding gases. First, the powder is ejected from the nozzle. A large portion of the powder travels through the laser beam over some distance and absorbs a fraction of the beam's energy. The remaining laser energy strikes the surface of the substrate and generates a thin layer of molten metal. The powder particles, melted and solid, impact the surface of the part. Some particles ricochet off the surface. However, the remaining particles are added to the melt pool. Gradients in surface tension drive melt pool flow through Marangoni convective forces and cause the metal particles to mix with the melted parent material, resulting in good metallurgical bonding. Depending on the thermal input into the process, and the geometry of the substrate and already deposited material, large thermal gradients can occur where the temperature can vary between 40° C and 1000° C within a short distance (millimeters) in the build [31][31]. The molten metal is also known to experience rapid solidification (~103–108 K/s) [32]. The magnitude and direction of the thermal gradients, solidification rates, and degree of similarity between the added and base materials determines the mode of solidification and resulting microstructure.

The purpose of this paper is not to present a fully developed thermo-mechanical model of the DED process and all of its interactions, but a brief discussion has been in included in the following section to provide the reader with the necessary background information about the process. The process of DED can be dissected into several sequential steps. Most researchers interested in modeling the process have focused their efforts on modeling each process individually, while a few have attempted to create more integrated models. Several steady-state, time-independent models have been proposed, and a few researchers have worked to incorporate the transient nature of the process. In order to comprehensively model the entire process, it is essential to address several key physical phenomena of the process including thermal conduction, Marangoni flow, powder and shield gas effects on the melt pool, mass transport, and diffusion. Multiple interactions must also be considered: laser-powder, melt pool-powder, and laser-substrate.

The process has traditionally been broken down to the following steps for ease of modeling. The process begins with powder and shielding gas flowing out of the deposition head, the dynamics of which are governed by the geometry of the deposition head, the flowability characteristics of the powder, and the interaction between the powder stream and shielding gas [33] [34]. The powder particles arrive at the substrate surface at a different range of temperatures depending on their path through the Gaussian-distributed laser beam, their velocity, and how much shielding occurs from other powder particles [35][36]. Powder is then either captured and sticks to the surface through surface tension or rebounds off of the solid substrate and is lost. The catchment and resulting solidification are closely related. As the powder particles pierce the melt pool they change the thermal distribution, causing changes in the convective flows within the molten material, and governing resulting heat transfer dynamics [37] [38].

2.2.2.1 Energy balance above the melt pool

Using a simplified lumped model, where the behavior of the process is simplified into time-dependent ODEs with a finite number of parameters, the amount of laser energy that is absorbed by the substrate can be estimated by the energy balance equation (Eq. 1):

$$Q_c = Q_l - Q_{rs} - Q_L + (\eta - 1)Q_p - Q_{rp} - Q_{radiation} - Q_{convection} \quad (1)$$

where Q_c is the total energy absorbed by substrate (J), Q_l represents the energy output of the laser (J), Q_{rs} is the energy reflected by substrate, Q_L is the latent energy of fusion (J), the η term is a constant representing the powder catchment efficiency, Q_p is the energy absorbed by the powder particles (J), Q_{rp} is the energy reflected from the powder particles (J), $Q_{radiation}$ is the energy loss due to radiation, and $Q_{convection}$ represents the energy loss due to convection (J).

The energy delivered by the laser beam can be represented by the following relation (Eq. 2):

$$Q_l = A_l P_l t_l = \pi r_l^2 P_l t_i \quad (2)$$

where A_l is the laser beam area on substrate (m^2), r_l is the beam spot radius on the substrate (m), P_l is the average laser power (W), and t_i is the interaction time between laser and material (s). The interaction time is dependent on the process speed or traverse speed of the laser, as well as the size of the laser beam on the surface (Eq. 3).

$$t_i = \frac{2r_l}{U} \quad (3)$$

U is the process speed (m/s). The energy reflected by the substrate is the total amount of energy that reaches the surface minus the fraction that is absorbed (Eq. 4):

$$Q_{rs} = (1 - \beta_w)(Q_l - Q_p) \quad (4)$$

β_w is the workpiece absorption coefficient. β_w *most likely* needs to be experimentally determined, as it is dependent on the wavelength of the incident energy, the surface finish of the substrate (may vary by a factor of two just from changing from a polished surface to a milled surface where Ra = 2.95μm), the temperature of the materials, and the cleanliness of the surface [39]. As this process takes place in a machine tool, there might be coolant or oil that could have contaminated the surface. The energy required to melt the metal is (Eq. 5):

$$Q_L = L_f \rho V \quad (5)$$

L_f is the latent heat of fusion (J/kg), ρ is the average density in the clad area (kg/m^3), and V is the volume of the melt pool including the clad region (m^3). In the lumped model, V can be assumed to be a cylinder lying along the cladded track with a length equal to the diameter of the beam and the width of the clad is equal to the diameter of the beam. The cross section is A_c (Eq. 6):

$$A_c = \frac{\dot{m}}{\rho_p U}\eta \quad (6)$$

ρ_p is the particle density (kg/m^3). If dilution is ignored, which is acceptable for many laser cladding operations, the volume of the clad track is approximated as (Eq. 7):

$$V = 2r_l A_c \quad (7)$$

In a lumped model, the power catchment efficiency can be simplified to only consider the ratio of the laser beam area to the powder stream area on the substrate:

$$\eta = \frac{r_l^2}{r_s^2} \quad (8)$$

r_s is the powder stream radius on the substrate (m). The ratio (Eq. 8) can be determined by factoring in the initial powder and laser diameters, their respective divergence angles, and the standoff distance between the deposition head and the melt pool surface:

$$\frac{d}{D} = \frac{2r_l}{2r_s} = \frac{r_l}{r_s} = \frac{(d' + Stan\delta)}{(D' + Stan\theta)} \quad (9)$$

d/D is the ratio of the melt pool diameter to the powder stream, d' is the initial diameter of the laser beam exiting the nozzle, D' is the initial powder stream diameter exiting the nozzle, S is the standoff distance, δ is the divergent angle of the melt pool variation in the beam axis, and θ is the spraying angle of the powder stream.

However, as the powder is not uniformly distributed, but follows more of a Gaussian distribution, the catchment efficiency calculation can be further refined by integrating the volumetric powder concentration on the melt pool to the entire spray area [37]. The Gaussian function and powder catchment efficiency can be expressed by the equations (Eq. 10, Eq. 11):

$$G(\zeta) = exp\left(\frac{-\zeta^2}{2}\right) \quad (10)$$

$$\eta\left(\frac{d}{D}\right) = \frac{\int_{\zeta_d} G(\zeta)\zeta d\zeta}{\int_{\zeta_D} G(\zeta)\zeta d\zeta} \quad (11)$$

G(ζ) is the Gaussian function, $\zeta_d = d/\sigma$ and $\zeta_D = D/\sigma$, where σ is the stream diameter corresponding to 60% coverage of the concentration in the section plane. Selecting $D = 3.5\sigma$, for example, so that $\zeta_D = 3.5$, Eq. 11 can be re-arranged to yield the following relation (Eq. 12), where this selection of the powder stream diameter covers 99.8% of the concentration in the plane of the substrate surface.

$$\eta \cong 1 = exp\left[\frac{-\left(\frac{3.5d}{D}\right)^2}{2}\right] \quad (12)$$

It can be seen from this equation that powder catchment efficiency increases with a higher d/D ratio and approaches 80% as d/D=0.5.

To simply approximate the energy absorbed by particles in the particle stream, consider a homogeneous distribution of powder over the laser cross-section (Eq. 13):

$$n = \frac{3\dot{m}t_i}{4\rho_p r_p} \quad (13)$$

r_p is the particle radius, ṁ is the power feed rate (kg/s), ρ_p equals the powder density (kg/m^3), and n represents the number of the particles in the beam area per time t_i. The area of powder particles in laser beam indicates the attenuated area A_{at} by the powder particles (Eq. 14):

$$A_{at} = n\pi r_p^2 = \frac{3\dot{m}t_i}{4\rho_p r_p} \quad (14)$$

It follows that the energy absorbed by powder particles can be estimated by Eq. 15:

$$Q_p = Q_l \frac{A_{at}}{A_l} = \frac{3Q_l\dot{m}t_i}{4\pi\rho_p r_p r_l^2} \quad (15)$$

This model makes many simplifying assumptions, such as considering the powder stream and laser energy as uniformly-distributed columns, not considering the irradiation time of the powder particle based on its velocity and nozzle stand-off distance, shielding of downstream particles by upstream powder particles, and changes in particle absorptivity due to temperature and oxidation layers.

Fu et al. has a more complex model that takes into consideration the laser beam intensity distribution. It also is able to handle the side cladding configuration [40]. They argue that in early theoretical modeling, all particles are assumed to have the same temperature when they reach the surface of the part, and that this simple treatment conceals the changes in flow motion within the melt pool due to the temperature variation among the particles. As it is known that surface tensions are sensitive to thermal gradients, which prove to be the main force in pool flow motion,

understanding the temperature distribution of the powder particles incident to the melt pool is critical to determining the properties of the clad. Additionally, as the powder particles absorb the laser beam energy, the beam is not only attenuated, but its distribution changes as well. A thorough investigation of the more comprehensive and complex model presented by Fu et al. is outside the scope of this paper. A simplification is presented here, where the power distribution of a TEM_{00} mode laser, such as the optics used throughout the duration of this study, can be described by the Gaussian distribution function (Eq. 16):

$$P(x,y) = \frac{P_o}{\pi r_l^2} exp\ (-\frac{x^2+y^2}{r_l^2}) \quad (16)$$

where P_o is the total laser power and r_l is its radius. Beam divergence is considered in the above equation through the selection of the beam diameter.

The total reflected energy by the powder particles is equal to (Eq. 17):

$$Q_{rp} = (1-\beta_p)Q_p \quad (17)$$

β_p is the powder particles' absorbed coefficient. The laser energy loss to radiation is (Eq. 18):

$$Q_{radiation} = A_l \epsilon_t \sigma (T^4 - T_0^4) \quad (18)$$

where ϵ_t is emissivity, σ is the Stefan-Boltzmann constant, T is the melt pool temperature (K), and T_0 is the ambient temperature (K). Convection loss assuming a concentrated heating zone is expressed by Eq. 19:

$$Q_{convection} = A_l h_c (T - T_0) \quad (19)$$

where h_c is the heat convection coefficient (W/m^2K). The experimental expression for h_c is (Eq. 20):

$$h_c = 24.1 * 10^{-4} \epsilon_t T^{1.61} \quad (20)$$

The non-linear term, $T^{1.61}$, may be ignored for simplification.

$$Q_c = \rho c_p \int_{V_s} T(x,y,z,t_i) dV_s \quad (21)$$

V_s is the heat-affected volume (m^3), and ρ is the average density in the clad region (kg/m^3).

2.2.3 Solidification

Fundamental to the successful implementation of a DED process is the resulting microstructure, which plays a large role in determining the resultant mechanical properties. DED variables such as the thermal cycling, chemical reactions within the melt pool, alloying, and contaminants significantly affect the deposit and HAZ microstructures. The relationship between solidification behavior in the fusion zone and the size and shape of the grains, extent of segregation, and the distribution of inclusions, porosity, and hot cracks has been well-studied in the literature.

The main components that influence the solidification mechanics and microstructure are the temperature gradient (G), growth rate (R), undercooling (ΔT), and alloy composition (C_o). Laser processing involves a highly localized heat source with an interaction time equal to the product of the laser diameter and the scanning speed (e.g. 0.2 s for a 1mm spot size laser and a 300 mm/min scanning speed). The short interaction times coupled with rapid heat transfer by conduction into the substrate – occurring when the substrate is large compared to the region of the localized heating – leads to high solid/liquid interface velocities. The conductive heat removal is highly directional, setting up steep positive temperature gradients in the melt pool ahead of the solid/liquid interface [41]. A schematic of the solidification geometry for coaxial blown powder laser cladding is displayed in **Figure 3**.

The rate of solidification as indicated by the velocity of the solid/liquid interface, S, can be related to the scanning velocity using Eq. 22:

$$S = T_s cos\theta \qquad (22)$$

θ represents the angle between the vector normal to the solid/liquid interface and the vector aligned with the direction of motion. Based on **Figure 3**, it can be seen that the solid/liquid interface velocity varies from 0 at θ = 90° to T_s at θ = 0°. It can be seen from the figure and analysis that both solidification rate and temperature within the melt pool vary significantly, thus a different microstructure develops spatially throughout the melted region.

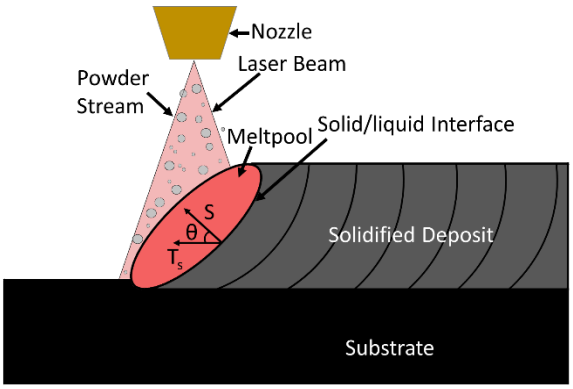

Figure 3: *Schematic of solidification geometry in coaxial laser cladding with blown powder feedstock*

The exact modes of solidification and microstructure present within in the specimens analyzed in this study are further presented in Section 4.4.2, but a brief overview of solidification is presented here. DED is similar to a welding process in that filler material is fed into a region of molten metal created using a localized heat source. The main difference between the processes is that welding is most often used to join pieces of metal, whereas DED is used to create new, independent geometric features. Thus, an understanding of solidification mechanisms present within welding processes can be helpful when applied to DED, as well.

In welding, solidification can come in the form of nucleation and growth mechanisms, or just through growth mechanism. This characteristic is largely due to the similarities between the deposited material and the base material. When the compositions differ greatly, solidification occurs

by nucleation and growth mechanisms, however, if the compositions are largely similar, then the dominating solidification is epitaxial growth originating from the liquid/solid boundary.

The two main factors controlling the modes of solidification relate to the kinetics of the liquid-solid interface –G and R – the travel speed of the liquid-solid interface. The four modes that can arise based on the relative behavior of the G and R values are planar, cellular, columnar dendritic, and equiaxed. The ratio between the two factors, G and R, determine the mode of solidification and the product of the two can serve as an indication of the cooling rate, which effects the level of refinement of the resulting grain structure (***Figure 4***).

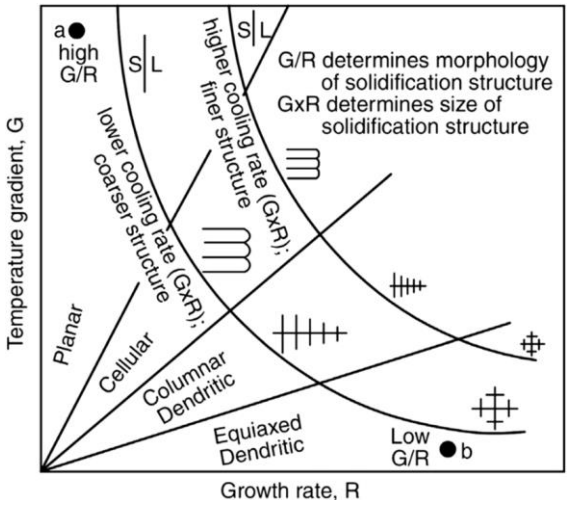

Figure 4: *Influence of G and R on solidification mode and grain structure [42]*

Grains may be single crystal in pure metals or polycrystalline aggregates in alloys. Individual grains experience anisotropic behavior, as behavior is dependent on crystallographic orientation, so, nominally, polycrystalline material is isotropic due to the random distribution of crystallographic orientation. Anisotropy, however, can be introduced into a material if certain orientations experience preferential growth. The number of nucleation sites and the growth rate of each nucleated crystal influence the grain size. As the grains grow, they eventually interfere with and impinge upon one another. Grain boundaries refer to the surfaces that separate individual grains. Grain size influences

mechanical behavior of metals; large grains generally result in low strength, low hardness, and high ductility. Grain boundaries serve as pinning point, interfering with the movement of dislocations and their propagation. As lattice structures in adjacent grains differ in orientation, it requires additional energy for a dislocation to change directions and propagate into the adjacent grain lattice. Grain boundaries are also much more disordered than the structured lattices within grains, which prevents the dislocations from moving along continuous slip planes. Under applied stress, as existing dislocations move to the grain boundaries, they generate repulsive stress fields due to atomic mismatch. As a result, dislocations pile up at grain boundaries which then serve as further barriers to slip. By impeding the free movement of dislocations, the material will experience a higher yield strength, as the onset of plasticity in hindered. The relation between grain size and yield strength can be expressed mathematically by the Hall-Petch equation (Eq. 23) [42]:

$$\sigma_{YS} = \sigma_0 + \frac{k_y}{\sqrt{d}} \quad (23)$$

where, σ_{YS} is the yield stress, σ_0 is a constant describing the resistance of the lattice to dislocation motion, k_y is a strengthening constant intrinsic to the material, and d is the average grain diameter, which can be determined using the ASTM E112 method for grain size measurement. Under large deformations, such as those seen in forging or sheet bending, large grains result in rough surfaces generating a so-called “orange peel” effect.

2.2.4 Porosity Formation

Depending on the ending application, macro- and micro- structure deviations from what is nominally desired are considered to be an anomaly or a defect. Macrostructure defects may include dimensional or surface roughness issues, whereas microstructure defects may arise in the form of porosity, lack of fusion (LOF), microcracking or hot-tears, severe variations in crystallographic texture and grain size, elemental segregation or variations in composition, undesirable secondary phases, and non-metallic inclusions [43]. These defects lead to unwanted mechanical properties and

increase the variance in stochastic behavior from sample-to-sample and build-to-build, leading to challenges in qualifying components' behavior. Porosity is a common defect present within many parts produced using AM processes. There are many contributing factors to the formation and extent of porosity within a printed specimen, however on the macro-scale they can be categorized into two main groups: gas porosity and LOF [44].

2.2.4.1 Gas Porosity

Current research suggests that gas porosity is largely attributed to entrapped shielding gas that occurs due to three main causes. The first is when a high powder flow rate is used, lowering the specific energy of the melt pool and making it more susceptible to gas entrapment. Gas porosity may also arise due to the presence of porosity and entrapped gas within the power feedstock. Finally, gas retention bubbles within the melt pool may form due to strong Marangoni flow [45]. Gas porosity tends to form smaller, more spherical voids that are more randomly dispersed throughout the build and is sometimes referred to as intralayer porosity.

2.2.4.2 LOF

Interlayer porosity, including LOF defects, tend to form larger, non-spherical voids closer to the substrate when heat is diffused away from the process zone rapidly. LOF defects form as a result of insufficient thermal input necessary to achieve satisfactory melting and metallurgical bonding of the powder and the parent material. Barua et al. cite issues such as incorrect or varying standoff distance between the deposition head and substrate surface causing further defocusing of the laser beam and reduced energy density [45]. As such, LOF defects are larger and more irregularly shaped compared to gas porosity and appear along layer-layer boundaries. Unmelted powder particles are often seen on fracture surfaces that fail due to unacceptable presence of LOF defects.

2.2.5 Residual Stresses

As a result of the intense localized heat and short interaction times with the laser, steep thermal gradients form between the molten deposit and the "cold" substrate, or adjacent deposited material. During the first stage of rapid cooling, the molten material shrinks but is restricted by the surrounding material, which leads to the formation of tensile stresses within the material [46]. The magnitude of the tensile stress is dependent on the coefficient of thermal expansion of the deposited material, its Young's Modulus, and the difference between the deposit melting temperature and the process temperature of the substrate. Plastic deformation and creep may serve to relax these initial tensile stresses. During the second stage of cooling, from the processing temperature down to ambient temperature, additional residual stresses develop. The signs and magnitudes of the residual stresses are dependent on the differences in melt pool and substrate temperatures, the ratios of coefficients of the thermal expansion, the material mechanical properties, the rate of cooling, and any solid-state phase transformations resulting in further changes in volume [46]. The presence of residual stresses can result in premature failure due to distortion, delamination, and cracking.

2.3 AISI 316L Stainless Steel

Austenitic steels (2xx and 3xx series) are non-magnetic, non-heat treatable, and contain high levels of chromium and nickel and low levels of carbon. Known for formability and resistance to corrosion, austenitic steels are the most widely used and have the largest number of alloys [47]. Austenitic steels are defined by their face-centered cubic (FCC) crystal structure. This grain structure forms when enough nickel, an austenite stabilizer, is present in the alloy – about 8-10% in a standard 18% chromium alloy, as chromium causes a ferrite-stabilizing effect. Molybdenum maybe be added in small quantities to improve corrosion resistance. As there is no phase change upon cooling, austenitic steels are only hardened through cold working and not by heat treatment. Austenitic stainless steels possess a wide range of desirable mechanical properties, including excellent low-

temperature toughness, good weldability, corrosion-resistance, and usually excellent cryogenic properties due to no ductile-brittle transition temperature.

Type 316 stainless steel is an austenitic chromium-nickel stainless steel with 2-3% molybdenum, which serves to increase corrosion-resistance and strength at high temperatures. 316 is very effective in acidic environments such as sulfuric, hydrochloric, acetic, formic, and tartaric acids, as well as acid sulfates and alkaline chlorides. It is often used in the construction of furnace parts, heat exchangers, jet engine parts, pharmaceutical equipment, valve and pump parts, chemical processing equipment. It also is used in pulp, paper, and textile processing equipment, and any parts exposed to marine environments.

Type 316L stainless steel is an extra-low carbon version of the 316 steel alloy. When austenitic stainless steels are heated, as in welding, carbon forms chromium carbide that precipitates on the grain boundaries. Corrosion can take place along the austenitic grain boundaries, as well as in those regions from which the chromium has been depleted to form the carbides. Consequently, 316L is used when welding is required in order to ensure maximum corrosion resistance (**Table 2**). Recently, 316L SS has found use in nuclear science applications as a material for nuclear fuel clad tubes and fuel sub assembly wrappers in fast breeder reactors [8]. ***Table 3*** compares the chemical compositions of the normal and low-carbon versions of 316.

316L has proven to be a popular material system for developing DED and other additive processes as it is relatively inexpensive and has a wide range of applications; as such, it has been selected for detailed analysis in this study.

Table 2*: 316 vs. 316L*

316	316L
• Contains more carbon • More liable to weld decay • Effective in acidic environments	• Contains less carbon • Better for avoiding welding corrosion • Good for high-temperature, high-corrosion use

***Table 3**: Chemical composition of type 316 and 316L stainless steel*

Element	316 Content (wt %)	316L Content (wt %)
C	0.08 max	0.03 max
N	0.10 max	0.10 max
S	0.03 max	0.03 max
P	0.045 max	0.045 max
Si	0.75 max.	0.75 max.
Mn	2.0 max	2.0 max
Cr	16.0-18.0	16.0-18.0
Mo	2.0-3.0	2.0-3.0
Ni	10.0-14.0	10.0-14.0
Fe	Balance	Balance

2.4 Tensile Testing

Tensile testing is used in this study as the foremost method for quantifying the difference in mechanical behavior of the different wrought-AM components studied. In qualifying a new material or manufacturing process, it is necessary to subject samples to a battery of mechanical tests. It is paramount to test the samples in conditions that allow engineers to say, with some degree of confidence, that the parts will behave as intended for the given application. The mechanical behavior of a part refers to its response to an applied load or force; several of the most important mechanical properties are strength, hardness, stiffness, and ductility. Tensile tests are the most common and widely performed mechanical property test. They are used to describe the elastic behavior of a part, which is relevant for the elastic design of structures. This type of test also provides information on the plasticity and fracture characteristics of a material. As the test is relatively easy and cheap to perform, and the stress state is well-established, it has been carefully standardized. Thus, uniaxial tension testing provides engineers with a convenient tool for comparing the behavior of different materials, selecting materials, quality assurance for new materials and processes, and to predict the behavior of materials under forms of loading other than uniaxial tension.

Throughout the duration of a tensile test, the tensile force applied by the testing machine is recorded as a function of the increase in gage length of the specimen as shown in **Figure 5**. The force

and change in gage length values are normalized with respect to the specimen's initial dimensions (Eq. 24).

$$Engineering\ stress\ (\sigma) = F/A_o \quad (24)$$

F is the tensile force, or load, and A_o is the initial cross-sectional area of the gage section.

$$Engineering\ strain\ (\epsilon) = \Delta l/l_o \quad (25)$$

l_o is the initial gage length and Δl refers to the change in gage length (l-l_o). The force-elongation curve can be converted into a stress-strain curve with identical shape, but that is more easily compared across multiple specimens. Using Hooke's law, it is possible to approximate the uniaxial stress relation within the proportional or linear section of the plot (Eq. 26):

$$\sigma = E\epsilon \quad (26)$$

E, the constant of proportionality, which corresponds to the slope of the linear region, is called the Young's Modulus or modulus of elasticity. E describes the stiffness of the material, and, because strain is unitless, is expressed in the same units as stress.

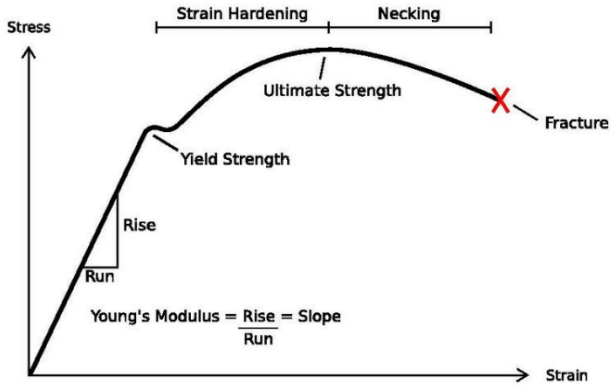

Figure 5: *Representative stress-strain curve of elastoplastic strain hardening material [48]*

The next important point on the curve is the elastic limit of the material – the point where deformation is nonrecoverable and any further deformation is said to be plastic rather than elastic. Beyond this point, the material is permanently deformed even when the load is removed. With the application of additional tensile loading, many materials reach the yield point, where there is a drastic

increase in strain without a corresponding increase in stress. This point can be difficult to determine, so a standard method used to determine this point is to use the 0.2% secant offset method, a graphical technique where a line is drawn with a slope E and intersects the x-axis at .002 mm/mm. The point where the line intersects the stress-strain curve is the graphically determined yield point and is significant in the design of mechanical structures.

The ultimate tensile strength (σ_{UTS}) represents the maximum stress experienced by the specimen in the stress-strain diagram. At the point of σ_{UTS}, the component begins to fail. After σ_{UTS}, many ductile materials experience necking, where there is a rapid reduction in cross-sectional area of the specimen, causing the strain to increase with a corresponding decrease in applied stress. Thus, ductile materials will experience a maximum stress well before fracture. Prior to the maximum stress, deformation is uniform along the length. However, when the maximum is reached, localized deformation forms a necked region with reduced area. As the cross-sectional area is reduced, all further deformation prior to fracture occurs in the necked region. In **Figure 5** a downward trend is seen until fracture occurs at some maximum elongation point, which depends on the *ductility* of the material. Other materials fail while the stress-strain trace is still rising, thus σ_{UTS} and the fracture point are identical; this is a characteristic of brittle material, though it is possible to see this type of failure in non-brittle materials, as well.

Work hardening, or cold working, is a metallurgical process which takes place when a material is strained beyond the yield point, below the recrystallization temperature. As the metal is further strained, additional stress is required to produce additional plastic strain, and the metal appears to become more difficult to deform. A metal possessing a higher shear modulus will have a higher strain hardening coefficient. Grain size also influences strain hardening, with small grains experiencing more rapid strain hardening than the same material with a larger grain size. This grain size effect on work hardening rates is only prevalent in the early stages of plastic deformation, and

grain size plays less of a role as the structure undergoes more serious deformation, as the grain structure breaks down.

Results of tensile tests are sensitive to both intrinsic material properties, such as grain size, impurities, texture, residual stress, and voids, and extrinsic geometric and surface properties, including cutting method, sample geometry, and surface roughness of the specimen. The test's sensitivity to both intrinsic and extrinsic attributes can make it challenging to compare results tested in the lab to differently prepared specimens tested under dissimilar conditions. Therefore, it is imperative to report the exact specimen preparation methods and test conditions used. Tensile testing, unlike uniaxial compressional and nanoindentation testing, is more sensitive to porosity and weak welding with regards to AM materials, making it a particularly useful test for the evaluation of AM mechanical properties.

2.5 Anisotropy in Layer-Base Additive Manufacturing

As a result of the layer-by-layer nature of the DED process, anisotropies arise in the resulting deposited material. After a CAD model has been generated for a layered manufacturing (LM) process, the next fundamental problem becomes determining the optimal orientation of the part within the build volume. The goal of the process design is to meet the required surface quality and geometric accuracy, while also minimizing material consumption and build time. Therefore, it necessary to understand the exact nature of the anisotropies that develop within the part so that the engineer can determine how to design and build the components efficiently, while also ensuring that the part meets its intended function. Anisotropies in DED and some of the LM processes manifest themselves in several different manners, impacting the produced surface geometry, the internal microstructure, and mechanical properties.

One example of an interesting application for applying additional understanding the relationship between layer oriented and direction of tensile stress is in the construction and modeling of lattice structure, also referred to as an architected structural material. Depending on the geometry of the unit cells composing the structures, the struts are subjected to loading conditions at different orientations with respect to the build orientation. This is due to the way stress propagates through the structure and the orientation of the strut within the cell. Analytical and finite-element models have generally utilized isotropic material properties to design and predict lattice structure performance, however,

The surface quality of the part is essential in determining the part's ability to meet the dimensioning and tolerancing requirements. Dimensioning and tolerancing is used to ensure that manufactured parts meet their design intent, which involves both integration into larger assemblies and ensuring the part fulfills its intended functional requirements. The aesthetic finish of the part is often of secondary importance, but sometimes may be a very critical requirement, so its significance cannot be understated. Factors that affect surface quality in DED and other LM processes, such as L-PBF and FDM, are powder and feedstock size, as well as process variables like layer thickness, build direction, and support material. The "stair-stepping" effect is a consequence of the limitations of the layered nature of the process attempting to generate surfaces inclined to the deposition plane. The exact roughness of the stair-stepping effect can be analytically determined based on the layer thickness and the angle of inclination. The part orientation within the machine may be chosen to minimize this phenomenon on critical surfaces. In addition to affecting surface finish, the staircase effect influences the geometric accuracy achievable in the XY-plane versus the XZ- and YZ-planes .

The use of additional structures necessary to support the construction of overhanging surfaces are another necessary process design consideration in LM processes. However, the increased degrees-of-freedom (DOF) available in DED processes allow for the minimization of their use. In L-PBF, support structures serve additional purposes like anchoring the part to the build plate in the

face of high residual stresses and conducting heat away from the melt pool. At the end of the print, the support structures need to be removed, often leaving a small defect on the surface to which they were affixed. Build orientation in LM processes is often dictated by the desire to minimize the use of supports, to lessen build costs associated with printing and removing those features, and to protect critical surfaces. Post-processing of these surface defects is often required to make the additively-made component fully functional and able to be integrated into a larger assembly. The advantages of DED-based hybrid manufacturing are the additional deposition DOF that the machine tool provides, as well as the seamless integration with post-processing capabilities. Thus, the sequence of deposition and machining toolpaths can generally be designed in such a way that yields high quality surface finishes, and, as such, build orientation effects on surface quality, dimensional accuracy, and support structure use is not considered in this body of work.

Often in a repair process, an initial "cut-back" machining operation is required to restore damaged or contaminated surfaces to a clean and uniform surface onto which the feedstock material can be successfully deposited. In order to minimize cycle time and material costs, the process design objective is to remove as little material as possible to generate a machined surface that requires the minimum amount of additional material to be added on. In order to minimize the amount of material added, it may be necessary to consider the use of different layer orientations with respect to the overall part coordinate system.

When approaching the problem of layer orientation selection, it is essential to know the way in which the fusing of one layer to the next affects the microstructure and resulting properties in each direction within the material. The combination of process parameters (laser power, powder mass flow rate, laser scanning speed, melt pool size, etc.) result in a heat transfer problem that contributes to the growth of a microstructure unique to metal AM, and the development of porosity and other internal defects, both of which cause an anisotropy of mechanical strength [23]. It has been demonstrated within the literature that the highly localized rapid thermal cycling in DED results in

inhomogeneous grain morphology throughout the part . The properties within a single as-deposited track differ from the fused regions between adjacent tracks, as well as between the stacked layers . Lack-of-fusion (LOF) defects such as porosity and unmelted powder particles are more likely occur between layers as opposed to within a layer .

As a result, parts produced using DED and other layer-based manufacturing methods may exhibit anisotropic mechanical properties that need to be taken in consideration when determining the build orientation for a part in order to meet the part's functional requirements. Furthermore, the complex relationship that exists between process, structure, and mechanical properties still needs to be vigorously investigated to further the industrial acceptance of DED and hybrid manufacturing. The anisotropies in LM process have been known to exist and studied for some time. However, the advancements in robotics, controls, and machine tools has cause a surge in related publications.

CHAPTER 3: LITERATURE REVIEW

In order to determine the best methods for undertaking a study on anisotropy in hybrid wrought-AM components, it is necessary to explore the previous body of research that has been carried out within this field. Dressler et. al. determines that LM processes produce heterogeneities in surface topography that influence the mechanical performance of small metallic features [48]. This team investigates strut performance in L-PBF-produced 17-4PH lattice structures and finds that heterogenous surface topology is due to print orientation-generated stress-concentrating contours and deviations from the nominally cylindrical features.

Other research such as Agarwala et al., Chlebus et al., and Buchbinder et al. appreciate the significant role that build orientation plays in tensile strength and decide to study its effects on SLM produced bronze (Cu-10wt%Sn)-nickel, Ti6AL7Nb titanium alloy, and AlSi10Mg aluminum alloy [49]–[51]. Agarwala et al. research build-up direction effects on tensile strength of SLM, as well as the impact of laser scanning direction. They find that scanning direction plays a significant role in the observed strength of the components, with the longitudinal scanning direction measuring 40 MPa and the transverse scanning direction measuring 60 MPa. While not strictly investigating the layer orientation effects, their results highlight an important phenomenon that is relevant to this study – they attribute the differences in observed strength to the scan vector length for the particular scanning orientation used. A shorter scan vector results in a better sintered part because there is less time for the temperature to decay between adjacent tracks. Kruth et al. demonstrate that short scan vector lengths contribute to greater localized net energy due to the shorter time interval until the laser scans the region of the successive track [52]. A longer path length allows for localized heat to dissipate and results in lower net energy as the laser rescans the region. Scan vector lengths are also a function of layer area, with larger areas leading to longer time intervals and increased localized temperature decay.

Additionally, Chlebus et al. study the mechanical properties of additively manufactured Ti6Al7Nb alloy components [50]. Chlebus and co-investigators find the modulus of the sample built in the z-orientation to be 15% higher than the stated bulk wrought modulus found in the literature, but 16% lower than specimens built in x and y directions. They obtain intermediary modulus values for the specimens produced at 45° to the long axis of the specimen. Samples built in the y-direction have slightly higher yield and tensile strength, and lower elongation, compared to x-direction samples reflecting the observations of Agarwala et al. [49]. Chlebus et al. are convinced that, due to similarities in the pore orientation and solidification direction between the x and y build directions, the influence of build direction is related to resulting distribution of residual stresses in the material. They conclude that differences in elasticity can be attributed to the different distribution and level of residual stress. When compared to z-direction built parts, the z-direction parts experience drastically lower tensile strength values, which is attributed to build defect morphology. Interlayer porosity formed in the z-built parts possess surfaces in the xy-plane, perpendicular to the specimen axis. The resultant small tip radii of the flat-shaped pores causes stress concentrations in the region in front of the defect tip, effectively magnifying the applied stress. The higher number of layers required to build tensile specimens in the z-direction result in a higher number of pores, as well as a higher level of residual stress within the material.

Buchbinder et al. investigate SLM-produced AlSi10Mg alloy and determine that the specimens with the layer orientation parallel to the tensile direction (which would be considered to be a 90° orientation within the naming conventions of this current study) have the highest σ_{UTS} at 420 MPa, whereas the layer orientation perpendicular to the applied load (0° in the current study, as the surface normal is parallel to the tensile axis) has the lower tensile strength of 360 MPa [51]. Even though a different material system is used, the reduced σ_{UTS} of the perpendicular/0° build orientation corroborates the reduced strength in the z-built direction observed by Chlebus et al [53].

While the above work serves to introduce some of the theories and reasoning authors have developed to which they attribute anisotropic properties, other groups of researchers have performed similar analysis on austenitic stainless steels like the 316L analyzed in the current study, the results of which are outlined in **Table 4**. Smith et al., for example, perform tension-tension and cyclic fatigue tests on DED manufactured 304L stainless steel parts in both horizontal and vertical build orientations [54]. Through studying the orientation effects on tensile behavior of additively manufactured austenitic stainless steel, they discover that by changing build orientation alone they are able to obtain a 25% increase in yield strength. Changing build orientation from vertical to horizontal results in a 25% difference in yield strength, 9% increase in ultimate tensile strength, and a 27% decrease in maximum elongation, as well as strongly influencings fatigue behavior. The disparity in mechanical properties is attributed to a difference in manufacturing defect populations for the different orientations.

Shrestha et al. deliver similar results for 316L SS parts produced by L-PBF [55]. They conclude that, despite the presence of LOF defects between layers, the specimens all exhibit higher yield strength, ultimate tensile strength, and elongation to failure when compared to wrought material. This result remains true despite changes in layer orientation and surface roughness condition. They attribute the variation in elongation-to-failure measurements to the orientation dependency of the epitaxial elongated grains, which align themselves perpendicularly to the build plate. As fatigue performance is also of significance to industrial applications, they also report that the effect of layer orientation is minimal in the presence of plastic deformation during low cycle fatigue, but, in general, the least fatigue strength belongs to diagonally-built specimens and the highest belonged to the horizontal (90°) specimens. Variations in fatigue failure are found to be largely a result of the projected LOF defect area on the loading plane for the different orientations.

Table 4: *Summary of Build Orientation Effects on Tensile Properties*

Material	Process	Orientation	Modulus (GPa)	Yield (MPa)	σ_{UTS} (MPa)	Elongation (%)	Authors
316L SS	SLM	YX (90°)	-	397	668	37	Alsalla [56]
		XZ (90°)	-	423	695	41	
		ZX (0°)	-	387	564	35	
304L SS	DED	V (0°)	-	440	670	70	Smith [54]
		H (90°)	-	552	730	51	
316L SS	LENS	Axial (0°)	-	448/455	545/638	4/25	Yang [57]
		Transverse (90°)	-	538/552	690/703	35/38	
AISI 316L	HP DLD	Parallel (90°)	199	580	900	6.5	Guo [58]
		Normal (0°)	197	415	770	4	
316 SS	LBAM	0°	-	558	639	21	Zhang [59]
		90°	-	352	536	46	
316L SS	L-PBF	Horizontal (0°) – Machined	172 (cyclic)	545	689	29	Shrestha [55]
		Horizontal (0°) – As-built	Not Reported				
		Vertical (90°) – Machined	163 (cyclic)	495	587	59	
		Vertical (90°) – As-built	165 (cyclic)	485	594	58	
		Diagonal (45°) – Machined	211 (cyclic)	573	722	48	
		Diagonal (45°) – As-built	196 (cyclic)	535	697	50	

There appears to be little consensus within the literature as to a single factor that can be named as the foremost reason why anisotropic mechanical properties exist; in reality it is most likely a contribution of numerous different sources. There are, however, many theories about which factors are the most influential. The orientation of the layers in DED is known to result in changes to defect size, shape, and distribution, microstructure size and morphology, mechanical fibering, and residual stress distribution. Each of these properties may drive the degree to which anisotropic mechanical properties exist. Still, it is not well understood which of the properties is primarily driving the mechanical property variability, and it also depends on the material and AM process utilized.

Selecting a build orientation affects the structure of the part in several important ways. First, it sets the number of layers required to successfully construct the geometry, as well as determining the per-layer cross-sectional area. If a constant laser power and scanning velocity are used, then the

per-layer cross-sectional area has a directf impact on the per-layer deposition time. The number of required layers is significant because, in the presence of interlayer porosity, it leads to a higher density of defects projected onto a plane normal to the tensile direction. Practically speaking, a greater number of layers may also lead to a higher chance of deviating from the nominal standoff distance. If there is any semblance of a mismatch between the programmed layer height and the actual layer height – which may also change throughout the build, as the part heats up – this chance increases. Another effect of having more layers is the possible prevalence of more residual stress present within the material.

Additionally, changing the build geometry and per-layer deposition time changes the solidification conditions present, as larger layers lead to higher localized temperature decay, which, in turn, impacts both the net local thermal energy and defect formation, as well as grain growth. As the deposited layer increases in size, and the scanning speed remains constant, the time between when the laser scans the same XY location (for planar and UV for non-planar) on the next layer increases. The significance of this fact is that the residual heat will have dissipated more as the layers increase in size due to the added time required to produce each layer. Also affecting the amount of residual heat is the geometry of the parent and deposited material. The solidification rate of the molten material is largely dependent on the geometry of the component being deposited. Smith et al. argue that for fully dense materials, the variability in mechanical properties stems from variability in the microstructures; they also note that the specific role various microstructural features play in materials performance (e.g., strength, ductility, fracture resistance, fatigue behavior) has yet to be fully delineated .

In addition to governing grain size formation, secondary dendrite arm-spacing solidification rates also affect element segregation and matrix depletion. The solidification rate refers to the rate at which the solid/liquid interface advances into the liquid. The rate at which the solid/liquid interface

advances is critical in determining the extent of solute distribution upon solidification and microstructure growth. As the solidification occurs more rapidly, the tendency of elemental segregation is minimized. Mechanical fibering refers to the alignment of impurities, inclusions (stringers), and voids within the structure of a material during deformation. Impurities cause a weakening of grain boundaries. For example, when metals that contain equiaxed grains with impurities present along the boundaries are subject to cold-working, the impurities align themselves horizontally in compression and along the axis of tension for tensile testing. Some researchers credit the formation of pores and voids in the cladded region as the foremost factors affecting tensile properties. Metallurgical defects such as pores, cracks, foreign inclusions, and other phases are more easily introduced into the bonding area between layers, thus, parts fabricated in the vertical direction may possess inferior tensile properties to those produced in the horizontal direction.

Changing the cross-sectional geometry of the component layers influences the complex thermal cycling behavior during the build, but also the solidification mechanism alone induces a grain structure that is not isotropic in its nature. It has been shown that preferential grain growth occurs along the direction of cooling, thus producing non-equiaxed columnar grains along the melt pool boundary. Columnar grains possess aspect ratios not equal to 1. As the primary thermal gradient changes direction, it causes variations in the effective grain size along the tensile axis.

While DED-produced austenitic stainless steels have been studied extensively in the literature, there is little work performed in thoroughly mapping the evolution of build orientation's effects on mechanical properties. What researchers have reported on is the presence of monotonic mechanical behavior, heterogenous microstructures, and manufacturing defects produced in the materials by the DED process [60]. Olakanmi et al. has highlighted the deleterious effects that voids and cavities have on elongation to failure [61]. From Olakanmi et al.'s work it appears that the porosity level has a dominating effect on mechanical performance, so in comparing the results of build

orientation, the behavior largely depends on the internal defects present. If the defect distributions are significantly different, then it will overshadow other sources of anisotropy. However, the level at which a certain minimum density causes property variation to transition to be dependent on grain structure is not clearly demarcated.

In Chlebus et al., the poor tensile strength of the z-direction-built specimens is postulated to be associated with the increase in stress concentrations, due to the flat pore shape with small tip radii on the edges perpendicular to the stress direction [50]. However, porosity also has an impact when considering the increased pore area fraction for each slice, which results in a reduced load bearing area. It is apparent that the porosity mode that may cause anisotropy is interlayer porosity, related to lack of fusion defects and insufficient melting and bonding of the parent and filler materials. These conclusions are further advanced by Smith et al. [54].

While many researchers have looked at purely additively produced components, the purpose of this study is to understand how variations within the additive region of material impact the bulk performance of a bi-metallic wrought-DED specimen. Additionally, in hybrid, bi-metallic components the interfacial bonding of the two regions is also important to investigate. Weak interfacial adhesion can incur premature failure due to detachment or cracking along the interface region. Most interest in hybrid components has been limited to wear and hardness properties relevant to laser clad metallic coatings, such as in hard-facing applications. However, for larger scale components and repairs, multi-layer deposition is unavoidable, and additional study of the bonding and mechanical behavior of half-wrought half-additive components is vital. In practical applications, the interfacial bonding strength and the mechanical properties of the bulk multi-material component should be similar to or exceed that of the parent material [62], and tensile testing is determined to be a satisfactory method for this evaluation and comparison.

Few studies have focused on wrought-DED specimens in this manner. The studies have been limited to nickel-based deposits [27][28], and one such study is from Kim et al. , examining AISI 4140 [65]. In bi-metallic materials, the interface bonding between the laser-repaired region and the original parent material plays a vital role in determining the overall performance of the component .[66]. Kim et al. find that all 4140 half-wrought half-additive tensile specimens fractured in the additively produced region of material. As no specimens are shown to fail in the interface region, they are able to deduce that the as-deposited AM material suffers from less inter-layer bond strength than the bonding strength between the AM and wrought material. In terms of analyzing stress-strain behavior, the tensile properties of the samples represent those of the fracture region of the specimen. As compared to the wrought material, their as-built hybrid samples show 50% lower σ_{UTS} with a 47% standard deviation, 36% of the wrought yield strength with 32% standard deviation, and almost half the maximum elongation with 65.2% standard deviation. The high variance in measure properties are attributed to metallurgical defects, which also result in largely brittle fracture [67].

The current study outlined in this paper seeks to expand upon the work performed by Kim et al. by investigating build orientation effects on tensile performance of 316L – a commonly used AM material – as well as interfacial bonding strength. The orientations of 0°, 15°, and 30° are investigated to develop a higher resolution empirical model relating slight changes in orientation to behavior in multi-material wrought-additive components. The novelty of this work lies in the fact that few researchers have looked at hybrid manufactured components, and those that have were only concerned with the level of bonding at the interface region. Additionally, few researchers have investigated the effects of small variations in build orientations choosing instead to look at the difference between vertical, diagonal, and horizontal orientations. This research aims to show that build orientation matters – even in increments of 15° – and that those changes can be seen in both the bulk properties as well as the relative strain behavior between the AM and wrought regions.

CHAPTER 4: EXPERIMENTS AND RESULTS

4.1 Methodology

To investigate the phenomena outlined in the previous sections, this work is divided into subsections (miniature-experiments). The first priority is to determine the method with which to produce the tensile specimens. This work includes specimen design and the development of the process through which differently oriented specimens will be generated. This study focuses on 0°, 15°, and 30° build orientations. 15° increments are selected because of the improved resolution provided over the previously reviewed studies, and the three orientations investigated are determined to be sufficient to reveal any variance in the properties. The selected tensile specimen size is chosen for ease of production and to reduce the number of overall printed layers required. However, it is recognized that a larger tensile specimen is easier to handle, load into the machine, better accommodate the contact extensometer, and help to minimize variation in mechanical properties resulting from deviations from a 50/50 composition of DED and wrought material in the gage section. The volume fraction of the tensile specimen belonging to each material should be one half (½), however as the gage length decreases, the more error there is if the interface does not exactly bisect the specimen. The volumetric fraction of each region is assumed to be ½, and, if the interface region is not perfectly in the middle, a longer specimen reduces the overall deviation from the nominal assumption.

Appropriate process parameters are identified in order to print a large block of bulk material from which the tensile samples are cut. A multi-level, multi-factor full factorial statistical analysis is performed to select process parameters that yield desirable single-track geometry. The microstructure of the produced bulk material is analyzed via optical microscopy and compared with what is expected in the literature. Computed Tomography (CT) inspection is utilized as a tool to non-destructively test for internal defects and voids within the printed samples, as it is presented in the

literature review that defect population and distribution plays a significant role in the resulting mechanical performance. The fracture surfaces are imaged using scanning electron microscopy (SEM) to try to determine the failure mechanisms.

4.2 Process parameter selection

4.2.1 Introduction to Process Parameter Selection

To build a multi-track, multi-layer, fully dense component, it is necessary to identify the appropriate process parameters for the material system, component geometry, and DED equipment in use. There are many process variables that can affect the resulting build quality and performance. Not only are there multiple inputs and outputs to consider, but the relations are nonlinear, and the input and outputs are highly coupled. The variables are divided into intrinsic parameters (those that cannot be easily varied) and extrinsic parameters (those that can be easily tuned). Some examples of intrinsic parameters are material composition of both the powder and substrate, substrate geometry, deposition geometry, powder shape and size distribution, laser wavelength and mode, and the environmental conditions within the machine. Other parameters, such as laser power, mass flow, traverse speed, toolpath design including hatch-spacing and z-increment, can be easily modified by the process engineer to ensure proper deposition and are there classified as extrinsic. Examples of some of the different variables influencing the quality of the deposit are presented in **Figure 6**.

Primary parameters in the DED process govern the resulting bead geometry and the degree to which it is bonded to the substrate and are the focus of the experiment performed in the following section. Primary parameters can be thought of as those that govern the deposition of a single track. Secondary parameters, such as hatch-spacing (the distance between the centerlines of adjacent, overlapping tracks) and z-increment (the distance upwards the cladding nozzle moves prior to deposing the next layer), are chosen based on the geometry of the deposited track. To select the

appropriate hatch-spacing and z-increment to build large, complex parts using DED that are free of voids, it is essential to control the geometry of single tracks of deposited material and understand the effect of various process parameters on the resulting clad geometry. Additionally, not only can morphological characteristics of a track be used to indicate the degree of metallurgical bonding achieved for a given material system, track shape can also indicate process efficiency [7][8]. Once single tracks are deposited, it is necessary to define the geometric traits that are considered desirable.

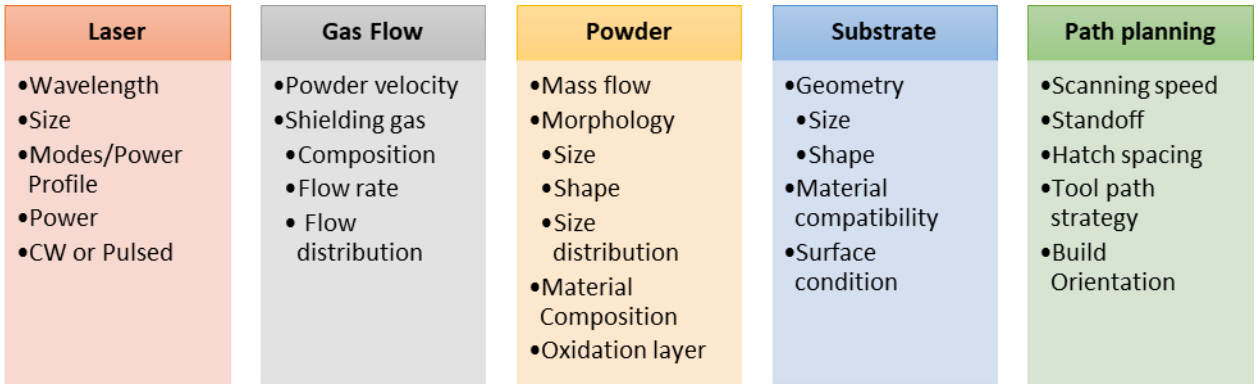

Figure 6: *Independent Variables in Directed Energy Deposition*

Primary parameter selection – those most easily tuned on the machine – are the focus of the following discussion. The metrics used to evaluate the quality of a deposited track are the width of the bead (w), the bead height (h), the penetration depth (b), and the wetting angle (θ). A diagram depicting the cross-section of a typical single track is shown in **Figure 7** [70].

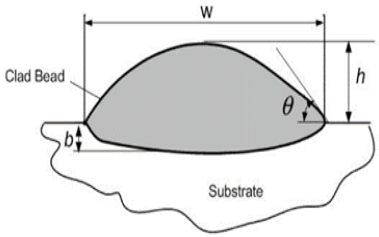

Figure 7: *Schematic of single deposited track cross-section* [37]

The two primary requirements that affect the performance of the DED-produced component, before fine tuning properties such as the microstructure, are the degree of bonding with the substrate and the formation of voids. These have been shown to occur between adjacent tracks generated under non-ideal conditions [10][11].

The desirable dilution (D) percentage, defined as the relative mixing between the molten clad and melted substrate, is dependent on the functional requirements of the component. For example, a cladding operation might want to achieve a lower dilution percentage so that as few layers as possible are used to transition from the base material to the clad material properties. However, in all applications, the dilution value should be low enough to ensure that the cladded material properties are not degraded by the substrates, while also high enough to ensure suitable bonding with the substrate [73]. The extent of dilution is the result of a complex function of the thermal energy input, process speed, and material deposition rate and can be represented as a ratio of the elemental mixing of the two materials. While the level of bonding does depend largely on the compatibility of the cladding and substrate material compositions, it may also be quantified geometrically using Eq. 27. [74] [41]:

$$D = \frac{b}{b+h} \quad (27)$$

The clad angle, another key factor in controlling the extent of void formation between adjacent tracks, may be calculated from the track width and height (Eq. 28):

$$\theta = 2arctan\left(\frac{2h}{w}\right) \quad (28)$$

A wetting angle that is too large may increase susceptibility to entrapped air between adjacent beads and result in increased porosity as seen in **Figure 8**. This is especially true when insufficient laser power is used to cause re-melting of the already-deposited adjacent track.

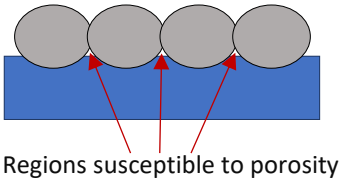

Figure 8: *Overlap regions susceptible to voids*

In practice, the clad angle should be small enough to ensure proper overlapping between adjacent tracks. A contact angle of less than 90° causes the bead to spread over the surface, which fills in the gaps between adjacent tracks and generates a fully dense layer. Beads that have very low wetting angles are considered to be excessively "wetted." Excessively wetted beads do not result in much layer height and are thus less efficient in terms of volumetric build rate, resulting in the need for more layers to achieve the desired build height. Too much spreading of the bead may signal excessive re-melting of already-deposited material, greatly affecting its grain structure, which could be undesirable depending on the component's application. As the clad angle is a function of width and height, it can be controlled by manipulating the aspect ratio of the bead, which is defined as the ratio between the width and the height of the clad (Eq. 29):

$$AR = \frac{w}{h} \tag{29}$$

Setting an upper clad angle limit of 90° results in an aspect ratio of at least 2:1. However, the literature suggests using a value of 3-5:1 [75] [76].

4.2.2 Statistics-Based Approaches to Modelling Single Track Geometry

While many researchers have attempted to model the cladding DED process and precisely control the bead shape through the manipulation of several key process parameters, there are so many variables involved in the process that it is necessary to adapt the existing research to the specific materials and equipment. The empirical models developed for single track cladding are developed for specific process conditions and may not be appropriate to use directly from one DED

system to the next. However, the various methodologies for developing the different models may be utilized and adapted to fit the specific machine and material configuration.

One of the most widely cited studies, conducted by Oliveira et al., examines how clad geometry may be controlled by tuning the heat transfer between the laser beam, substrate, and mass transfer between the powder flow and the molten surface [70]. They verify their theoretical model, examining 175 unique combinations of laser power (P), mass flowrate (Pf), and scanning speed (U). The researchers use a statistics-based approach to identify empirical relations between layer height, width, and dilution with specific combined parameters. Some of the most important of these combinations are the linear mass density – the amount of powder delivered per unit length, Pf/U (g/mm) – and the linear energy density – the amount of heat delivered to the substrate per unit length, P/U (J/mm).

Picasso et al. develop a simple geometric model for determining laser power and mass flow rate for a given set of laser power, beam radius, powder stream geometry, and clad heights while considering interactions between the powder particles, laser beam, and molten pool [77]. They assume particles are completely melted by the laser beam prior to reaching the melt pool. Toyskerani et al. take multiple approaches to predicted bread geometry. In one work, they utilize a numerical model to obtain deposited bead geometry and, in another published work, they employ a neural network and stochastic models to obtain clad height [78] [79] [80]. Furthermore, a simple lumped model, correlating laser clad track width and height with laser cladding operating parameters such as powder feed rate, is developed by Colaco et al. [81]. The process speeds and estimated powder catchment efficiencies can be obtained using their method. Based on a parametric study of clad geometry, Cheikh et al. develop analytical relationships between laser track geometric characteristics and select process parameters. By comparing various correlation coefficients, Cheikh et al. are able to identify the highest correlated combined parameters on which to base the model [82].

Farahmoud et al. uses response surface methodology (RSM) and a desirability function to map and optimize process parameter selection [83]. They conduct a multi-factor, multi-level statistical study of high-power direct diode laser fabrication of AISI H13. They form multiple regression second-order analytical models relating the main process parameters – laser power, powder flow rate, and HAZ – to geometric outputs such as height and dilution, and then use a desirability function to perform the multi-criteria optimization of parameter selection. Onwubolo et al. also used RSM mapping to model cladding angle response to laser power, scanning speed, and mass flow rate [84]. In their work, they present two different models, each one corresponding to a different range of the processing window. They fit a first-order model to a small window of processing parameters and then fit a second-order model, which covers a wider range of the processing window. Both models are tested with analysis of variance (ANOVA), and a scatter search optimization is performed to determine optimal process parameters.

4.2.3 Design of Experiment

While other researchers have developed various empirical laser cladding models, the process is sensitive to environment and equipment-specific process conditions, making additional studies in this area valuable. Even though one statistical model may be developed for a particular material and laser cladding system, the relationship among and the process' sensitivity to the different process parameters may change significantly when moving to a different material and equipment configuration. Thus, in order to build the tensile specimens used in this study, it is necessary to first perform a full-factorial parametric analysis of several laser cladding process parameters. Statistical methods are employed to model the relationship between various geometric properties of single tracks and the primary DED parameters: laser power, scanning speed, and mass flow rate. A correlation matrix is used to determine the linear correlation coefficients between various inputs and

outputs, while also providing insight into how the various outputs correlate to one another. Second-order polynomial models are fit to the data and verified using ANOVA.

The laser used in this study has a range of 100-1000W, so laser powers are selected that span the available processing window; the laser powers selected for investigation are 300, 450, 600, and 750 W. The main parameters influencing the powder stream are the powder flowability, the geometry of the deposition head, the flow rate of the carrier gas, and the mass flow of the powder. The powder used throughout the duration of this study is gas-atomized AISI 316L SS procured from LPW (now Carpenter Additive) with a specified size range of 44-106 μm. A small sampling of powder is imaged using a Zeiss Ultra 60 FE-SEM (**Figure 9**).

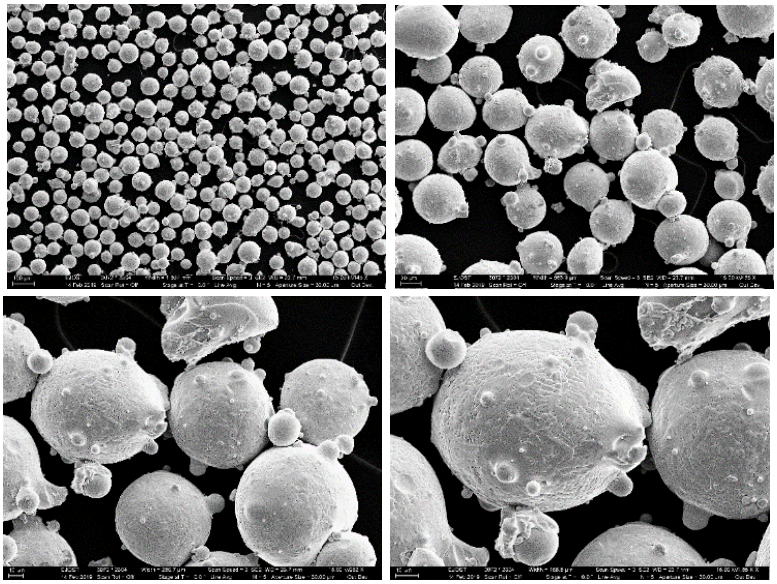

Figure 9: *SEM Images of gas-atomized 316L SS Powder Procured from LPW [85]*

It can be seen in the SEM images that the gas atomization method produces very spherical powders with some small satellite particles attached to the main particles. It has been demonstrated in the literature that it is desirable to have a decent spread in powder size distribution (PSD) for improving flowability. According the histogram of powder diameter as determined from the 2D SEM image, the PSD ranges from 60-120 μm for the powder used (**Figure 10**). As the same lot of powder is

used throughout this study, there should be limited variation in powder flowability due to changes in PSD or powder morphology.

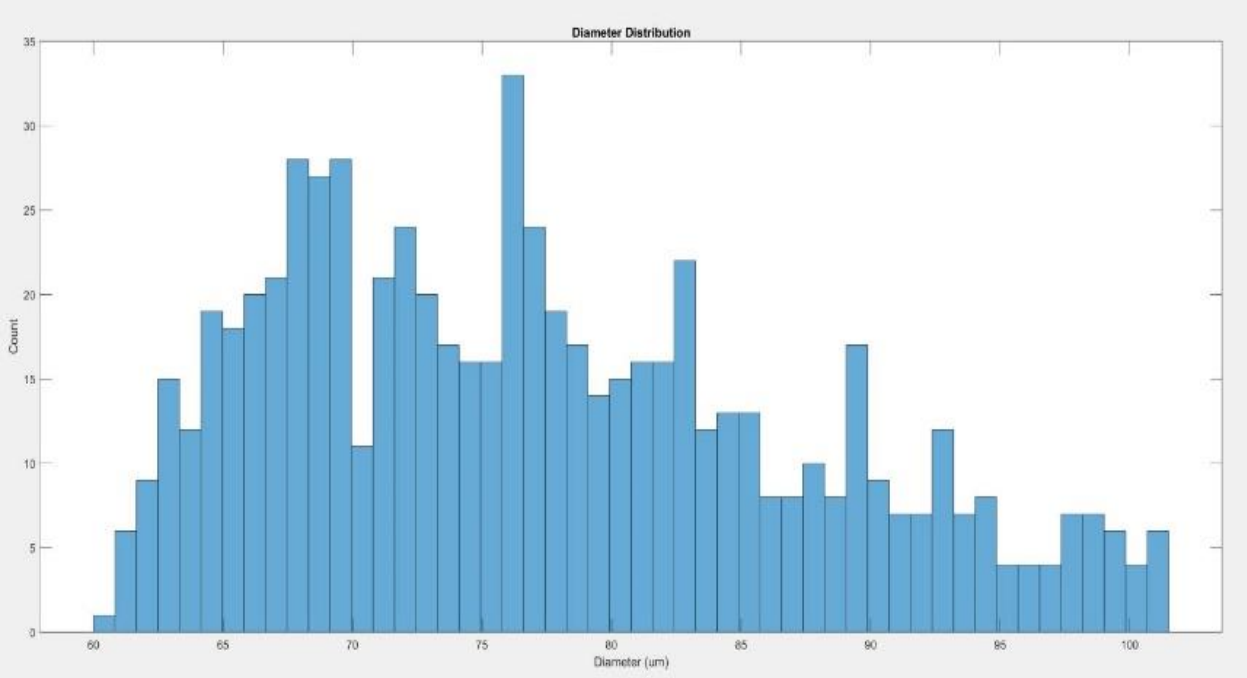

Figure 10: *Powder Size Distribution (PSD) Histogram of 316L SS gas-atomized powder [85]*

Humidity has a deleterious effect on powder flowability, as it is known to cause clumping that clogs narrow passages in the powder feed system. To aid in the prevention of moisture collection within the powder feeder, the powder is stored in air-tight containers with desiccant packets prior to loading into the hopper. Once loaded, the hopper is sealed and pre-heated to 60°C.

The engineer has the ability to regulate the carrier gas volumetric flow rate on the machine control. The carrier gas flow rate may be modulated throughout the program by re-running the macro subprogram that sets the cladding parameters, but it is held at a constant 5 L/min for this study. The carrier gas flow rate determines the velocity of the powder particles as they exit the deposition head. With the powder and carrier gas flow acting as a tightly coupled system, the carrier gas velocity at the nozzle exit can be assumed to be the peak powder stream velocity. Assuming incompressible flow

and a nozzle exit diameter of .676 mm, the peak powder velocity for a carrier gas rate of 5 L/min is approximately 92.9 m/s.

The mass flow is controlled by the duty cycle of a rotating metering disk, whereby increasing or reducing the rotational speed of the disk increases or decreases the amount of powder delivered to the melt pool, respectively. The available duty cycles range from 5-100% and 5 values are selected spanning the range. To determine the corresponding powder mass flow, the disk is operated at various speeds and the expelled powder is collected in a glass of water over a one-minute time period. The mass of the water is measured before and after. The process is conducted three times at each disk speed. The measurements are averaged, and a best fit line is determined based on the plotted values. **Figure 11** demonstrates that the mass flow increases in a nearly linear manner, which can be approximated by the best fit line with the equation (Eq. 30):

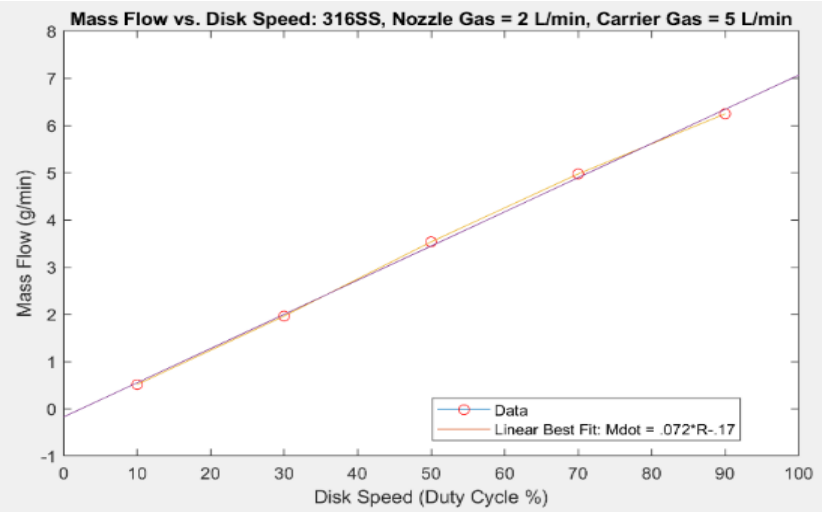

Figure 11: *Powder mass flow as a function of metering disk duty cycle*

$$Pf = 0.072 * D - 0.17, \text{ where } Pf \text{ is the mass flow, } Pf = \frac{dm}{dt}, \text{ and } D \text{ is the duty cycle} \quad (30)$$

With regards to traverse speed (U), six values are selected that represent a wide enough window of possible process speeds that good insight into the effect of traverse speed on bead morphology can be realized. The fixed DED process parameters are displayed in **Table 5**, and the independent variables and selected values are presented in **Table 6**.

Table 5: *Fixed process parameters*

Laser spot size:	1 mm
Nozzle stand-off:	5 mm
Nozzle Gas:	Argon, 2 L/min
Carrier Gas:	Argon, 5 L/min
Shielding Gas:	Argon, 6 L/min

Table 6: *Levels of independent variables tested*

Power (W):	300	450	600	750		
Traverse Speed (mm/min):	150	300	450	600	750	900
Mass flow (g/min):	.195	1.83	3.47	5.11	6.76	

A full-factorial experiment is conducted with the values selected in **Table 6**, depositing 120 unique combinations of process parameters on 0.250" thick 316L SS wrought substrate procured from Michlin Metals. Using wire electron-discharge machining (EDM), representative cross-sections of the deposited tracks are cut from the midpoint of the track where the process is steady-state. The single-track cross-sections are cold-mounted in epoxy, polished using increasingly finer grit size, and etched in hydrochloric and nitric acid to differentiate between the cladded region and the substrate region. Micrographs of the bead cross-sections are captured on a Leica DVM6 and the geometric dimensions of each cross-section are measured in Leica's LAS X software (**Figure 12**).

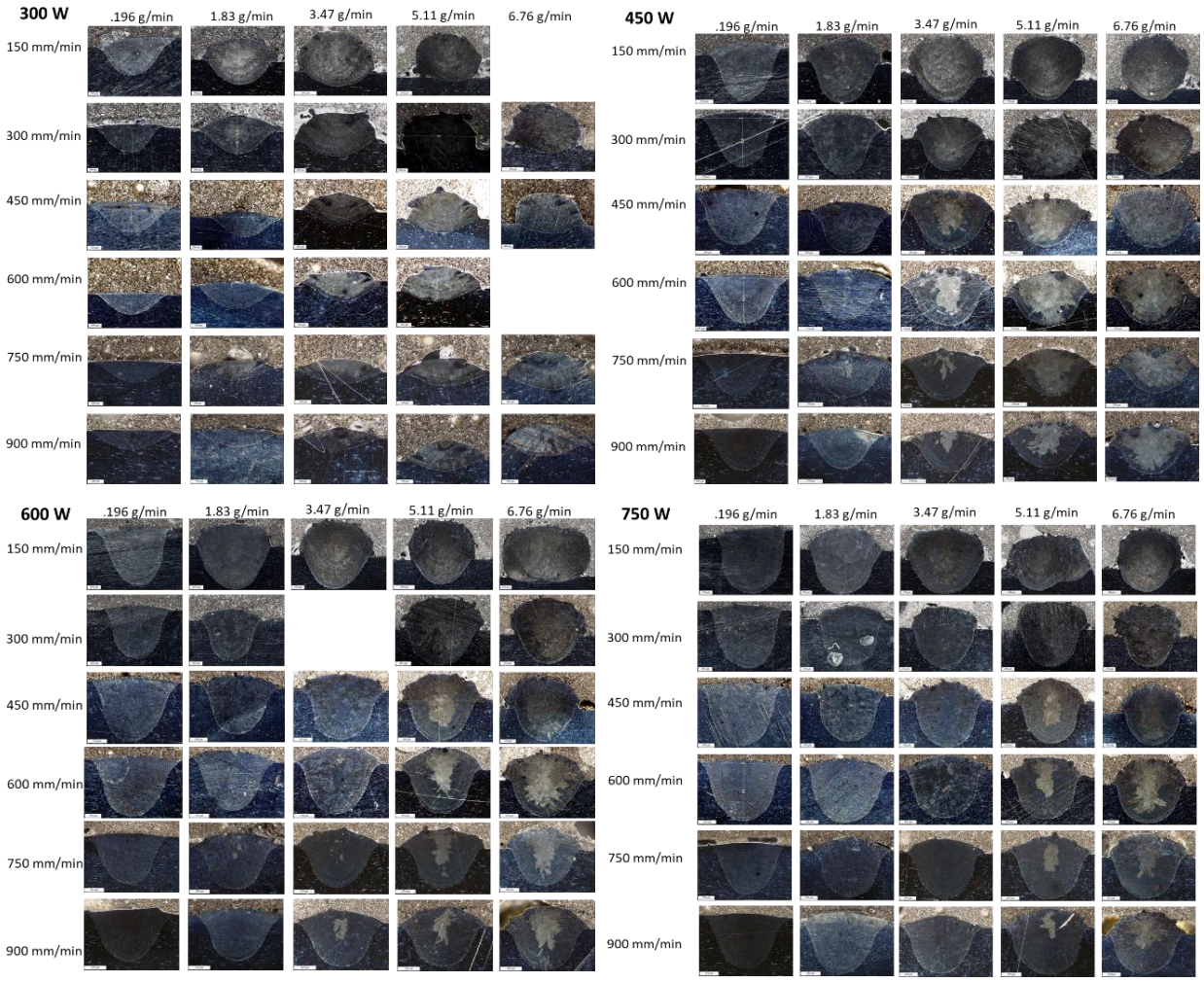

Figure 12: *Optical Micrographs of track cross-sections for full-factorial build parameter experiment*

4.2.4 Results

4.2.4.1 Correlation Matrix

A correlation matrix is constructed (**Table 7**) to identify the extent to which the different inputs and input interactions have correlative effects on bead geometry. Additionally, the correlation matrix can be used to identify linear correlations between the different response variables, such as the relation between bead aspect ratio and dilution. When the engineer is required to tune the DED-processing parameters, it is beneficial to know the extent to which adjusting one output variable will affect other outputs. In the correlation matrix, the independent and dependent variables are

displayed in both the first row and first column. The Pearson correlation coefficient value in each cell of the table shows the corresponding strength and direction of the linear correlation between the two continuous variables. The correlation coefficients range from -1, indicating a strong negative correlation, to 1, which indicates a strong positive correlation. The larger the absolute value of the coefficient, the stronger the linear relationship between the variables, while a magnitude close to 0 indicates little to no linear relationship.

Table 7: *Correlation matrix of single track geometry and build parameters*

	P	U	*Pf*	*P*U	*P*Pf*	U**Pf*	*w*	*h*	*D*	*AR*
P	1									
U	0.003	1								
Pf	0.016	-0.004	1							
P*U	0.527	0.811	0.007	1						
P*Pf	0.408	0.000	0.877	0.214	1					
U*Pf	0.016	0.537	0.755	0.444	0.665	1				
w	0.758	-0.501	0.140	-0.030	0.415	-0.223	1			
h	0.205	-0.581	0.617	-0.369	0.634	0.026	0.673	1		
D	0.327	0.361	-0.780	0.455	-0.502	-0.333	-0.078	-0.716	1	
AR	-0.149	0.290	-0.678	0.121	-0.599	-0.437	-0.300	-0.530	0.637	1

When interpreting the results from a correlation matrix, there are several important considerations to note. The Pearson correlation coefficient is sensitive to extreme data values, so care should be taken in collecting the data and extreme outliers should be discarded if appropriate. A low Pearson correlation coefficient does not necessarily indicate that no relationship exists between the two variables, as the relationship may be nonlinear. The correlation term alone does not convey its statistical significance. Rather, the statistical significance for each correlation term may be determined by calculating its corresponding p-values. In cases where the p-values fall under the confidence level, the null hypothesis can be rejected (the correlation coefficient is significantly different from 0). A 95% confidence interval is chosen, where p-values less than 0.05 show

significance of the result. The correlation coefficients between P and AR, Pf and w, and w and D have p-values of 0.106, 0.128, and 0.396 respectively, and are not considered statistically significant. All other correlation coefficients pass the significance test.

P demonstrates a high positive linear relationship with w and weak correlation with the other geometric properties considered. The correlation between P and w makes intuitive sense when considering the process interactions – increased laser power results in a larger melt pool, which, in turn, increases the powder catchment area. This calculation confirms the findings of Lin, who postulates that powder catchment is directly related to the size of the molten substrate surface and molten powder particles [22]. The width of the bead may be a good indicator of the level of catchment efficiency. For applications where the material is costly, powder utilization becomes a priority and maximizing the track width is increasingly desirable.

U, the scanning speed, shows moderately strong negative correlations with track width, w, and height, h, while possessing weak positive correlation to dilution, D, and aspect ratio, AR. As the scanning speed increases, there is less material deposited per unit length of track – defined as the linear mass density – leading to a decrease in overall bead size. Furthermore, a decrease in laser-substrate interaction time results in less energy delivered per unit length due to the time dependency seen in Eq. 3. Less interaction time leads to less penetration into the substrate. The notably less material build up above the substrate, due to the lower linear mass density, results in a slight increase in D and AR.

The powder mass flow, Pf, shows a strong linear correlation to a decrease in D and AR, and a moderate positive correlation to h. The increased linear mass density increases the track height more so than track width and the penetration into the substrate does not increase due to no change in the laser substrate interaction. The interaction terms exhibit a range of correlation coefficients ranging from almost 0 to moderately strong. Supplying more powder mass per unit length of track tends to

generate beads with larger cross-sections, with less percentage of the bead penetrating the substrate, a smaller aspect ratio, and larger clad angle. The linear energy density is also directly proportional to bead size, but, increasing, the energy density also corresponds to an increase in the penetration into the substrate.

Using the approach of Cheikh et al., it is possible to achieve higher correlation values using combined parameters [82]. However, the purpose of this preliminary experiment study is to identify the individual process parameters to use and to provide some intuitive understanding of how the machine, the VC-500AM, and the material system, 316L SS, interact to generate cladded tracks. Utilizing simplified models and models based on parameters that can be directly adjusted through the machine control are more useful for the operator of the machine in order to tune the process based on the observed bead geometry. The use of combined parameters, while yielding models with better fit, make it more challenging for a user to identify which parameter to adjust in order to achieve the desired results. Thus, only single parameters and their interaction terms are considered in this work.

4.2.4.2 Multiple Linear Regression and ANOVA

Multiple regression fitting is a mathematical tool commonly used to model multi-input, multi-response behavior of systems. Multiple regression modelling is used here to develop an empirical model that considers a range of statistically significant continuously variable inputs and their interaction terms, and to quantify their effect on selected output responses.

Determining the degree of polynomial to use requires balancing the trade-offs between underfitting the data and increasing the complexity of the model, since either extreme may render the model impractical for actual implementation. Most often, for practical engineering purposes, first and second-degree functions are selected as the general form. Cheikh et al. show that first order models may be successfully used to map input and output variables that fall within the middle range

of the processing window [82]. However, Farahmoud and Onwubolu counter that approach, arguing that a second-order polynomial model is the preferable choice for the case of single-track laser cladding with several significant interactions among main input variables, the general form of which is shown in Eq. 31 [83] [84]:

$$Y = \beta_0 + \sum_{i=1}^{k} \beta_i X_i + \sum_{i=1}^{k} \sum_{j=1}^{k} \beta_{ij} X_i X_j + \sum_{i=1}^{k} \beta_{ii} X_i^2 + e_r \quad (31)$$

k is the number of main factors (i.e. independent variables), X_i (i=1, 2, 3) are the controlling variables, β_0 is a constant coefficient, β_i , β_{ij} , β_{ii} are the linear, interaction, and quadratic coefficients, respectively, e_r represents the error term, and Y is the yield or the response variable. In the geometric analysis undertaken in this study, Y is used to represent the clad width, height, aspect ratio, and dilution percentage. However, this analysis can be extrapolated to be used to predict other clad properties such as hardness, porosity, or phase composition. Substituting in the chosen independent variables, Eq. 32 becomes:

$$Y = \beta_0 + \beta_1 * P + \beta_2 * U + \beta_3 * Pf + \beta_{12} * P * U + \beta_{13} * P * Pf + \beta_{23} * U * Pf + \beta_{11} * P^2 + \beta_{22} * U^2 + \beta_{33} * Pf^2 + e_r \quad (32)$$

ANOVA is often used to test the significance of input terms on the output response for multiple factor, multi-input scenarios by comparing the means between the different groups of interest. F and p values are both used to indicate the statistical significance of a particular input variable in the regression model. The coefficient of determination, or R^2 value, is a statistical measure of the fit between the actual, measured data and the regression function. The following ANOVA tables are presented for the single bead width, height, aspect ratio, and dilution second-order equations.

Based on p-value analysis for the clad width regression (**Table 8** and **Eq. 33)**, all first order main effects are determined to be statistically significant, except for the interaction between P and Pf, and the second order Pf term, which both fall outside the confidence interval. There are no statistically significant differences between group means P*Pf and Pf*Pf as determined by the multi-way

ANOVA. Due to the lack of data showing that changes in those independent variables are associated with the changes in the response at the population level, it may be prudent to remove those terms from inclusion in the final model. . The various R^2 values are consistent and close to 1, which indicates a good fit.

$$Clad\ width\ (w) = -8.51 * 10^{-2} + 4.28 * 10^{-3}P - 1.39 * 10^{-3}U + 4.38 * 10^{-3}Pf - 6.73 * 10^{-7}P * U - 8.27 * 10^{-7}P * Pf - 6.62 * 10^{-6}U * Pf - 2.23 * 10^{-6}P * P + 1.35 * 10^{-6}U * U + 8.00 * 10^{-6}Pf * Pf \quad (33)$$

***Table 8**: ANOVA clad width (w)*

Source	DF	Adj SS	Adj MS	F-Value	P-Value
Regression	9	13.0044	1.44494	226.23	0.000
P	1	0.8955	0.89547	140.20	0.000
U	1	0.4158	0.41582	65.10	0.000
Pf	1	0.0822	0.08219	12.87	0.001
P*U	1	0.1003	0.10031	15.71	0.000
P*Pf	1	0.0023	0.00232	0.36	0.548
U*Pf	1	0.3585	0.35847	56.12	0.000
P*P	1	0.2995	0.29953	46.90	0.000
U*U	1	0.6767	0.67666	105.94	0.000
Pf*Pf	1	0.0057	0.00574	0.90	0.345
Error	109	0.6962	0.00639		
Total	118	13.7006			

S	R-sq	R-sq(adj)	R-sq(pred)
0.0799190	94.92%	94.50%	93.54%

$$Clad\ height\ (h) = 3.42 * 10^{-2} + 1.02 * 10^{-3}P - 1.21 * 10^{-3}U + 8.23 * 10^{-3}Pf - 1.34 * 10^{-7}P * U + 3.99 * 10^{-6}P * Pf - 1.11 * 10^{-5}U * Pf - 7.87 * 10^{-7}P * P + 1.16 * 10^{-6}U * U + 4.58 * 10^{-6}Pf * Pf \quad (34)$$

***Table 9:** ANOVA clad height (h)*

Source	DF	Adj SS	Adj MS	F-Value	P-Value
Regression	9	8.06999	0.89667	124.85	0.000
P	1	0.05038	0.05038	7.01	0.009
U	1	0.31362	0.31362	43.67	0.000
Pf	1	0.29011	0.29011	40.39	0.000
P*U	1	0.00395	0.00395	0.55	0.460
P*Pf	1	0.05415	0.05415	7.54	0.007
U*Pf	1	1.00773	1.00773	140.31	0.000
P*P	1	0.03729	0.03729	5.19	0.025
U*U	1	0.50285	0.50285	70.01	0.000
Pf*Pf	1	0.00188	0.00188	0.26	0.610
Error	109	0.78285	0.00718		
Total	118	8.85285			

S	R-sq	R-sq(adj)	R-sq(pred)
0.0847476	91.16%	90.43%	89.25%

For the AR ANOVA presented in **Table 10**, the only term that does not pass the statistical significance test is the U*U second-order term. However, variance in the AR can be explained by the other independent variable groupings chosen. While the all of the R^2 values are lower for the AR model, relying solely on the R^2 value as an assessment of fit may be misleading. As a result, the model deserves further goodness-of-fit analysis to determine the cause of the lower coefficients of determination. Of note is the observation that both the width and height regression lines fit the data with a 90% or greater R^2 fit, and that AR is essentially the ratio of those two parameters. The increase in lack-of-fit for the AR model could be due to compounding error in trying to fit the product of the clad width and the inverse of the clad height, which also leads to more variance in the data. For other applications, it may be possible to investigate a different form of the regression or utilize different combinations of parameters that yield a closer fit, or to develop individual models for different regions of the process window. However, the R^2 values of 73-79% indicate that the independent variables modelled in Eq. 35 and **Table 10** can predict the aspect ratio across the range of process variables investigated somewhat well.

$$Apect\ Ratio\ (AR) = 27.6 - 5.47 * 10^{-2}P + 3.66 * 10^{-2}U - 6.44 * 10^{-1}Pf - 3.16 * 10^{-5}P * U + 2.99 * 10^{-4}P * Pf - 2.61 * 10^{-4}U * Pf + 4.60 * 10^{-5}P * P + 4.07 * 10^{-6}U * U + 4.20 * 10^{-3}Pf * Pf \quad (35)$$

Table 10: *ANOVA clad aspect ratio (AR)*

Source	DF	Adj SS	Adj MS	F-Value	P-Value
Regression	9	8904.5	989.39	44.79	0.000
P	1	145.8	145.80	6.60	0.012
U	1	289.0	288.99	13.08	0.000
Pf	1	1776.4	1776.40	80.42	0.000
P*U	1	220.3	220.32	9.97	0.002
P*Pf	1	303.1	303.07	13.72	0.000
U*Pf	1	554.9	554.89	25.12	0.000
P*P	1	127.1	127.11	5.75	0.018
U*U	1	6.2	6.20	0.28	0.597
Pf*Pf	1	1583.0	1583.04	71.66	0.000
Error	109	2407.8	22.09		
Total	118	11312.3			

S	R-sq	R-sq(adj)	R-sq(pred)
4.69995	78.72%	76.96%	73.17%

$$Dilution\ \%\ (D) = 0.363 + 1.43 * 10^{-3}P + 6.36 * 10^{-4}U - 1.22 * 10^{-2}Pf - 1.90 * 10^{-7}P * U + 6.44 * 10^{-6}P * Pf + 4.07 * 10^{-6}U * Pf - 1.13 * 10^{-6}P * P - 4.05 * 10^{-7}U * U + 1.49 * 10^{-5}Pf * Pf \quad (36)$$

Table 11: *ANOVA Clad dilution % (D)*

Source	DF	Adj SS	Adj MS	F-Value	P-Value
Regression	9	5.20157	0.577952	64.94	0.000
P	1	0.10031	0.100312	11.27	0.001
Ts	1	0.08723	0.087232	9.80	0.002
Pf	1	0.63668	0.636684	71.54	0.000
P*U	1	0.00796	0.007961	0.89	0.346
P*Pf	1	0.14064	0.140636	15.80	0.000
U*Pf	1	0.13543	0.135435	15.22	0.000
P*P	1	0.07688	0.076879	8.64	0.004
U*U	1	0.06121	0.061206	6.88	0.010
Pf*Pf	1	0.01994	0.019940	2.24	0.137
Error	109	0.97013	0.008900		
Total	118	6.17170			

S	R-sq	R-sq(adj)	R-sq(pred)
0.0943412	84.28%	82.98%	81.62%

The models and ANOVA tables demonstrate the tightly coupled nature of the various process parameters. For example, decreasing the scanning speed does not just lower its U term, but it also decreases the U*U, P*U, and U*Pf terms, as well. It should be noted that the single order terms for P, U, and Pf, as well as the parameters U*Pf and P*P, are significant for each of the geometric characteristics analyzed. This result may indicate the usefulness of the U*Pf interaction and P*P second-order term in developing further models.

After developing the different regression models, it is necessary to perform further validation efforts them before utilizing them in the field. While ANOVA provides a good indication of the statistical significance of each term used within the model, normal probability plot validation techniques are a graphical method used to visualize whether the data substantively departs from a normal distribution about the regression line. The normal probability plot is a special case of the probability plot for testing normal distribution, formed by plotting the ordered response values against the normal order statistic medians. The plot should form an approximate straight line and departures from the straight line indicate the departures from normality in the form of outliers, skewness, kurtosis, and mixtures. A secondary plot is also used, for further visual clarification, where the predicted responses are also plotted against the actual measured responses and the color map

corresponds to the absolute value of the residual. The colormap is useful in providing a visual indication of the deviation between actual and predicted responses.

The cladded bead width normal probability plot presented in **Figure 12** depicts a reasonably linear pattern in the center of the data, however the tails show departures from the fitted line. The appearance of the lower tail below and the upper tail above the fitted line indicate that the tails are longer than normal distribution. This normal probability plot looks similar to the double-exponential distribution, which is symmetric about the mean but declines more rapidly and has longer tails as compared to the normal distribution. In **Figure 13**, the model shows a strong match between the predicted responses and the experimentally measured clad widths. The upper extremes of the data set do show some increased deviation between the expected and actual results. The presence of outliers could represent volatility in the process in that region of the process window, or it could represent more difficulty in obtaining good quality measurements during data collection.

Figure 14 presents the normal probability plot for the clad height data set. The residuals follow a similar distribution as the clad with measurements. However, it does appear to follow the fitted line for a shorter span that the width data, indicating a slightly less normal distribution. The tails are long on both extremes; however, it looks to be longer on the right-hand side, above the fitted line. The actual and predicted response plot, **Figure 15**, generally follows a slope of 1 throughout the whole data set. However, after a height of 0.5mm, the data begins to diverge more and more from the predicted responses. While a few data points lie on the fitted line, as the track height increases it tends to be over predicted.

The AR normal probability plot, **Figure 16**, indicates a decrease in deviation from the normal distribution. The leftmost residuals seem to follow the fitted line; however, the line is drawn above them. Moving to the right, the data points curve upwards, a sign of right-skewness. Confirmed in **Figure 17**, above an aspect ratio of about 7.5, almost all of the actual results are under-predicted

using the current model. It may be necessary to consider a different distribution to represent the data, such as Weibull or lognormal. However, it should be noted that, under a few circumstances, it is desirable to choose an AR above 7.5. Thus, further work in process parameter development could focus data capture in the lower region of the graph.

The actual dilution values seem to match the predicted values relatively well along the entire range of measured values (**Figure 19**). However, the residual distribution presented in **Figure 18** is not normal about the fitted line. It is clear that there is more variance in the measured data than would be expected in a normal distribution. The measured data also reveals that, with the chosen process parameter range investigated in this full-factorial study, few combinations of parameters achieve a dilution of less than 40%. As powder flow possesses the strongest linear correlation with dilution percentage, it would be beneficial to focus investigative efforts on the upper ranges of powder mass flow capabilities, which correlate to a decrease in dilution, in future process parameter development.

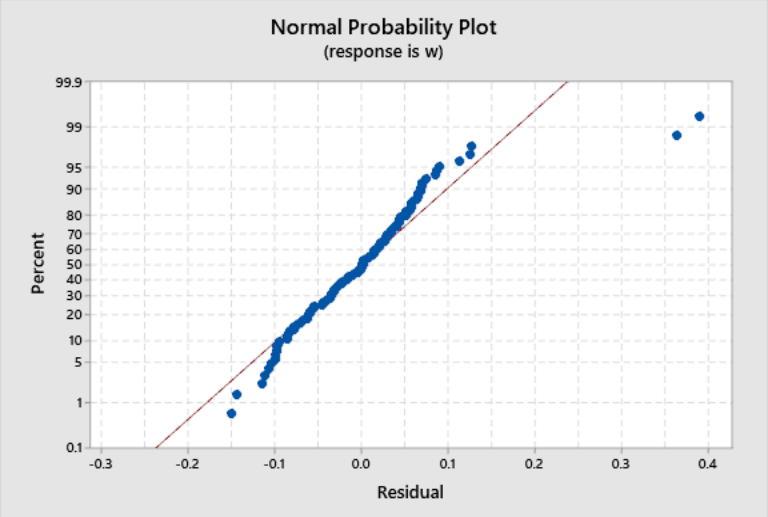

Figure 13: *Clad width normal probability plot*

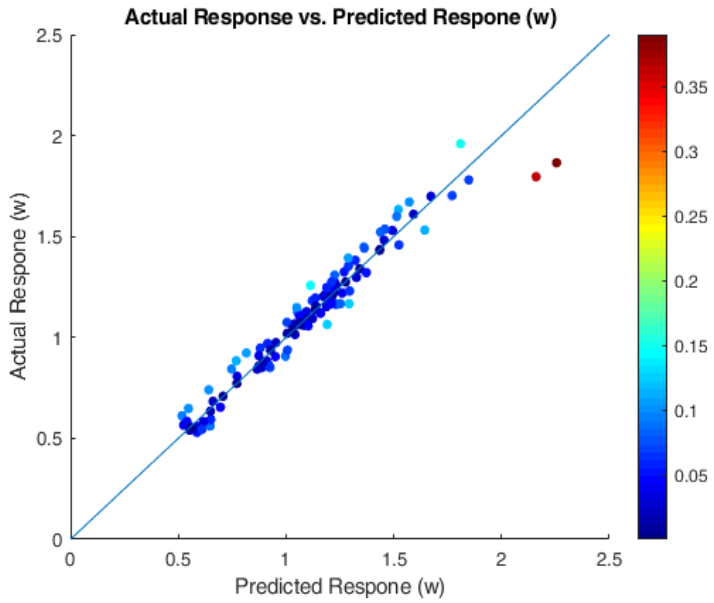

Figure 14: *Clad width actual response versus predicted response*

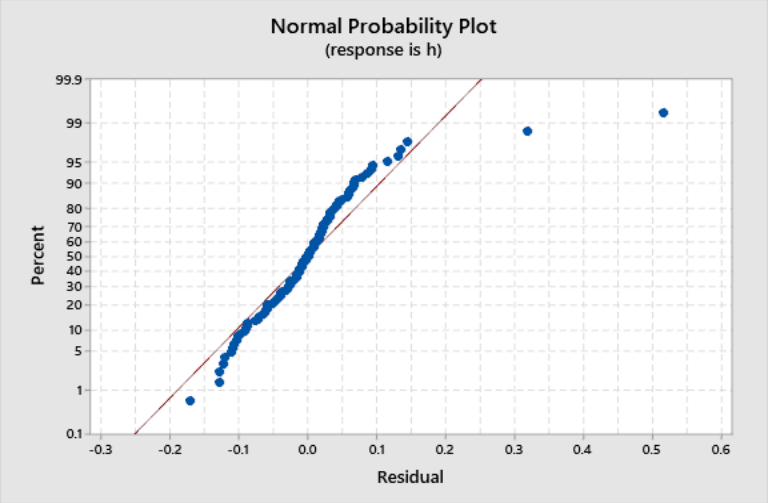

Figure 15*: Clad height normal probability plot*

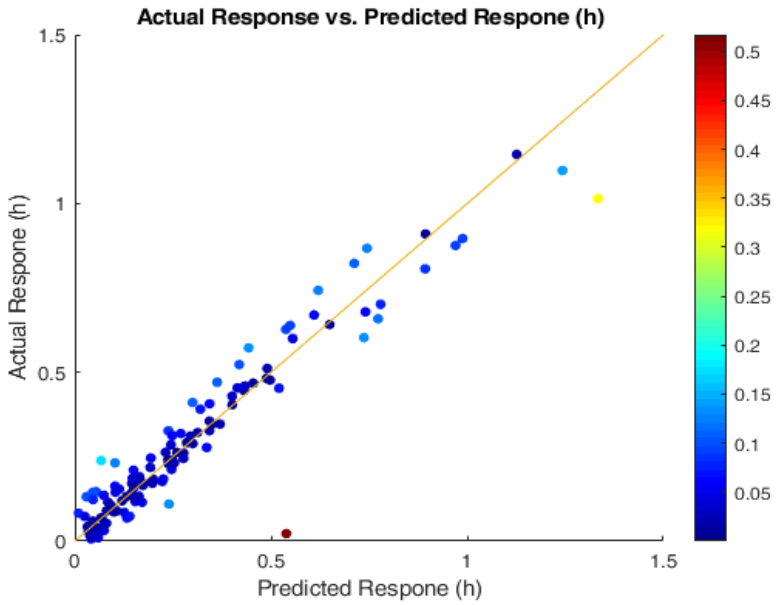

Figure 16: *Clad height actual response versus predicted response*

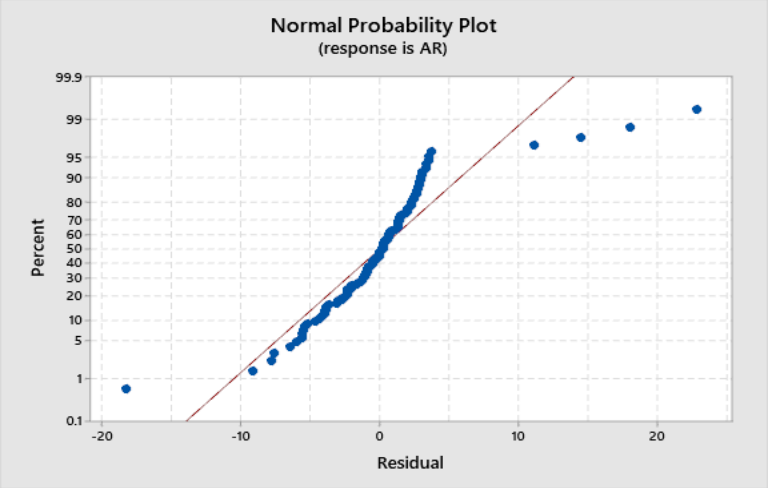

Figure 17: *Clad aspect ratio normal probability plot*

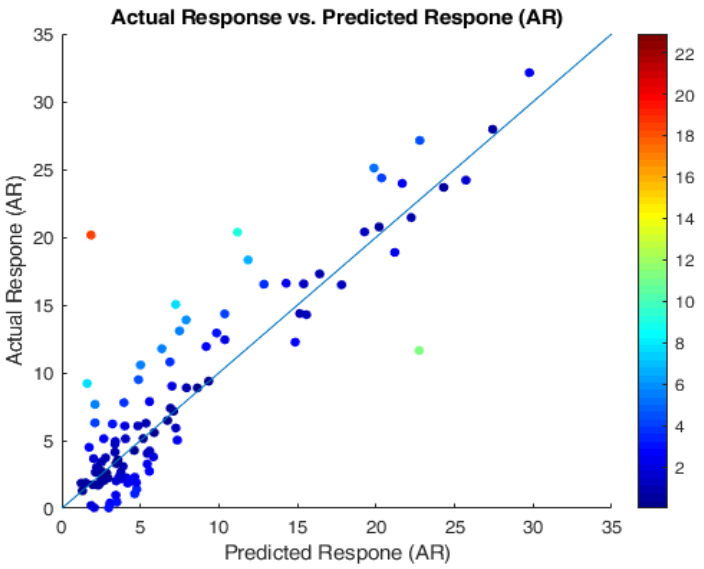

Figure 18: *Clad aspect ratio actual response versus predicted response*

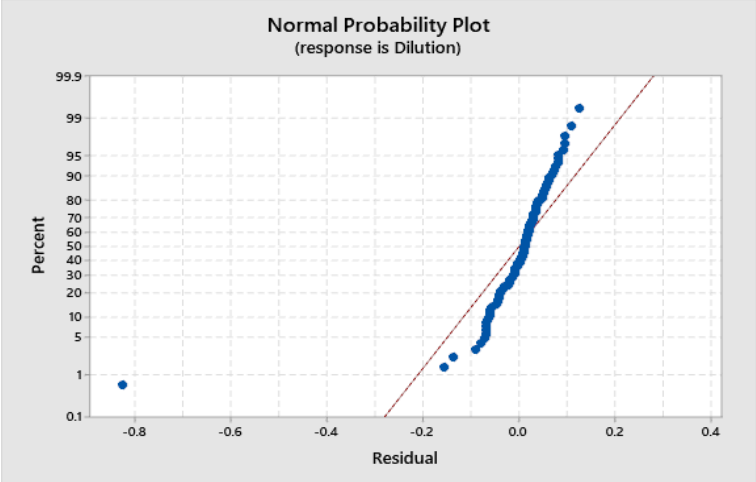

Figure 19: *Clad dilution normal probability plot*

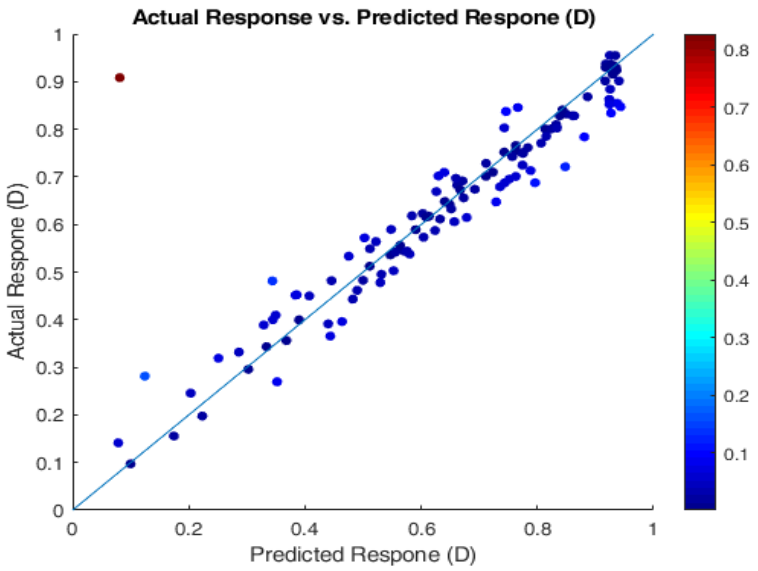

Figure 20: *Clad dilution actual response versus predicted response*

4.2.3.3 Multi-objective Optimization

Once the relationship between process parameters and clad bead shape is identified, the goal becomes solving for the process parameters that correspond to the desired geometric attributes. Based on values found in the literature, an AR of 2.38 is desirable, resulting in a clad angle of approximately 80°, which provides a good balance between height and spreading on the substrate surface [70]. A dilution percentage of 15% for 316L SS is selected as the desired outcome based on the work of Alvarez et al., and a track width of 1.0 mm is chosen in order to try to achieve a track towards the median of the measured results [25].

Process parameter selection can be performed in two ways. One method is through process of elimination where geometric characteristics are sequentially selected for based on their order of priority. Parameter combinations that do not yield the desired geometric traits are successively ruled out. One example of this method is to select for the desired dilution first, as it serves as an indicator of the extent of metallurgical bonding. Using the current data set, by selecting a range of 10-30%, the number of parameter combinations that meet that requirement is reduced from 120 to 8. Further selecting for an AR of 2.0-4.0, since this characteristic governs the overall shape of the bead and limits

inter-track void formation, reduces the possible combinations from 8 to 3. Then, other criteria can be used to select the parameter set to use, such as volumetric build rate (clad area above substrate multiplied by scanning speed), maximizing track width to increase powder utilization, or selecting a desired hardness. However, the limitations in this method are that only parameters that have been tested are used.

Another method is to develop a cost function and use a nonlinear multi-objective optimization solver to identify the most optimal combination of process parameters to meet the desired outputs. In optimization, a cost function maps the error between predicted vales and expected values. The goal is to identify the process parameters that minimize the cost. Sequential Quadratic Programming (SPQ) uses an iterative approach for solving constrained nonlinear optimization problems that meet the requirement that the objective function be twice continuously differentiable. SPQ solves a sequence of quadratic subproblems to identify a point where the gradient of the objective goes to zero. The Python library SciPy contains a SPQ solver called Sequential Least SQuares Programming (SLSQP), which is implemented here in order to solve the objective function and identify the appropriate input parameters. The corresponding cost function for the current problem is shown in Eq. 37:

$$J = w_1(w - w_o)^2 + w_2(AR - AR_o)^2 + w_3(D - D_o)^2 \quad (37)$$

where w_1, w_2, and w_3 are the corresponding relative weights of the desired outcomes. The weights represent the value trade-offs, defining how much the cost must be reduced in the achievement of one objective to compensate for an increase due to lesser achievement on a different objective [86]. They are determined by experimenting with different values and comparing the predicted output of the returned optimized parameter, taking care to account for the different scales of the various terms and the priority for each output. The desired outcomes for clad width, aspect ratio, and dilution percentage are indicated by w_o, AR_o, and D_o, respectively. The height term is not explicitly expressed

in the cost function because it is solved for through determining the corresponding w and AR values, thus including that term would serve to over-constrain the problem.

Once the initial guesses and parameter constraints are provided to the linear solver, the algorithm iteratively searches for the global minima of the cost function. In order to determine the initial guess to provide the solver, an iterative search process is performed whereby many different initial conditions are provided to the solver, spanning the process window. The initial guess that results in the least cost for the particular set of weights is identified as the optimum choice. In the case of the multi-criteria optimization of clad geometry, the solution is dependent on both the relative weights and the initial guess.

The predicted bead shape displayed in ***Table 12*** demonstrates that the models and optimization techniques show promise in predicting a bead shape that is close to or meets the desired objectives. However, the regression model used may not sufficiently account for the inconsistencies and variance within the process. This may be improved through the collection of additional data for analysis after refining the parameter search window or the use of combined parameters. Final tuning of process parameters can be made on the machine to account for deviations between the actual measured geometry.

Table 12: *Multi-Criteria Optimized Process Parameters*

Objectives: w = 1.0 mm, AR = 2.38, D = 15.0%		
	Initial Guess	Optimized Parameters
P (W)	300	305
Ts (mm/min)	300	301
Pf (Duty Cycle %)	90	66
Predicted: w = .99 mm, AR = 2.17, D = 26.0%		

As one might expect, the solution to the objective function changes substantially as a function of the chosen relative weights. While the experiments performed in this study represents an initial effort to perform multi-criteria optimization of the various process parameters, additional work

should be conducted to improve the current heuristic method for determining the value trade-offs between the different geometric traits. To reduce the solution-space, other objectives may be used to further constrain the solution and reduce the number of local minima, such as identifying the solution that maximizes microhardness or volumetric build-rate.

Through iterative testing of various initial guesses and tuning of the weighting factors, it is noted that a positive correlation exists between AR and D in both the outputs of the optimization function and the correlation matrix. Thus, the model is limited in its ability to simultaneously solve for a decreased dilution and increased aspect ratio. While the model presented here uses parameters that are direct inputs to the process and are interpretable, using combined parameters, for the purposes of multi-objective optimization, may present more capability in balancing the two opposing objectives and yield more desirable results.

4.3 Full build

4.3.1 Specimen Design

The tensile specimens are designed in accordance with the ASTM E8 subsize tensile specimen dimensions. The specimen cross-sections measure 3 mm x 6 mm with a 32 mm gage length. The specimen size is chosen to balance build time while minimizing errors that may arise from working with small components. In order to maximize tensile test usefulness, they should behave as a representative volume of the investigated material. However, tensile behavior is a convolution of intrinsic material properties and superimposed contributions from flaws such as internal defects, cracks, corrosion, embrittlement, and residual stress, among others [87]. Due to this convolution, there is a size effect on mechanical properties. A larger specimen may experience an increase in the number of defects present within the specimen, however the size of each defect becomes smaller relative to the specimen volume. For example, a lattice strut with a 250 μm thickness can contain a 25 μm pore that reduces the effective area by 10%. There is also a statistical size effect of structures

that follow the weakest-link model, where the macro-fracture initiation from one material element causes the entire structure to fail – analogous to the weakest link in a chain. The stochastic material strength of the material depends on the survival of all of its links. In addition to being easier and less costly to build, the fewer number of layers deposited should increase the strength of the material as the number of material elements decreases.

The tensile specimen gage size is also selected to be large enough to reduce errors in mechanical behavior due to the gage length not being split perfectly in the middle between the two materials. Using a 32 mm gage length with a 3 mm x 6 mm cross-section leads to a change in the volumetric percentage for each region of 3.1% due to a 1 mm deviation from the nominal substrate-additive adhesion zone position. This error is doubled to a 6.2% change in volume with a 16 mm gage length specimen.

Three batches of ASTM E8 subsize tensile specimens are produced to investigate the build orientations of 0°, 15°, and 30°. The specimens are manufactured so that half of the gage section is composed of wrought flat bar stock and the other half is composed of deposited 316L SS. The three sperate builds are designed to yield 5 test specimens each. The motivation for designing the specimens in this way is to simulate the behavior of hybrid manufactured components. Unlike L-PBF produced parts, the advantage of DED and hybrid manufacturing is to integrate various manufacturing processes and materials together to produce fully functional parts, and few experiments in the literature investigate the behavior of wrought-DED tensile properties of similar metals.

All depositions are performed in the XY-plane with the nozzle normal to the deposited surface. While the deposition of the specimens occur all in the same build orientation, the components are sectioned from the bulk material using wire EDM in such a way that the layers are oriented at different angles with respect to the tensile specimen axis. This particular specimen design necessitated

performing three separate builds to yield each orientation of specimens. Thus, each build had a slightly different geometry as depicted in **Figure 21**. The geometries of the completed samples are displayed in **Figure 22**.

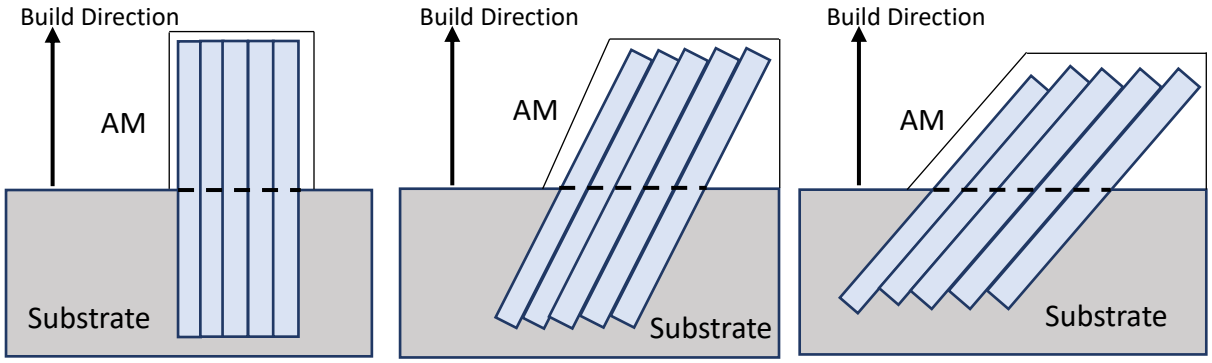

Figure 21: *Bulk material geometry for additive material a) 0° b) 15° c) 30°*

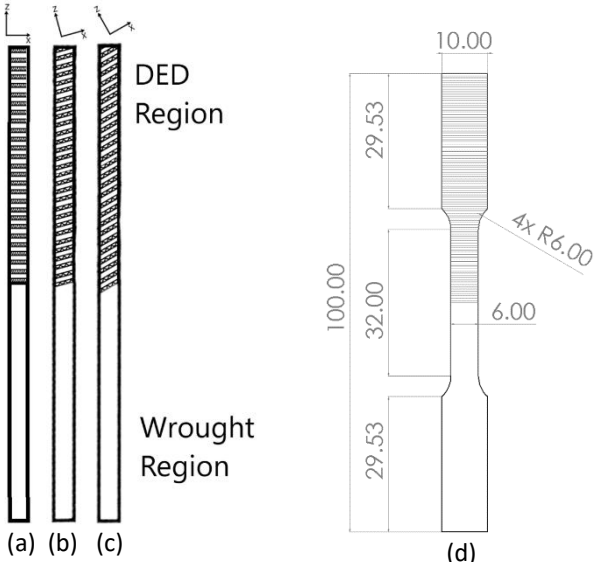

Figure 22: *ASTM E8 Tensile samples showing build geometry and layer orientation: a) 0° orientation; b) 15° orientation; c) 30° orientation; d) specimen dimensions in mm—3 mm thickness not shown*

4.3.2 Toolpath Selection

The properties of the deposited material are influenced by the deposition path trajectory, which makes path planning an essential part of the process design. It is crucial to develop an

appropriate path planning strategy to reduce harmful effects the toolpath may have had on mechanical and metallurgical characteristics of the as-built part. The deposition process, part geometry, and end functionality are all key influencers in determining an appropriate strategy. It has been reported that reducing the number of layers, by increasing the layer thickness (slicing interval), may improve mechanical properties. Reducing the number of deposited layers may also decrease build time, with the consequence of increasing the surface finishing requirements, as the intervals between layers coarsens and the "stair-stepping" effect becomes more significant. Another contributing factor to the quality of DED parts is the accumulation of residual thermal stresses due to the non-uniform heating of the workpiece. There are some general guidelines when designing a toolpath for DED regarding the accumulation of thermal stress and considerations taken to minimize discontinuities and void accumulation within the component [41]:

- **Thermal stresses** accumulate through unbalanced heating of the part. The deposition path should be symmetrical to reduce the accumulation of residual stresses.
- **Discontinuous tracks** require the laser shutter to be switched on and off repeatedly, possibly leading to premature wear or failure of the laser unit. Discontinuous tracks also increase the possibility for voids or non-uniform deposition to occur at the beginning and ending point of each track as a result of additional non-steady-state deposition.
- The chosen strategy should be **robust** enough to minimize the effects of depositing on complex geometries, such as acute corners, thin features, and surfaces requiring multi-axis motion**.**
- **Non-planar** deposition strategy may be required if a planar strategy leads to material being redeposited in certain points, leading to over-building.
- **Gaps** between adjacent tracks, such as when transitioning from a profile path to an infill pattern, may lead to low quality parts and should be avoided. CAM software often

includes a parameter that can be adjusted to control the degree of overlap between the outer contour path and the infill.

- **Anisotropy** of layer-based manufacturing methods may require the use of a slicing strategy that accounts for the external loads on the part.

The requirements considered above significantly constrain the problem of deposition path planning, and, in many ways, reflect similar decisions when developing machining strategies. The two main deposition strategies used for 2-D cross section path planning are zig-zag paths and contour paths:

- **Zig-zag (or raster) paths** are a sequence of linear paths executed in bidirectional or unidirectional manner within the boundary of the 2-D cross section.
- **Iso-contour (or spiral) paths** are a series of contoured paths incrementally offset from the boundary of the 2-D cross-section. It is also possible to link the series of contoured paths so that they form a spiral, or the laser can be shuttered when traversing from the end of one contour to the beginning of the next.

Zig-zag and spiral strategies (shown in **Figure 23** and **Figure 24**) may be used individually to completely fill the 2-D cross section of a part, or, if the 2-D boundary geometry necessitates it, it may be necessary to use some combination of the two strategies. These basic toolpaths can be further adapted to more complex scenarios, for example, utilizing curved path vectors within in the zig-zag strategy. For large components, some engineers have employed an island scanning strategy, where the 2D-slice is dissected into small squares, or islands, and each square is completed using the chose deposition strategy before moving onto the next section [88].

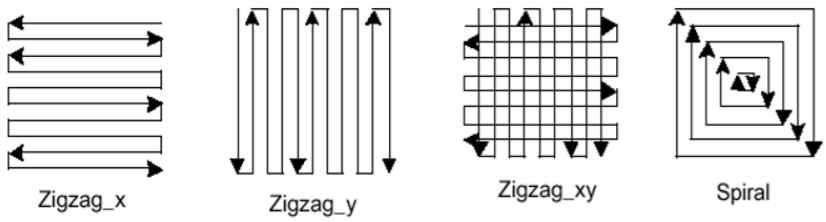

Figure 23: *Different deposition strategies used to produce cubic component layers (Source: Professor J. Choi, Department of Mechanical and Aerospace Engineering and Engineering Mechanics, University of Missouri at Rolla)*

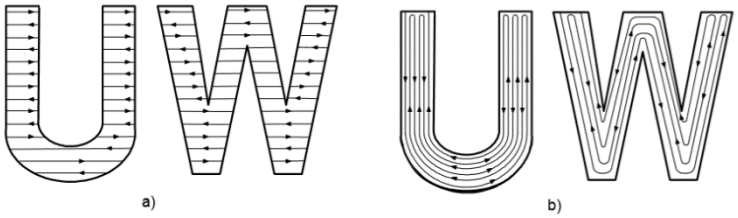

Figure 24: *Deposition strategies for non-cubic geometries: a)zig-zag x strategy b) spiral strategy [41]*

The toolpath strategy selected in this study is a bi-directional raster with 0.75 mm step-over and a 0.5 mm z-height increment. The build direction occurs along the z-axis and the layers are deposited in the XY-plane. A XY-raster path is used, where the toolpath is rotated 90° each layer so that tracks on adjacent layers are oriented perpendicular to each other and the starting point for each layer is rotated around the part clockwise (**Figure 25**). Using this strategy, every fourth layer employs the same start point and zig-zag orientation; rotating the start point ensures symmetric heat distribution throughout the build.

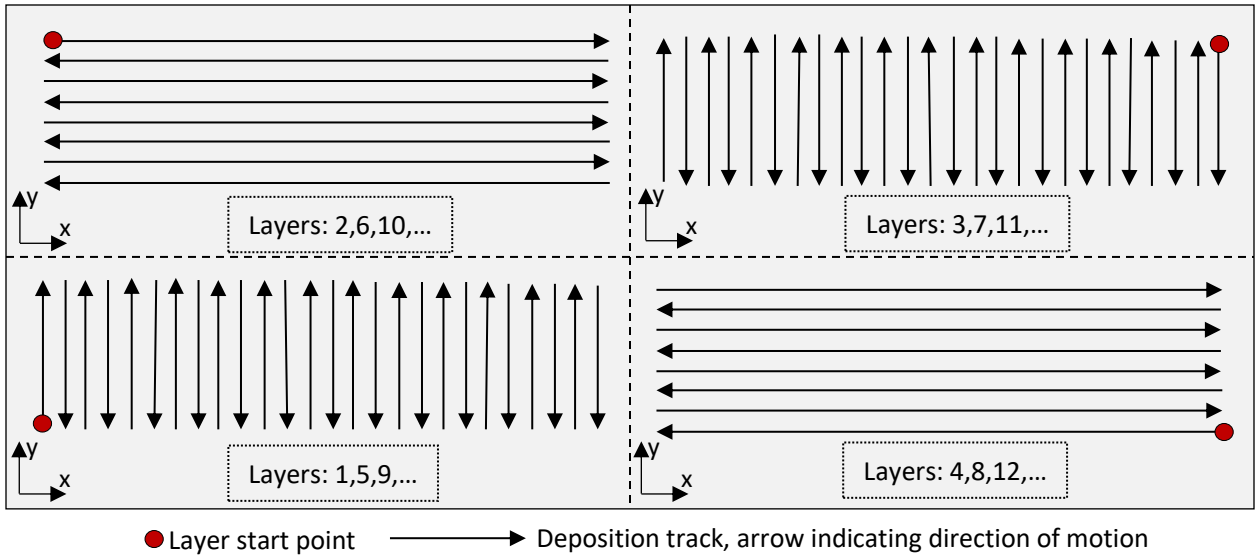

Figure 25: *XY-zigzag with 90° rotation*

Preliminary tests to determine the desirable toolpath strategy begin with the use of a contour path. Contour paths are commonly used in Fused Deposition Modeling (FDM) AM processing for several reasons. One motivation is to generate higher fidelity surfaces, where discontinuities from the infill starts and stops are not exposed. The surface not only looks "cleaner", but also ensures dimensionality. Another motivation for using a contour path is that AM processing possesses the capability of generating components with non-solid infill, and therefore necessitates the creation of a solid outer shell. Generating components with completely solid interior is achievable, but it is time consuming and may require significant material investment. However, if the component application allows for it, sparse infill can be generated to reduce the density of the component. The advantage using this strategy comes in the form of weight savings, reduction in build time, and lower material consumption, but at the cost of reduced component strength. Due to the prevalent use of contour paths combined with zig-zag infills, it is selected as the first deposition strategy to build the bulk material for the tensile specimens.

As demonstrated in **Figure 26**, significant concavity develops on the top surface over the course of the build. The formation of the concave surface may be attributed to a variety of different sources:

- Too much overlap between the infill and contour path, resulting in overbuilding along the edges. Overcorrection and the subsequent lack of overlap, however, results in voids between the tracks.
- As the laser turns around between path vectors, the laser interaction time is longer, and the heat has not had as much time to dissipate, leading to different powder catchment conditions.
- As the concavity evolves, the variation in standoff distance leads to different energy densities between the edge and center, resulting in different powder catchment conditions and contributing to a positive feedback loop, further exacerbating its formation.

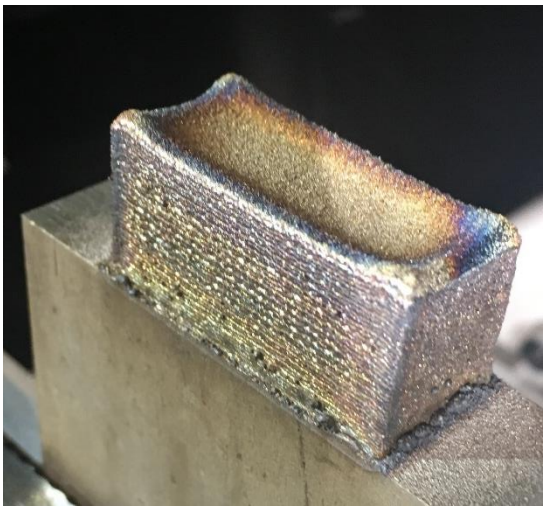

Figure 26: *Results of Contour path with XY-zigzag infill*

The formation of concavity in the top surface introduces a new challenge of how to determine where on the surface the standoff distance should be set. As the depth of the concavity increases, the standoff distance between the deposition head and the deposited surface progressively deviates from

the nominal distance. The increasing and decreasing standoff distance, coupled with constant laser power, causes the power distribution density – the amount of power delivered divided by the area of the defocused laser – to vary. The inverse square relationship is plotted in **Figure 27**, which reflects the configuration of the deposition conducted in this study – a nominal laser power of 300W, a laser diameter of .383 mm at the nozzle exit, and a laser divergence angle of 11°.

Forgoing the use of a contour path prior to executing the infill pattern results in a significantly more stable surface topography with limited overbuilding along the edges as compared to the rest of the surface. Additionally, to maintain a more even process zone temperature throughout the part, dwelling times are incorporated between path vectors to allow some of the heat to dissipate. In this manner, the laser interaction time is somewhat normalized throughout the build.

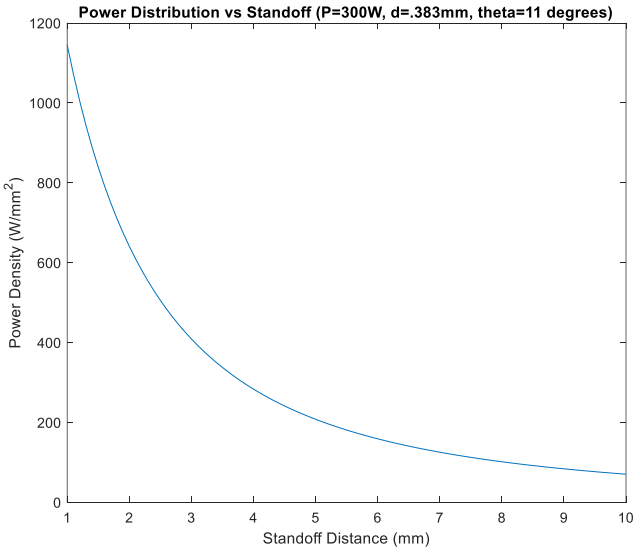

Figure 27: *Inverse square relationship between power density and standoff distance*

4.3.3 Additive Build

Using the specimen design and toolpath strategy outlined above, the three batches of parts are produced, with material deposited at build orientations of 0°, 15°, and 30° on top of wrought 316L

substrate using the nominal build parameters presented in ***Table 13***. The parameters chosen have been selected due to the satisfactory wetting angle, bead aspect ratio, and dilution that they produce.

Table 13: *Nominal Build Parameters*	
Laser Power (W)	305
Nozzle Gas (L/min)	2
Shielding Gas (L/min)	10
Disk Speed (%)	66
Carrier Gas (L/min)	5
Scanning Speed (mm/min)	300

5 individual tensile specimens are then extracted from the block via wire EDM. The specimens are extracted in such a manner so that the effective build orientations with respect to the lengthwise axis of the samples are oriented at 0°, 15°, and 30°. Samples are then lightly polished using 1000 grit sandpaper to remove small surface defects and the recast layer leftover from the EDM process.

4.4 Microstructure Analysis

4.4.1 Metallographic Preparation

In order to reveal the microstructure present within the as-deposited samples cutouts were yielded from the bulk material printed. The samples were first cold mounted in a two-part epoxy resin. After 24 hours of curing, the samples were removed and subject to a series of mechanical polishing steps. Starting with 200 grit abrasive, the samples were wet ground to achieve flat and parallel opposing surfaces. Successively finer silicon carbide grit abrasives were utilized until 4000 grit. Then suspended diamond grit was used beginning with 9 μm and finishing with 0.5 μm. The samples were then placed in a slurry of fine alumina and polished for an hour and a half to produce a scratch-free mirrored surface.

Grain boundaries tend to be more reactive (in that they more readily form chemical bonds) than the grains, because of the lower packing efficiency and increased disorder present in the boundaries as compared to the ordered grain structures. Due to this difference, using special reagents, it is possible to induce rapid corrosion along the grain boundaries so that when the surface

is magnified and subjected to illumination it is possible to see, visually, the structure of the metal. After polishing, a solution of 100 mL water, 100 mL HCl, and 10 mL was swabbed on the surface of the samples at room temperature. The samples were then rinsed under tap water to halt the reactive from over-etching the surface.

The microstructure images were captured on a Leica DVM6 with a 5MP lens using Bright-Field Illumination where the light reflection is perpendicular to the specimen being viewed. The images were processed in Leica's LAS X software. Generally, using this method, the microstructural features such as grain boundaries are dark and the complimentary matrix regions are bright.

4.4.2 OM Results

The two main factors contributing to the mode of solidification is the temperature gradient, G, and the solidification rate, R. Within the melt pool G, R, and ΔT vary significantly, thus a different microstructure develops spatially throughout the melted region. Along the solidification boundary the liquid/solid interface varies from next to zero at the bottom of the bead to a velocity equal to the scanning speed at the top. The largest thermal gradient occurs at the bottom of the melt pool boundary with the substrate and large amounts of heat is transported through conduction into the substrate material resulting in the expectation that columnar dendrites should be observed along the interface with the substrate and then should transition to a highly refined equiaxed grain structure towards the middle and top of the deposited track. Rapid cooling also occurs along the surface of the bead exposed to air due to the forced convective cooling of the Ar gas flow. The center of the bead experiences the slowest solidification rate and the highest peak temperature.

Figure 28 shows the grain formation within one of the deposited tracks of material. The columnar grains can be seen as indicated by the red arrows. They radiate normal from the melt pool boundary indicate the thermal gradient orientation and although they mostly do not align normal to the build direction the major axis of the columnar grains tends towards the build direction. The

majority of the deposited material is dominated by highly refined equiaxed grains. What is commonly seen in 316L SS cladded material is the presence of subgrains, which are part of larger grains but are slightly disoriented for the other lattice structures within the grain. The presence of subgrains complicate Hall-Petch calculations, but it has been shown that the higher the density of subgrains the greater the material yield strength, due to increased subgrain boundaries [89]. However, there is a subgrain boundary strengthening breakdown point at subgrain sizes less than 0.1 μm [89]. However, a circle of area 6049.54 μm was overlaid on the micrograph of the deposited material and it was determined, through thresholding the image and analyzing the number of detected particles using ImageJ that the average grain size was estimated to be 16.26 μm in the equiaxed region – well above the 0.1 μm strengthening lower limit.

It can be seen that the columnar grains rapidly transition to regions dominated by equiaxed grains which nucleated in the center of each bead and serves to introduce random crystallographic orientations into the sample. However, crystallographic orientation information cannot be obtained from these OM images, and further EBSD imaging would be necessary.

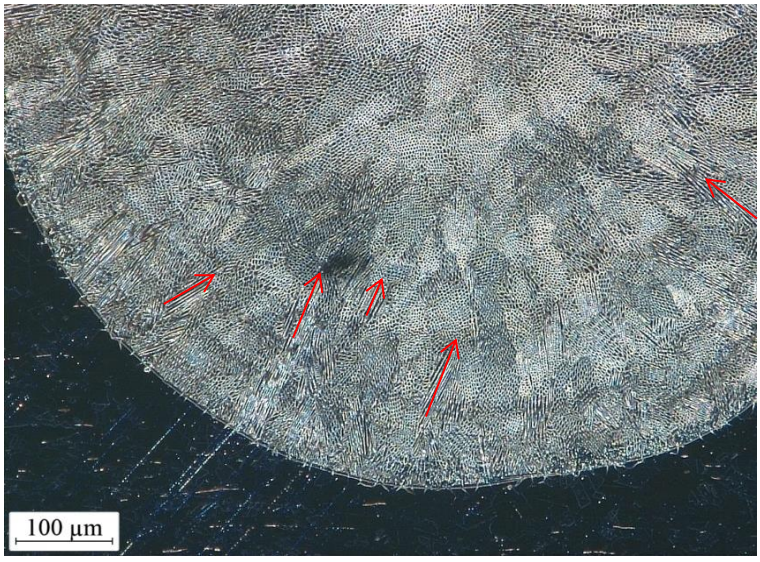

Figure 28: *High-resolution optical micrograph showing 316L SS DED microstructure*

Figure 29: *Multi-track, multi-layer optical micrograph*

In multi-layer depositions, it can be observed that many grains cross melt pool boundaries, which suggests that epitaxial grain growth occurs along the melt pool-substrate interface. Deposited beads inherit crystallographic orientations through epitaxial grain growth from the substrate boundaries. This is largely due to the similarity in composition between the deposited and substrate material. When the compositions differ greatly solidification occurs by nucleation and growth mechanisms. However, if the compositions are largely similar then the dominating solidification is epitaxial growth originating from the liquid/solid boundary.

It can be seen in the micrographs that competitive epitaxial grain growth results in only grains with direction parallel to the maximum temperature gradient experience easy growth and crowd out other grain growth orientations. For FCC and BCC metals the easy growth direction occurs in the <100> and <1010> for HCP metals.

Under higher magnification, regions of low-angle crystallographic boundaries, referred to as subgrains are revealed. EBSD analysis performed on the same materials produced via SLM shows a lack of melt pool boundaries, which confirms that grains in the bottom of the melt pool form through epitaxial growth [90]. However, Kurzynowski et al. revealed that the degree of crystallographic misorientation is highly dependent on laser power and scanning speed.

While columnar grains grow across melt pool boundaries the boundaries are still visible optically. This could be due to elemental segregation that occurs at the melt pool boundaries, or small HAZ zones of remelting as the above layer is deposited.

4.5 Computed Tomography Inspection

4.5.1 Experimental Procedure

Computed tomography, or CT inspection, is a computerized x-ray imaging process where combinations of many 2-dimensional measurements are taken from different angles and joined together to form a 3D reconstruction of an object. CT inspection is a popular non-destructive test to search for voids, defects, and cracks within an object. To investigate the extent of porosity present in the samples, prior to tensile testing, several specimens from each batch were inspected for internal defects using a Zeiss Metrotom 800 Computed Tomography system. Due to the large time investment in performing CT inspection, 5 out of the 20 specimens were inspected: 2 0° specimens, 2 15° specimens, and 1 30° specimen. In industry, inspection is costly, so oftentimes it is only performed on a sampling of the population. 100% lot inspection is used in some cases, however, as CT inspection is time consuming, computationally expensive, and has volume limitations, it must be used strategically. Thus, a smaller sampling of specimens is tested using CT and the results displayed in the section below.

The CT scans are obtained with a tube voltage of 226 kV, 3.00 mA current, and 0.5 Cu filter. The voxel size is 23 μm per side. The pore detection is performed in VGSTUDIO MAX – a VolumeGraphics software tool used to visualize and analyze industrial CT data. Within the software tool is a pore detection algorithm called EasyPore that is used to look for voids and porosity within the components.

4.5.2 Porosity Results

It is clear from looking at the pore data and reconstructed volumes that porosity is present in varying quantities within the different samples. The number of pores, their mean size, and spatial distribution varies between the different batches, which is cause for closer analysis. Despite the fact that the same nominal build parameters are used, something changes from build to build that causes significant differences in void formation. This differentiation highlights the sensitivities of the process to the variations in the large number of inputs, such as small perturbations in powder flow, gas flow, and nozzle standoff distance. Additionally, it is important to consider the effect that differences in geometry may have on the deposition process, namely in terms of the interlayer delay time – the time it takes for the laser to scan the same XY (or UV in non-planer slices) location on subsequent layers. Generally, the larger the feature cross-section, the longer it takes for the laser to scan the entire slice. By the time the laser returns to the same location on the next layer, more heat has dissipated and the initial process zone temperature ($T_0(x,y,z)$) of the selected location is lower. The initial temperature of the process zone location is significant for two reasons. First, T_0 affects the temperature and size of the melt pool; second, T_0 influences the thermal gradient and solidification cooling rates. In this way, differences in cross-sectional area may influence differing levels of porosity due to the different thermal conditions.

Porosity data is analyzed using several different techniques. A normalized histogram looks at the probability density function of pore size and pore sphericity as an indicator of the mode of porosity formation and the impact that it may have on mechanical strength. A correlation matrix is employed to investigate any correlation between pore location and pore size and shape. The pore distribution is visually analyzed to look for regions of large increases in pore prevalence and to try to determine if they seem to congregate at specific heights within the gage section, indicating interlayer porosity. Finally, the effective cross-sectional area of the gage cross-section as a function of z-height is approximated using aspherical pore assumption. The tensile behavior of a material is a function of

intrinsic material properties, as well as the cross-sectional geometry of the specimen. The presence of porosity effectively reduces the cross-sectional area and the reduced cross-section cannot be captured using conventional contact external dimensional measurement techniques.

A summary of the average pore size and its standard deviation as well as the total number of pores detected for each specimen is presented in ***Table 14***. **Figure 30** presents normalized histograms of pore diameter for each of the build orientations investigated. Both the 0° and 30° samples show a log-normal distribution. There is a lower limit on the minimum detectable pore size – 0.023 mm – that is a function of the voxel size. As a result of the several porosity modes that govern pore size and shape, the histograms presented represent the convolution of multiple porosity formation mechanisms on a single plot. The 15° plot does not show as clear of a distribution pattern as the other builds. There is a grouping of pores detected in the under 0.13mm region and then a few counts of pores detected in the upper half of the histogram region. The 15° build clearly has a significantly fewer number of overall pores detected, which makes it challenging to fit a probability distribution to the data. However, the lack of pores exhibited on the upper range of detected pore sizes may indicate a significant improvement in the reduction of LOF defects. The 30° build shows fewer large pores, as well, especially when compared with the pore size distribution of the 0° samples. This finding is significant, as large, irregular defects reduce the strength of a component significantly more than smaller pores due to the increased reduction in effective area. Depending on the sphericity and orientation of the pores, some may lead to a higher local stress field around the edge of the void, leading to premature crack propagation.

Table 14: *Porosity Results for all 5 test samples using X-Ray CT measurements*

Specimen	# of Pores	Avg. Pore Diameter (mm)	Standard Deviation, Avg. Pore Diameter (mm)
0° - 1	259	0.142	0.097
0° - 5	377	0.135	0.093
15°-1	61	0.157	0.045
15°-4	17	0.164	0.092
30°-2	248	0.111	0.032

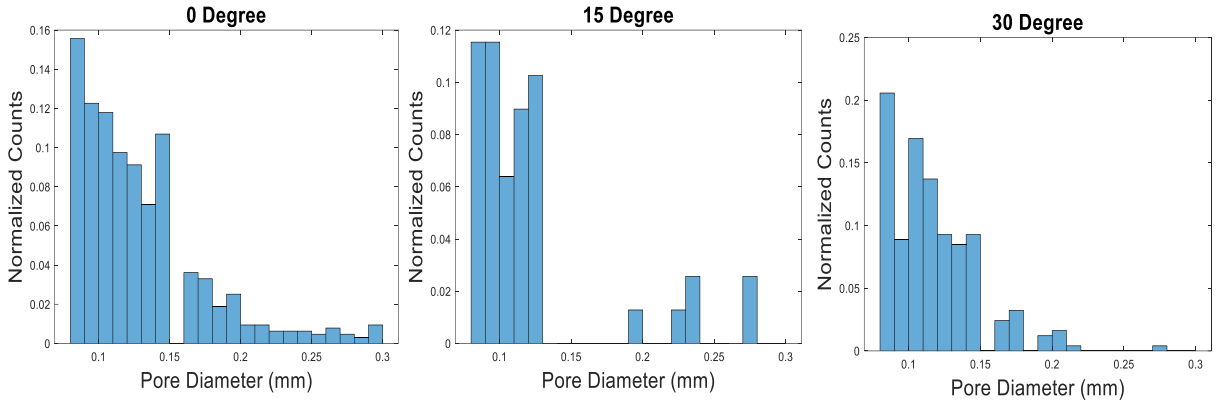

***Figure 30**: Normalized histogram of pore diameter for the: a) 0° build b) 15° build and c) 30° build*

Based on the three correlation matrices presented (**Tables 15-17**), the location of the pore within the sample shows little to no correlation with pore morphology. In the samples inspected, porosity does not seem to change size and shape as the distance from the substrate increases. However, the z-axis for the 15° and 30° specimens are along the axis of the tensile specimen and do not reflect the rotation of the layers. The lack of correlation result suggests either that the cooling cycles may be largely consistent throughout the build or that extreme changes in material temperature during the build due to unplanned stops results in large variations in T_0 values throughout the build.

Susan and Brooks suggest that interlayer porosity generally occurs in regions of close proximity to the substrate or between unmelted tracks when solidification rates are high and there is a lack of sufficient energy input to completely melt the filler material [91]. In the 0° build, large, irregular pores are seen throughout the material, indicating that the process is poorly controlled and that high solidification rates endured for each layer in the build due to unplanned stops. The existence of high solidification rates may be due to the relatively low heat input of laser DED and the time delay between when the laser passes over the same location in two different layers, allowing the region to cool significantly between subsequent layers, or it may have resulted from the need to pause the build periodically to adjust the standoff distance. As expected, there is a high negative correlation between

pore diameter and sphericity due to the different formation mechanisms between the large and irregular LOF defects and the smaller, more spherical gas entrapment flaws.

Table 15: *Correlation Matrix 0° Build*

0° Build	*Diameter [mm]*	*Sphericity*	*Pos. x [mm]*	*Pos. y [mm]*	*Pos. z [mm]*	*Projected size x [mm]*	*Projected size y [mm]*	*Projected size z [mm]*
Diameter [mm]	1.000							
Sphericity	-0.788	1.000						
Pos. x [mm]	0.044	-0.052	1.000					
Pos. y [mm]	0.033	0.040	0.025	1.000				
Pos. z [mm]	-0.094	0.113	0.151	0.062	1.000			
Projected size x [mm]	0.921	-0.748	0.011	0.025	-0.092	1.000		
Projected size y [mm]	0.775	-0.605	0.108	0.032	-0.032	0.535	1.000	
Projected size z [mm]	0.414	-0.249	0.101	0.018	-0.006	0.328	0.563	1.000

Table 16: *Correlation Matrix 15° Build*

15° Build	*Diameter [mm]*	*Sphericity*	*Pos. x [mm]*	*Pos. y [mm]*	*Pos. z [mm]*	*Projected size x [mm]*	*Projected size y [mm]*	*Projected size z [mm]*
Diameter [mm]	1.000							
Sphericity	-0.475	1.000						
Pos. x [mm]	-0.134	0.641	1.000					
Pos. y [mm]	-0.198	-0.419	-0.466	1.000				
Pos. z [mm]	-0.035	0.304	0.382	-0.096	1.000			
Projected size x [mm]	-0.140	0.047	-0.412	0.234	-0.226	1.000		
Projected size y [mm]	0.708	-0.521	-0.291	-0.075	-0.161	0.001	1.000	
Projected size z [mm]	0.478	-0.549	-0.404	0.209	-0.171	0.319	0.517	1.000

Table 17: *Correlation Matrix 30° Build*

30° Build	*Diameter [mm]*	*Sphericity*	*Pos. x [mm]*	*Pos. y [mm]*	*Pos. z [mm]*	*Projected size x [mm]*	*Projected size y [mm]*	*Projected size z [mm]*
Diameter [mm]	1.000							
Sphericity	-0.478	1.000						
Pos. x [mm]	0.012	0.037	1.000					
Pos. y [mm]	-0.037	0.005	0.126	1.000				
Pos. z [mm]	0.069	-0.042	-0.050	0.075	1.000			
Projected size x [mm]	0.817	-0.483	0.029	-0.070	0.009	1.000		
Projected size y [mm]	0.919	-0.406	0.039	0.007	0.079	0.703	1.000	
Projected size z [mm]	0.848	-0.450	0.028	0.049	0.060	0.709	0.780	1.000

LOF may be caused by insufficient melting and bonding of the powder stream with the parent material due to either rapid conduction of heat away from the melt pool or a lack of energy from the laser. The extent to which LOF defect accumulation is prevalent throughout the build or concentrated to one or even a few layers provides some feedback on whether the nominal laser power used was inadequate or if something may have caused a drop in the energy density (J/mm^2), such as a defocusing of the laser. If there is a mismatch in the programmed layer-height and the actual deposition layer height then that error may accumulate as more layers are added, as well. Eventually, either the deposition head is too close to the surface, causing the resulting tracks to be thinner than originally accounted for, with insufficient overlapping potentially causing voids to form between tracks, or the deposition head is too far from the surface and the energy density decreases. If this cyclical pattern is repeated throughout the build, as the operator periodically adjusts the standoff distance, a periodic function of porosity formation versus build height may be seen. If the LOF defects are seen consistently throughout build height, then it may simply mean that it is due to some combination of the many contributing factors, such as substrate and component geometry, nozzle wear, condition of the deposition surface, contamination on the laser lens, or the programmed laser power being too low. However, Taheri demonstrates that increasing the power of the laser to prevent harmful LOF defects will also increase the likelihood of gas porosity due to the increase in enthalpy [43].

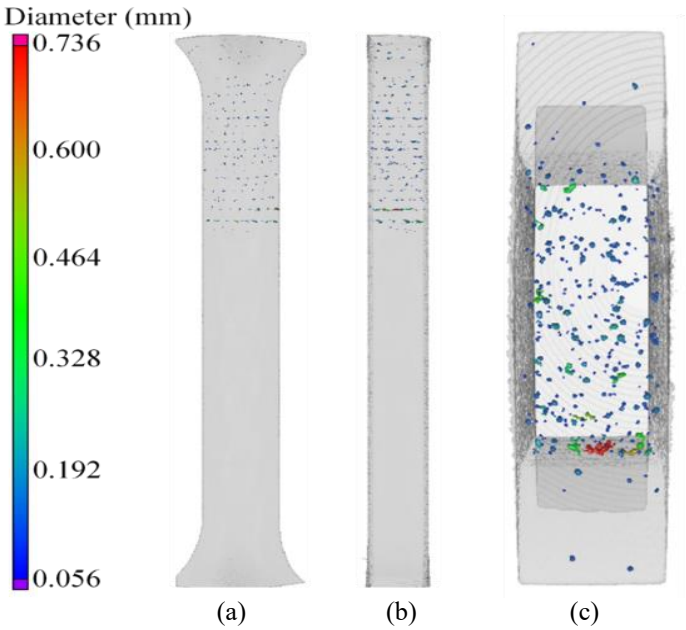

***Figure 31**: Internal porosity of 0° specimen a) front view b)side view c) top view*

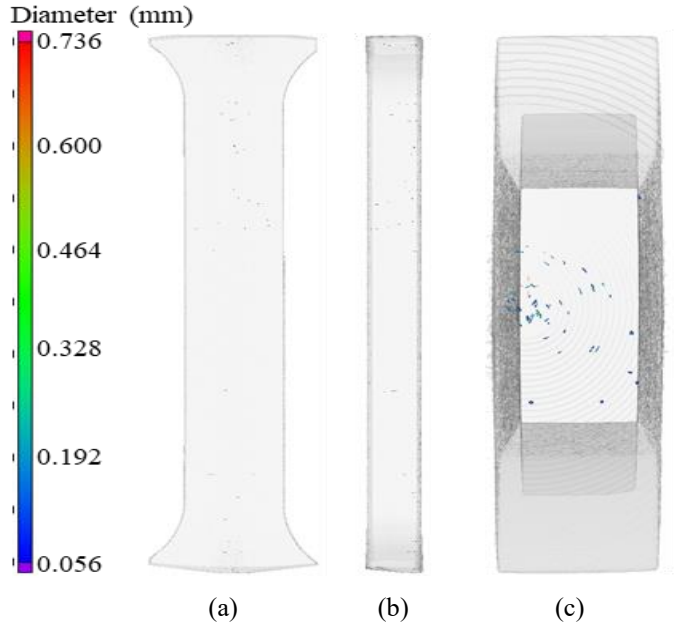

***Figure 32:** Internal porosity of 15° specimen a) front view b) side view c) top view*

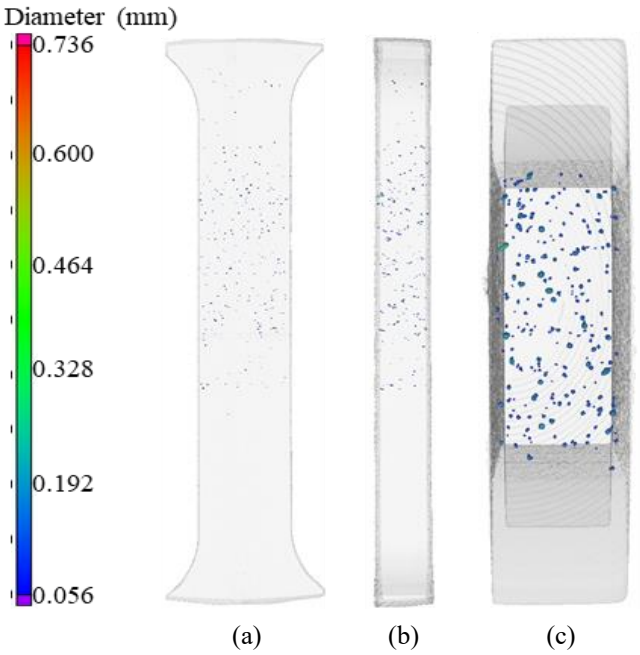

Figure 33: *Internal porosity of 30° specimen a) front view b) side view c) top view*

Using a spherical approximation of pore shape for ease of computation and analysis in Matlab, the cross-section density is plotted as a function of position along the z-axis. The coordinate systems are all aligned in different locations for each of the specimens, so little information can be gleaned from the absolute scale. However, the z-position is scaled, so the distance between spikes in pore area fractions, which corresponds to a drop in layer density, is accurate. For the three orientations investigated (**Figure 34**), the 0° samples suffered from significant drops in cross-section density corresponding to interlayer bonding defects. The 15° samples show some drops in load bearing area, however the minimum density as approximated using this method is 98.6%, which is well above the 0° samples (area fractions in the region of 91 and 92%). Despite the presence of significant porosity in the 30° samples, the investigated sample is above 99% dense across all layers. To see the extent to which the porosity forms in between layers, the plane of examination is rotated 30° about the X-axis so that it aligns with the layers. In the rotated sample (**Figure 35**), the least dense layer decreases to 98.2%. Visually, the rotated sample seems to show the presence of pores forming along specific layers,

however all cross-sections measure at least 98% dense. The slight decreases, along with the sharp decreases that appear to occur in multiples of 0.5 mm increments, indicate the presence of some interlayer porosity. It is possible, however, that the majority of the porosity is due to gas-entrapment or simply interlayer porosity that is well-distributed along the length of the gage section.

There are challenges in controlling DED processes in a time-invariant manner, where the nominal parameters are set at the beginning of the build and limited adjustments are able to be made as the material is being deposited. This complexity illuminates the need for extremely well-defined process parameter studies that reflect the component geometry, in addition to testing build parameters for the material system and equipment configuration. Furthermore, it highlights the need for enhanced process monitoring and control, both where LOF defects can be detected and flagged during the deposition process, and where the laser power can be finely tuned to maintain a constant predetermined melt pool size and layer height.

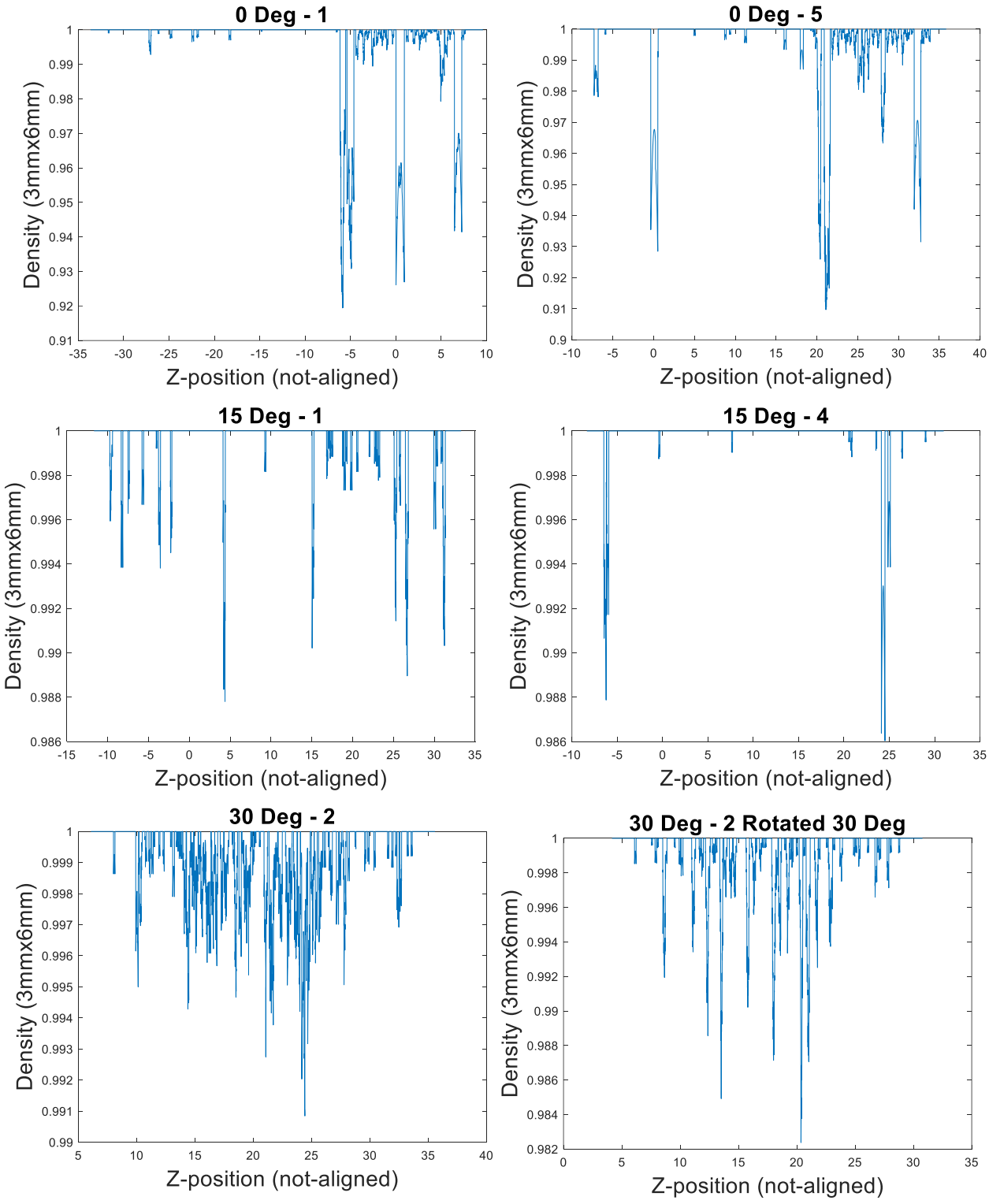

Figure 34: *Cross-section density*

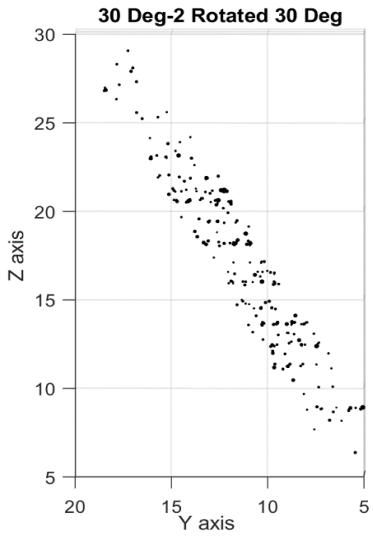

Figure 35: *Porosity of 30 degree sample rotated*

4.6 Mechanical Properties

4.6.1 Tensile Testing Experimental Procedure

In order to investigate the effects of build orientation on hybrid wrought-DED specimens, quasi-static uniaxial tension testing is performed on all specimens. All tests are conducted at room temperature using an Instron 5982 Universal Materials Testing System – an electromechanical test system with a maximum load capacity of 100 kN, ideal for conducting room temperature monotonic tension tests. A contact extensometer measuring 25.4 mm between arms is physically attached to the gage section of the specimens and used to measure bulk deformation until 10% strain, at which point it is removed to prevent damage to the instrument. The crosshead displacement is also tracked throughout the experiment, and, after the extensometer is removed, crosshead displacement is used as the measurement of strain. However, due to compliance in the system, a correction factor is employed that is determined by comparing the relative stiffnesses of the specimen and the testing machine before and after yielding.

The specimens are manually loaded and aligned into the machine, then fixtured in place using wedge-style grips. The bottom grip is fixed, while the top grip moves upwards in the machine to incrementally apply tension to the specimen. The tests are controlled using displacement, as opposed to stress, to prevent rapid acceleration of the machine during the onset of necking prior to ultimate failure. The ASTM E8 standard allows for the use of a stepped, two-speed crosshead control. One crosshead speed is employed through the yield point and then a second faster speed is allowed from beyond yielding to ultimate failure. The allowable crosshead speed for determining elastic properties to the yield point is equal to 0.015±0.003 mm/mm/min of the original reduced parallel section, which equates to a crosshead speed of approximately 0.5 mm/min for a 32 mm gage length specimen. However, after yielding is detected, the machine may accelerate to between 0.05 and 0.5 mm/mm/min, or between 1.6 and 16 mm/min for the specimens in this study. The lower limit, 1.6 mm/min, is selected to be more conservative and ensure satisfactory data is collected from the tests. After yield is detected based on an automatic Young's Modulus calculation performed within the Instron control software (Bluehill Universal) the crosshead increases to the plastic region displacement rate over a 3 second transition period, in order to limit the effects of rapid changes in crosshead displacement.

In addition to the testing of the 20 wrought-AM specimens, 5 specimens are prepared of only wrought material. This wrought material – annealed and cold-drawn 316L SS– is tested in order to develop the testing procedure before conducting the tests on the printed specimens, and also serves as a baseline for how the wrought, conventionally produced material behaves in comparison.

4.6.2 Tensile Results

The averaged values and standard deviation for Young's Modulus, yield stress, ultimate tensile stress, and maximum elongation to failure for each build orientation and wrought material are displayed in **Figure 36**.

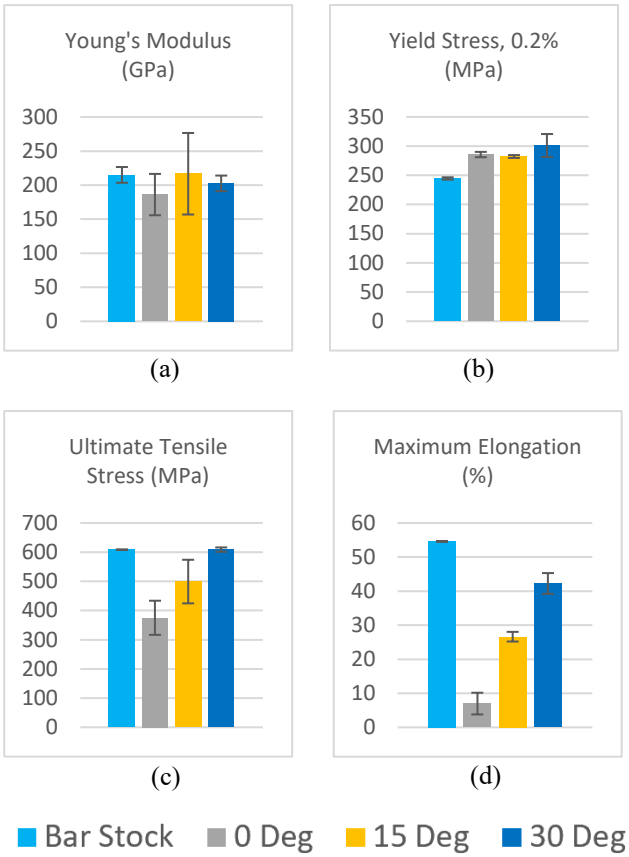

Figure 36: *Bar charts of mechanical property measurements for each batch of specimens a) Young's Modulus b) Yield Stress c) Ultimate Tensile Strength d) Maximum Elongation*

The modulus values are determined using a linear regression analysis performed within the Bluehill software. The resulting calculated values do not demonstrate a clear connection to build orientation. The 15° sample has the highest calculated Young's Modulus, as well the least amount of porosity, but also experience the largest standard deviation. The 0° specimen presents with the lowest modulus value. This result is significant when considering the effective load bearing area of the components. Depending on the build orientation, the presence of interlayer porosity has a varying impact on the actual cross-sectional area of the specimen. As there is a complex relationship between pore size, shape, and distribution and mechanical properties that is not fully understood, cross-sectional density provides one method of comparing the relative behaviors of porous metals. It is not clear, however, the impact that the proximity between reduced density slices have. The CT-inspected

0° samples are found to have a minimum cross-section density of 91.5% as compared to 98.7% and 99.1% for the 15° and 30° builds, respectively. As expected, in the presence of interlayer porosity, the cross-sectional area is more affected the smaller the angle is between the uniaxial loading direction and build direction. While that seems to clearly explain the significant reduction seen in the 0° modulus, it does not explain why the 15° samples present a higher modulus than the 30° samples, despite also having a lower minimum slice density, albeit only by 0.4%. The difference may be a function of the bulk density and relative porosity measurements, however, the large variance in the mean 15° modulus expectation value does obscure the significance of that conclusion. Adjusted Young's Modulus values based on the reduced area calculations are presented in ***Table 18***. Of note, the wrought-DED specimens display elastic behavior within 5.3% of the wrought material. The lack of a clear correlation between build orientation and elastic properties is reflected in the linear correlation value between build orientation and Young's Modulus in **Table 19**.

Table 18: *Adjusted Young's Modulus Values*			
Orientation	Elastic Modulus (GPa)	Min. Load Bearing Area (%)	Adjusted Elastic Modulus (GPa)
Wrought	215.04	~100	215.04
0°	186.14	91.5	203.53
15°	216.74	98.7	219.74
30°	202.66	99.1	204.50

The results from tensile testing suggests that the σ_{YS}, as calculated by the 0.2% secant method, increases as the angle of the build orientation increases, as reflected by the moderately high positive correlation coefficient. All of the DED-wrought samples had a higher σ_{YS} than the wrought material tested, which can be expected. Due to the Hall-Petch relationship between grain size and yield strength, the measured values in this study are significantly less than those found in the literature for purely AM material (***Table 4***). This can also be expected – according to the rule of mixtures for determining elastoplastic mechanical properties in bimetallic materials, the bulk yield strength will be less than the higher yield strength material, though the exact amount by which it differs is dependent on factors such as the Poisson ratio, volume fraction of each material, and each material's individual elastoplastic properties. In general, smaller grains increase the yield strength of a metal,

due to the increased impediment to slip and dislocation movement through the material. Generally, in metals, grain boundaries serve to interfere with the movement of dislocations. The specimens printed at the 30° orientation to the tensile direction show the highest σ_{YS} (301.04 MPa), followed by the 0° and 15° samples (285.56 MPa and 282.15 MPa, respectively). As seen in the multi-track, multi-layer 316L microstructure analyzed via optical microscopy, columnar grains grow parallel to the largest thermal gradient. This result is meaningful when considering that it changes the number of grain boundaries along the loading direction. The change in mean path length between different orientations depends on the grain size and aspect ratio. However, it also depends on the initial orientations of the grains. As the grains generally form normal to the melt pool boundary, some are oriented parallel to the build direction, while most have a significant component of their major axis tilted at some angle. The micrographs reveal batches of columnar grains; however, they do not seem to dominantly orientate themselves in any one direction to induce a clear effect on yield strength. However, grain aspect ratio, if allowed to be the dominating factor, will have the impact of increasing the yield strength as the uniaxial loading and build direction diverge.

The mean σ_{UTS} for the 0° orientation measures approximately 20-25% lower than the other samples tested and is accompanied by a maximum elongation to failure that is considerably lower than the rest (6.98% elongation) of the samples tested. The significantly worse σ_{UTS} and elongation measurements reveal the noteworthy influence that porosity has in determining ultimate failure within that build. The highest σ_{UTS} belongs to the wrought material (608.53 MPa), presumably due to the lack of internal defects and absence of significant residual stresses within the material. The σ_{UTS} does appears to be mainly influenced by the extent of porosity and internal defects present within the samples, as the next highest σ_{UTS} is the 15° samples (499.27 MPa), followed closely by the 30° samples (463.39 MPa). The sizable standard deviations associated with the mean σ_{UTS} measurements suggest that porosity plays a significant role in the maximum stress that each specimen can experience before failing. While certain conditions may lend themselves to increases in the

probability of void formation during the build process, the exact pore morphology and spatial distribution within the specimen is stochastic in nature. As a result, component failure is largely nondeterministic. The connection between the presence of internal defects and the scatter in σ_{UTS} values are apparent, as the σ_{UTS} standard deviation increases with the number of pores detected in the specimen. As more detectable defects appear in the specimen, so do the possible states of internal stress concentrations within the specimen. However, it is significant that the pore-laden 0° specimens fair considerably worse than the porous 30° specimens, possibly due to the higher number of larger pores or the fact that the pores tend to be close to one another.

The maximum elongation measurement returned with a highly positive correlation with build orientation (**Table 19**). The most ductile material is the wrought bar stock, which experiences maximum strain at failure of 0.5462 ± 0.0005, followed by 30° (0.4226 ± 0.0305), 15° (0.2663 ± 0.0142), and 0° (0.0698 ± 0.0319). The 30° samples exhibit higher ductility than the 15° despite the detection of significantly more pores. The results support the assertion that the ductility increases as the direction of uniaxial stress pulls more in line with the deposited tracks, as opposed to across the layers. This may be an outcome of the mechanical fibering that takes places in DED parts. Elemental segregation, as well as internal voids and defects, generally impede deformation mechanisms and tend to occur along melt pool boundaries. The deposited tracks represent extended regions of defect-free material. Due to the rotation of the bi-directional zig-zag scanning path, the tracks lie along both the X and Y axes on alternation layers. As the axial loading aligns itself in an increasingly perpendicular fashion to the build direction, half of the deposited layers will contain tracks that are along the axis of tension. This allows for increased elongation as the plastic deformation is impeded by melt pool boundaries. Additionally, the numbers of pores appear to have a diminishing impact on elongation; this is demonstrated in the 30° sample, which contains the highest maximum elongation but also a significant number of pores.

Several one-way ANOVA tables are generated to identify to what statistical confidence level variations in mechanical properties can be attributed to changes in build orientation (**Table 20-23**). Based on the ANOVA, the Young's Modulus (**Table 20**) does not meet the 95% confidence interval to claim statistical significance. The closeness of the means and the size of the variance in the reported values make it impossible to reject the null hypothesis. The p-value corresponding to the build orientation effect on yield strength is 0.031, just below criteria of 0.05, indicating that it is possible that the build orientation does play a significant role in determining the yield strength of the bi-metallic specimens (**Table 21**). The P values of 0.002 and 0.000 for σ_{UTS} and maximum elongation (**Table 22-23**), respectively, clearly pass the confidence test. However, additional specimens built at other orientations, as well as repeated builds with the same orientation, would serve to further bolster these results.

Table 19: *Correlation matrix of build orientation and mechanical properties*

	Orientation	*UTS*	*Young's Modulus*	*Yield (Offset 0.02 %) : Tensile stress*	*Yield (Offset 0.02 %) : Tensile strain*	*Max Elongation*
Orientation	1.000					
UTS	0.612	1.000				
Young's Modulus	0.185	0.295	1.000			
Yield (Offset 0.02 %) : Tensile stress	0.465	0.206	0.014	1.000		
Yield (Offset 0.02 %) : Tensile strain	0.019	-0.373	-0.411	0.011	1.000	
Max Elongation	0.984	0.615	0.172	0.379	0.078	1.000

Table 20: *ANOVA Young's Modulus*

Source	Sum Sq.	df	Mean Sq.	F	Prob>F
Orientation	2.8142 e+09	2	1,4071e+09	0.85	0.4466
Error	2.30574e+10	14	1.64696e+09		
Total	2.58716e+10	16			

Table 21: *ANOVA Tensile Strength, Yield (0.2% offset)*

Source	Sum Sq.	df	Mean Sq.	F	Prob>F
Orientation	1077.84	2	538.918	4.49	0.0311
Error	1679.18	14	119.941		
Total	2757.01	16			

Table 22: *ANOVA Tensile Strength, Ultimate*

Source	Sum Sq.	df	Mean Sq.	F	Prob>F
Orientation	242259.3	2	121129.6	9.91	0.0021
Error	171108.2	14	12222		
Total	413367.5	16			

Table 23: *ANOVA Maximum Elongation to Failure*

Source	Sum Sq.	df	Mean Sq.	F	Prob>F
Orientation	0.3446	2	0.1723	245.76	1.249e-11
Error	0.00982	14	0.0007		
Total	0.35441	16			

4.6.3 Optical Measurement of Dual Strain Behavior

To capture the dual strain behavior of the bimetallic specimen an optical method is employed. The gage section of the tensile specimen is monitored throughout the test using a high-speed camera. Four black dots are applied to the length of the gage length, two on the upper half of the specimen and two on the lower in the AM and wrought regions. The camera captures images of the tensile test at a 5 Hz sampling frequency. The frames are downloaded into GOMCorrelate, a commercially available product from GOM, for further analysis. Facets are applied digitally to the frames. Facets are matrix subsets of pixels, in this case 31x31. Each pixel has a corresponded grey-level assigned and the quality of the facet is determined by the amount of grey-level variation including the contrast between grey-levels of adjacent pixels. The 4 dots are marked with facets, and the facets are tracked from one frame to the next. In this way, the strain in each region of the dual material specimen can be monitored throughout the test. The percent length change between the dots are obtained for each sample as well as the strain rate based on the known sampling rate. The recorded data is smoothed using a moving average and the values plotted.

Both the percent strain and percent strain rate for the wrought, AM, and combined, bulk material are plotted in **Figure** 37. The strain plots are interesting to look at, however, as the dots are applied manually to each specimen, they do not all have an equal starting length or are they perfectly

positioned in relation to where the specimen fails. As the tensile tests are displacement-controlled tests the bulk strain plotted over time should follow a strain line with a slope corresponding to the cross-head velocity For the most part, the bulk deformation follows that trend, but there are some deviations at the beginning and end of the test when the specimen is undergoing preloading and at the end, as the part necks and fails.

For the three build orientations tested, the deformation appears to start in the wrought region. In the 0° and the 15° samples the deformation in the wrought region rapidly departs from the level of strain seen in the AM material. However, after some time the rate of deformation in the wrought region begins to decrease, presumably due to strain hardening behavior, and then the majority of further plastic deformation occurs in the AM portion. In the 0° and 15° samples the AM material increases its strain rate and continues to deform until the maximum load is reached and the material begins to fail. The behavior of the 30° samples behaves slightly differently. There is less of an initial divergence in strain values between the two regions and they appear to follow a similar strain rate profile, until final failure.

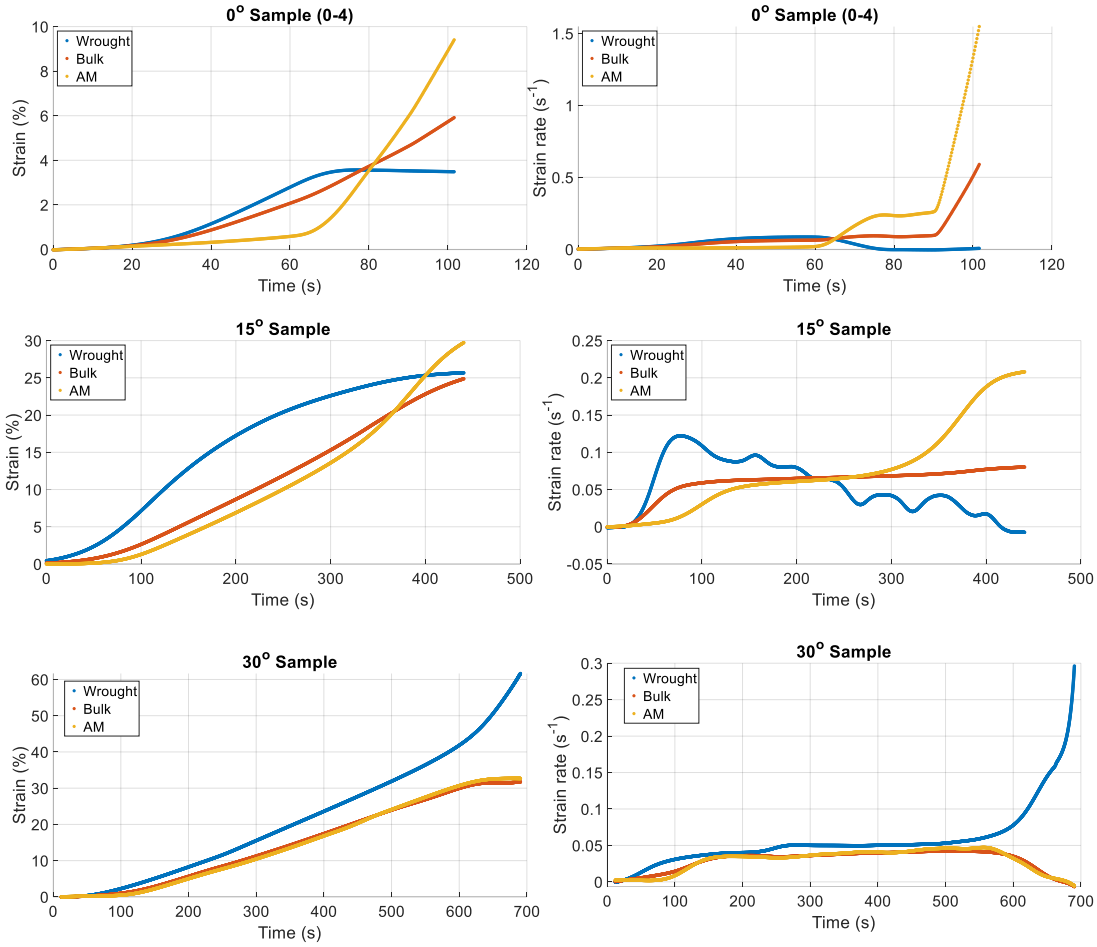

Figure 37: *Plots of strain and strain rate over time for a 0°, 15°, and 30° sample.*

4.7 Failure Analysis

The failure location appears to be consistent within the different builds (**Figure 36**), an indication of negligible misalignment effects in the uniaxial tension tests, which could also result in failure in the grip section. As the DED samples are deposited on wrought substrate, they exhibit unique strain behaviors due the dual microstructures present, effectively behaving as a bi-metallic specimen even though the two metals are similar in composition. To obtain additional information about the fracture mechanism, the fracture surfaces are imaged using a Zeiss Ultra 60 FE-SEM, which utilizes a Schottky FEG gun and Gemini column to obtain high resolution sub-micron scale images.

The SEM images presented are captured using 15.00 kV accelerating voltage, an aperture size of 30 μm, and working distances ranging from 10.2mm to 12.8mm.

Due to the 0° specimens failing prematurely, there is minimal deformation seen in those samples. The reduced cross-sectional area at the failure zone measures 97.1% of the original gage area and each specimen fails in the DED region. Furthermore, the specimens all appear to fail in the same location, indicating the presence of a weak layer or region that dominates the UTS and elongation performance of the samples. As seen in **Figure 37,** the SEM images confirm the presence of several indicators suggesting lack of sufficient energy density. Interlayer defects, such as partially melted powder particles, can be seen along the fracture surface. The objects identified as particles measure roughly 100 μm across, matching the PSD distribution histogram presented in **Figure 9**. The particles also show what appear to be satellite particles fused to the surface of the larger particle, similar to the powder SEM images obtained earlier in **Figure 8**. **Figure 39** also depicts the outlines of the tracks themselves, indicating the lack of sufficient melting and metallurgical bonding in the failure region. The fracture surface is split into levels, suggesting weak bonding and poor melting in at least two interlayer regions. The lack of dimpling on the surface indicates the lack of micro void coalescence, which is indicative of brittle failure.

All 15° samples, on the other hand, experience significant initial plastic deformation in the wrought region. After some time, the majority of the bulk strain is observed in the DED region. As with the 0° samples, all failure occurs in the DED region. However, the reduced cross-sectional area of the fracture surface measures 68.5% of the original gage area, a sign of ductile failure. The fracture surfaces in the 15° specimens occur at a 45° orientation (measured within ImageJ), indicating that failure occurs along the plane of maximum shear stress and that the failure plane propagates across multiple layers.

The 30° specimens exhibit slightly different strain behavior, with the yielding occurring at similar rates between the wrought and DED regions until necking begins. In these specimens, failure

occurs in the wrought material. The 30° samples exhibit the most necking behavior, with a reduced area 75.6% smaller than the original gage cross-section. Both the 15° and 30° samples show significant dimpling of the surface, which is a sign of ductile failure occurring as micro voids nucleate around different inclusions and coalesce as they grow to form dimples on the surface. The density of dimples on the surface is associated with less elongation because it means that the voids grew less before linking and failure. In order to quantify the average dimple size between the different samples, SEM images are imported into ImageJ and a line of known length is drawn. Observing the number of dimples that the line intersects across multiple different orientations, reveals similar dimple sizing between the 15° and 30° surfaces (≈.40-.50 μm).

(a) (b) (c)

Figure 38: *Example of tested a) 0 Degree specimens b) 15 Degree specimens c) 30 Degree specimens*

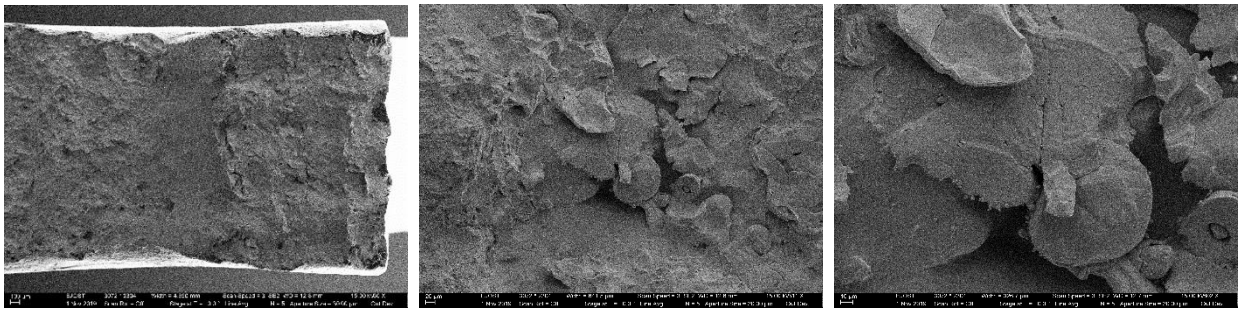

Figure 39: *SEM images of 0 Degree fracture surface*

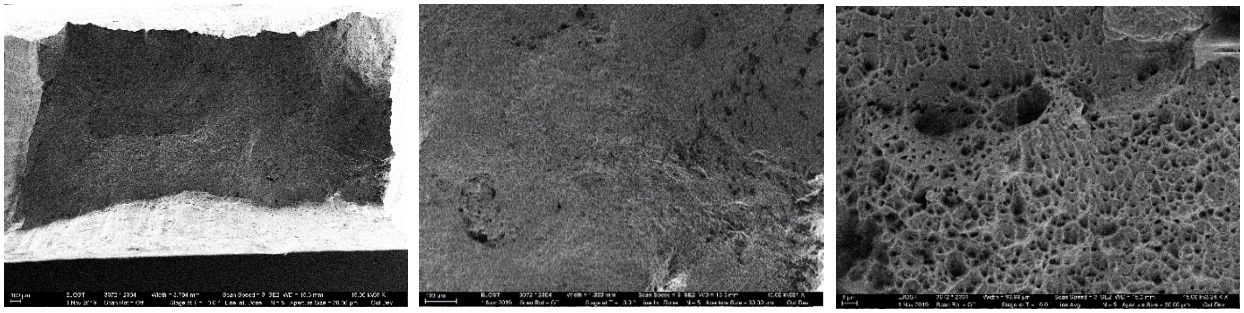

Figure 40: *SEM images of 15 Degree fracture surface*

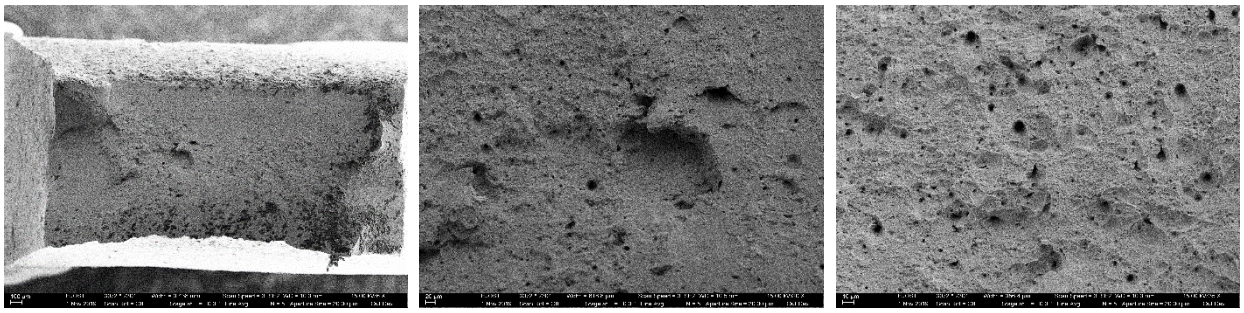

Figure 41: *SEM images of 30 Degree fracture surface*

CHAPTER 5: CONCLUSIONS

5.1 Conclusions

Based on the graphical and statistical methods used to analyze the effects of build orientation on mechanical properties of DED-wrought specimens, there is enough of a correlation that it needs to be taken into consideration when designing hybrid manufacturing processes. Microstructure, size, distribution, and orientation of porosity, and the presence of residual stresses in LM produced parts are all factors in determining tensile performance. Therefore, it is challenging to identify the dominating factor causing the different behaviors as there is often more than one influencing factor at play. However, a few conclusions can be drawn from the work conducted in this study:

1. The dominant form of porosity detected within this samples appears to be related to the presence of interlayer defects. The extent to which interlayer defects serve to reduce to the effective load bearing area of the material depends on the orientation of the layers, ranging from an 8% reduction to less than 1%.
2. While elastic behavior does not appear to be correlated to build orientation, σ_{YS}, σ_{UTS}, and maximum elongation do show a statistical correlation. This behavior appears to hold true despite varying degrees of porosity among the different builds.
3. The lower angle build orientations failed in the AM material, whereas the 30° specimens failed in the wrought region despite possessing a relatively high level of porosity. It is believed that the improved ductility in the high orientation samples is due to the axis of uniaxial tension lying more in line with extended tracks of defect free material.
4. Monitoring the strain rate throughout the duration of the tests in the two regions reveal different plastic behavior throughout the test. The differences in interaction between the two materials are due to differences in rates of cold working between the different build orientations. However, further work can be done in this area to confirm this postulate.

The VolumeGraphics reconstructions of the pore data reveal a noticeable difference in the distribution of porosity throughout the specimen based on build orientation. The 0° samples suffer from significant voids that form and cluster around distinct locations in the build orientation. The clustering behavior is less visible in the 30° and the 15° specimens. However, the 30° samples reveal some interlayer porosity when they are rotated. The effect of interlayer porosity and orientation is that it may cause differences in mechanical behavior, such as elastic modulus, may be due to the difference in effective cross-sectional areas resulting from variations in defect distribution. When the 0° orientation is corrected for the reduced loading area the modulus value increased to about 202 GPa, which insignificantly closer to the modulus for the other DED and wrought specimens. This leads one to believe that the formation of interlayer porosity plays a significant role in the elastic performance of 316L DED samples

Despite the varying levels of porosity present within the different builds, the following trends emerged. Young's Modulus has little to no significant correlation to build orientation. For σ_{YS}, all of the wrought-AM hybrid samples measure higher than the wrought material but is significantly less than for the pure AM material. The 30° samples present the highest yield measurement believed to be caused by the decrease in effective grain size along the loading direction. Even though this conclusion largely comes from literature review, it is challenging to make in that case in this study because there is no overwhelming columnar grain orientation discovered during the OM investigation.

The maximum elongation measurements show the clearest relation between build orientation ductility. Even though the 30° specimens have significantly higher porosity over the 15° samples, they still experience about 50% more elongation than the 15° values. The clearest explanation seems to originate from the concept of mechanical fibering and the strength of materials pulling across multiple layers of pores and hard inclusions versus along it. It is interesting to note at

in the AM-wrought samples the yield strength and elongation both are highest for the highest orientation build tested.

The different orientations present more than just different mechanical values, such as stiffness, yield, ultimate strength, and ductility, but by employing digital optical techniques it is possible to capture further anisotropic behavior. While the overall effects in a bulk specimen may be less noticeable, utilizing optical strain measuring reveals the immediate resistance to yielding in the 0° AM versus the 30° material that diverges, but less significantly. The 15° samples perform in the middle. As the deformed material strain hardens, the other region begins to strain more and more depending on the relative fraction of resistance to further plastic deformation, However, in the case of the 0° samples, the AM region reaches its maximum load and begins to fail rapidly.

It is shown that build orientation should be taken into consideration when working with DED-wrought materials. However, the effects of build orientation appear to be significantly less extreme than if the material is are constructed of solely AM material. Safety factors may be utilized by design engineers to account for the variation in properties. However, the most significant departure from isotropic behavior is in the ductility of the specimens. The work presented here, while providing a good initial investigation, should be supplemented by follow experiments.

5.2 Limitations

To improve the conclusiveness of the results presented, several limitations in the work must be overcome. The primary challenges facing the work are the sampling size, the difficulty in separating variations in material properties resulting from build-to-build variance and those strictly related to build orientation, and determining the primary contributing factor to the tensile specimen performance. Due to the restricted sample size it is somewhat difficult to try and clearly define the different levels of significance of all of the different factors involved.

Due to the costs associated with operating the hybrid machine including material costs and the time required to process the samples it was not feasible to produce a large number of specimens. Utilizing smaller tensile specimens is one method to obtain an additional number of samples using the same amount of powder feedstock and machine time as is required for the 100 mm overall length specimens manufactured in this study. However, using smaller samples is accompanied by other challenges. Selecting a measurement sampling size must balance the trade-off between making enough observations to obtain a reasonably precise measurement with a practical budget. It is possible to use the gathered data on the variability of the population to determine the necessary sample size to meet a desired precision. If the required sample size is not feasible to produce, then the only option is to accept less precision. Through analysis of the experimental data the highest coefficient of variance present within the experiment can be taken as the worst-case-scenario and the necessary sample size to meet a specific confidence interval may be estimated. The largest coefficient of variation is 0.28 from the Young's Modulus 15° measurements. To estimate the mean within 10.5 GPa of the true mean with 95% confidence assuming normal distribution ($\alpha = .05$, $z\alpha = -2$) considering a coefficient of variance of 0.28, then the necessary sample size is about 130. Thus, if 130 samples are produced, then with 95% confidence the mean ultimate tensile strength can be estimated within 10.5 GPa of its true value. The associated costs with producing 130 samples is prohibitive, but by reducing the associated precision to 10% (~21 GPa), then the required number of samples for each build orientation reduces to 33, which is significantly more achievable.

The porosity, microstructure, and resulting mechanical performance seen in AM material are extremely susceptible to small deviations from the nominal build conditions. Due to the high number of process variables involved in DED there are many opportunities for the deposition process to deviate from the nominal conditions, and this is especially true when the process is controlled in an open-loop time-invariant manner. This sensitivity to the numerous process variables make it challenging to determine how much of the observed properties occur due to the process conditions

or due to the effects of changing the build orientation of the components. While valuable information is still gathered about how build orientation may be used to attenuate the effects of different build conditions, more insight could be gathered by employing different build strategies and increasing the number builds. Analyzing additional build orientations beyond the ones presented here would also provide more insight into the observed trends.

Another challenge encountered is the difficulty in stating with a high degree of confidence which of the numerous influencing factors affecting mechanical behavior are the primary influencer. Mechanical behavior is influenced by macro-defects such as porosity, microstructure defects including element segregation and secondary phase formation, and the presence and direction of residual stresses. Each of the observed macro- and micro-structures are influenced by both the layer-by-layer construction process as well as the changes in thermal history due to changing layer cross-section and heat conduction conditions. Additional experiments utilizing different build strategies, post-process heat treatments, and full material microstructure characterization would serve to address this limitation in the current research.

CHAPTER 6: FUTURE WORK

Many additional experiments are required to fully understand the complex phenomena that affect the mechanical properties of the material. The areas of interest for further work are broken down into process, structure, and properties. Further work in this area should further illuminate the interplay between those three areas. Additionally, a larger sampling size would allow for better stratification between the different properties under investigation.

In order to further understand the impact that the build process it has. More builds should be conducted both of orientations already tested and of new orientations. Not only would the additional samples provide for a more robust statistical analysis, but the effects of build to build variation could be compared to try and identify outliers.

However, in order to try and isolate the different phenomena that influence mechanical properties additional experiments need to be run that can modulate the various influencing factors, such as residual stress. Residual stress is mentioned in this study as a factor, but no work is done to attempt to quantify the presence of residual stress in the material. This may be done using a neutron detector or by measuring lattice distortions in XRD.

Of course, it is also possible to heat treat the material to relieve any residual stresses. However, performing heat treatments such as annealing will affect the grain structure and maybe even the porosity morphology. Regardless, testing specimens in various heat treat conditions would shed light on the influence of the various possible grain structures that exist.

Monitoring of the melt pool and process zone temperatures throughout the duration of the deposition would help to relate the effect of substrate and layer size to solidification rates and thermal gradients. The time it takes to scan a layer is identified as an important parameter, but without additional monitoring it is nearly impossible to know the exact relation between path planning and the resulting microstructure formation. The microstructure should be run through a more complete evaluation of metallurgical properties to quantify the changes that build orientation has on thermal

gradient and solidification rates. In this way, researchers can determine the exact grain structure, crystallographic orientation, elemental segregation, etc.

Additional future works in this area should aim to further correlate process decisions with the resulting microstructure and how that all affects the mechanical behavior.

REFERENCES

[1] B. Jackson, “LINCOLN ELECTRIC ACQUIRES BAKER INDUSTRIES FOR ADDITIVE MANUFACTURING BUSINESS LAUNCH,” *3D Printing Industry*, Apr. 05, 2019.

[2] M. Leino, J. Pekkarinen, and R. Soukka, “The Role of Laser Additive Manufacturing Methods of Metals in Repair, Refurbishment and Remanufacturing – Enabling Circular Economy,” *Phys. Procedia*, vol. 83, pp. 752–760, 2016, doi: 10.1016/j.phpro.2016.08.077.

[3] J. Scott *et al.*, “Additive Manufacturing: Status and Opportunities,” p. 36, 2012.

[4] S. Hendrixson, “AM 101: Hybrid Manufacturing,” *Additive Manufacturing*, Aug. 29, 2019. https://www.additivemanufacturing.media/blog/post/am-101-hybrid-manufacturing.

[5] “Developing an Additive Manufacturing DEDatabase for LPDED Repairs of Ti-6Al-4V Components: Viable Ti-6Al-4V Additive Manufacturing Repair.” America Makes, [Online]. Available: https://www.americamakes.us/wp-content/uploads/sites/2/2018/07/4037-SuccessStory_Final.pdf.

[6] I. Wright, “Hybrid Manufacturing & The Future of 3D Printing for Production,” *engineering.com*, Sep. 24, 2018. https://www.engineering.com/AdvancedManufacturing/ArticleID/17717/Hybrid-Manufacturing-The-Future-of-3D-Printing-for-Production.aspx.

[7] S. Hendrixson, “Lower Buy-to-Fly Ratios with Near-Net Additive Manufacturing,” *Modern Machine Shop*, Aug. 22, 2019. .

[8] “Cladding and additive manufacturing by laser metal deposition—the time of industrialization,” *Industrial Laser Solutions for Manufacturing*, Feb. 02, 2016. https://www.industrial-lasers.com/home/article/16486676/cladding-and-additive-manufacturing-by-laser-metal-depositionthe-time-of-industrialization.

[9] B. Gerard, “Fundamentals of HARDFACING by arc welding.” Welding Alloys Group, 2018.

[10] D. S. Gnanamuthu, “Laser surface treatment,” *Opt. Eng.*, vol. 19, no. 5, pp. 783–792, 1980.

[11] V. M. Weerasinghe and W. M. Steen, “Laser cladding by powder injection,” *Publ Ltd*, pp. 125–132, 1983.

[12] J. Mazumder, “State-of-the-art laser materials processing,” *ASME*, vol. 2, no. 115, pp. 599–630, 1987.

[13] A. G. Blake, A. A. Mangaly, M. A. Everett, and A. H. Hammeke, “Laser coating technology: A commercial reality,” *Laser Beam Surf. Treat. Coat.*, pp. 56–65, 1988.

[14] S. B. Doran, “The laser where flexibility ultimately means economy,” *Production Magazine*, 1987.

[15] K. Tanaka *et al.*, “New copper based composite for engine valve seat directly deposited onto aluminum alloy by cladding process,” *Jpn. Inst Met.*, vol. 57, no. 10, pp. 1114–1122, 1993.

[16] L. Shepeleva, B. Medres, W. D. Kaplan, M. Bamberger, and A. Weisheit, “Laser cladding of turbine blades,” *Surf. Coat. Technol.*, vol. 125, no. 1, pp. 45–48, 2000.

[17] J. L. Koch and J. Mazumder, “Rapid prototyping by laser cladding,” *Laser Mater. Process.*, pp. 556–557, 1993.

[18] W. Hofmeister, M. Wert, J. Smugeresky, J. A. Philliber, M. Griffith, and M. Ensz, “Investing solidification with laser-engineered net shaping process,” *JOM*, vol. 51, no. 7, p. 1999.

[19] M. L. Murphy, W. M. Steen, and C. Lee, “A novel prototyping technique for the manufacture of metallic components,” *Proc. ICALEO1994*, pp. 31–40, 1994.

[20] E. Toyserkani, A. Khajepour, and S. Corbin, “System and method for closed-loop control of laser cladding by powder injection,” 60/422606.

[21] K. A. Lorenz, J. B. Jones, D. I. Wimpenny, and M. R. Jackson, “A REVIEW OF HYBRID MANUFACTURING,” p. 13.

[22] *Machinery’s Handbook*. Industrial Press, 1980.

[23] I. Gibson, D. Rosen, and B. Stucker, *Additive Manufacturing Technologies*. New York, NY: Springer New York, 2015.

[24] N. N. Kumbhar and A. V. Mulay, “Post Processing Methods used to Improve Surface Finish of Products which are Manufactured by Additive Manufacturing Technologies: A Review,” *J. Inst. Eng. India Ser. C*, vol. 99, no. 4, pp. 481–487, Aug. 2018, doi: 10.1007/s40032-016-0340-z.

[25] “Multi-Tasking:What is Multi-Tasking?,” *mazakusa.com*. https://www.mazakusa.com/machines/process/multi-tasking/.

[26] F. Klocke and H. Wirtz, “Direct Manufacturing of Metal Prototypesand Prototype Tools,” *Franhofer Inst. Laser Technol.*, pp. 140–148, 1996.

[27] J. K. S. Nagel and F. W. Liou, “Hybrid Manufacturing System Design and Development,” *Manuf. Syst.*, pp. 223–224.
[28] “New Mazak VC-500 AM Combines 5-Axis and Additive Technology to Revolutionize Product Design,” *mazakusa.com*, Aug. 09, 2016. https://www.mazakusa.com/news-events/news-releases/new-mazak-vc-500-am-combines-5-axis-and-additive-technology/.
[29] “Mazak to Unveil HOT WIRE HYBRID Multi-Tasking Technology at IMTS 2018,” *mazakusa.com*, Jun. 18, 2018. https://www.mazakusa.com/news-events/news-releases/mazak-to-unveil-hot-wire-hybrid-multi-tasking-technology-at-imts-2018/.
[30] A. Trujillo and S. Luzik, “Additive Manufacturing and Combustible Dust Hazards in 3D Printing,” *EHS Today*, Mar. 12, 2018.
[31] R. Casati, J. Lemke, and M. Vedani, “Microstructure and Fracture Behavior of 316L Austenitic Stainless Steel Produced by Selective Laser Melting,” *J. Mater. Sci. Technol.*, vol. 32, no. 8, pp. 738–744, Aug. 2016, doi: 10.1016/j.jmst.2016.06.016.
[32] Y. M. Wang *et al.*, “Additively manufactured hierarchical stainless steels with high strength and ductility,” *Nat. Mater.*, vol. 17, no. 1, pp. 63–71, Jan. 2018, doi: 10.1038/nmat5021.
[33] S. Y. Wen, Y. C. Shin, J. Y. Murthy, and P. E. Sojka, “Modeling of coaxial powder flow for the laser direct deposition process,” *Int. J. Heat Mass Transf.*, vol. 52, no. 25–26, pp. 5867–5877, Dec. 2009, doi: 10.1016/j.ijheatmasstransfer.2009.07.018.
[34] A. G. Grigoryants, R. S. Tretyakov, I. N. Shiganov, and A. Ya. Stavertiy, “Optimization of the shape of nozzles for coaxial laser cladding,” *Weld. Int.*, vol. 29, no. 8, pp. 639–642, Aug. 2015, doi: 10.1080/01431161.2014.967043.
[35] I. Tabernero, A. Lamikiz, S. Martínez, E. Ukar, and L. N. López de Lacalle, “Modelling of energy attenuation due to powder flow-laser beam interaction during laser cladding process,” *J. Mater. Process. Technol.*, vol. 212, no. 2, pp. 516–522, Feb. 2012, doi: 10.1016/j.jmatprotec.2011.10.019.
[36] J. Lin, “Laser attenuation of the focused powder streams in coaxial laser cladding,” *J. Laser Appl.*, vol. 12, no. 1, pp. 28–33, Feb. 2000, doi: 10.2351/1.521910.
[37] J. Lin, “A simple model of powder catchment in coaxial laser cladding,” *Opt. Laser Technol.*, vol. 31, no. 3, pp. 233–238, Apr. 1999, doi: 10.1016/S0030-3992(99)00046-8.
[38] J. Mazumder and W. M. Steen, “Heat transfer model for cw laser material processing,” *J. Appl. Phys.*, vol. 51, no. 2, pp. 941–947, Feb. 1980, doi: 10.1063/1.327672.
[39] A. J. Pinkerton and L. Li, “An analytical model of energy distribution in laser direct metal deposition,” *Proc. Inst. Mech. Eng. Part B J. Eng. Manuf.*, vol. 218, no. 4, pp. 363–374, Apr. 2004, doi: 10.1243/095440504323055498.
[40] Y. Fu, A. Loredo, B. Martin, and A. B. Vannes, “A theoretical model for laser and powder particles interaction during laser cladding,” *J. Mater. Process. Technol.*, vol. 128, no. 1–3, pp. 106–112, Oct. 2002, doi: 10.1016/S0924-0136(02)00433-8.
[41] E. Toyskerani, A. Khajepour, and S. F. Corbin, *Laser Cladding*. 2004.
[42] W. F. Smith and J. Hashemi, *Foundations of Materials Science and Engineering*, 4th ed. McGraw-Hill, 2006.
[43] H. Taheri, “Powder-based additive manufacturing – a review of types of defects, generation mechanisms, detection, property evaluation and metrology,” p. 40.
[44] G. K. L. Ng, “Porosity formation and gas bubble retention in laser metal deposition,” *Appl. Phys. Mater. Sci. Process.*, vol. 97, no. 3, pp. 641–649, 2009.
[45] S. Barua and et al., “Vision-based defect detection in laser metal deposition process,” *Rapid Prototyp. J.*, vol. 20, no. 1, pp. 77–85, 2014.
[46] A. F. A. Hoadley, A. Frenk, and C. F. Marsden, *Surface engineering – processes and applications: A process overview of laser hardfacing*. Lancaster (USA): Technomic Publishing Company, Inc, 1995.
[47] F. C. Campbell, *Elements of Metallurgy and Engineering Alloys*. Materials Park, Ohio: ASM International, 2008.
[48] A. D. Dressler, E. W. Jost, J. C. Miers, D. G. Moore, C. C. Seepersad, and B. L. Boyce, “Heterogeneities dominate mechanical performance of additively manufactured metal lattice struts,” *Addit. Manuf.*, vol. 28, pp. 692–703, Aug. 2019, doi: 10.1016/j.addma.2019.06.011.
[49] M. Agarwala, D. Bourell, J. Beaman, H. Marcus, and J. Barlow, “Direct selective laser sintering of metals,” *Rapid Prototyp. J.*, vol. 1, no. 1, pp. 26–36, Mar. 1995.
[50] E. Chlebus, B. Kuźnicka, T. Kurzynowski, and B. Dybała, “Microstructure and mechanical behaviour of Ti—6Al—7Nb alloy produced by selective laser melting,” *Mater. Charact.*, vol. 62, no. 5, pp. 488–495, May 2011, doi: 10.1016/j.matchar.2011.03.006.

[51] D. Buchbinder, H. Schleifenbaum, S. Heidrich, W. Meiners, and J. Bültmann, “High Power Selective Laser Melting (HP SLM) of Aluminum Parts,” *Phys. Procedia*, vol. 12, pp. 271–278, 2011, doi: 10.1016/j.phpro.2011.03.035.
[52] J. P. Kruth, L. Froyen, J. Van Vaerenbergh, P. Mercelis, M. Rombouts, and B. Lauwers, “Selective laser melting of iron-based powder,” *J. Mater. Process. Technol.*, vol. 149, no. 1–3, pp. 616–622, Jun. 2004, doi: 10.1016/j.jmatprotec.2003.11.051.
[53] E. Chlebus, K. Gruber, B. Kuźnicka, J. Kurzac, and T. Kurzynowski, “Effect of heat treatment on the microstructure and mechanical properties of Inconel 718 processed by selective laser melting,” *Mater. Sci. Eng. A*, vol. 639, pp. 647–655, Jul. 2015, doi: 10.1016/j.msea.2015.05.035.
[54] T. R. Smith, J. D. Sugar, C. San Marchi, and J. M. Schoenung, “Orientation Effects on Fatigue Behavior of Additively Manufactured Stainless Steel,” in *Volume 6A: Materials and Fabrication*, Waikoloa, Hawaii, USA, Jul. 2017, p. V06AT06A020, doi: 10.1115/PVP2017-65948.
[55] R. Shrestha, J. Simsiriwong, and N. Shamsaei, “Fatigue behavior of additive manufactured 316L stainless steel parts: Effects of layer orientation and surface roughness,” *Addit. Manuf.*, vol. 28, pp. 23–38, Aug. 2019, doi: 10.1016/j.addma.2019.04.011.
[56] H. Alsalla, L. Hao, and C. Smith, “The Effect of Build Orientation on the Surface Quality, Microstructure and Mechanical Properties of Selective Laser Melting 316L Stainless Steel.” .
[57] N. Yang *et al.*, “Process-structure-property relationships for 316L stainless steel fabricated by additive manufacturing and its implications for component engineering,” p. 43.
[58] P. Guo, B. Zou, C. Huang, and H. Gao, “Study on microstructure, mechanical properties and machinability of efficiently additive manufactured AISI 316L stainless steel by high-power direct laser deposition,” *J. Mater. Process. Technol.*, vol. 240, pp. 12–22, Feb. 2017, doi: 10.1016/j.jmatprotec.2016.09.005.
[59] K. Zhang, S. Wang, W. Liu, and X. Shang, “Characterization of stainless steel parts by Laser Metal Deposition Shaping,” *Mater. Des.*, vol. 55, pp. 104–119, Mar. 2014, doi: 10.1016/j.matdes.2013.09.006.
[60] Z. Wang, T. A. Palmer, and A. M. Beese, “Effect of processing parameters on microstructure and tensile properties of austenitic stainless steel 304L made by directed energy deposition additive manufacturing,” *Acta Mater.*, vol. 110, pp. 226–235, May 2016, doi: 10.1016/j.actamat.2016.03.019.
[61] E. O. Olakanmi, R. F. Cochrane, and K. W. Dalgarno, “A review on selective laser sintering/melting (SLS/SLM) of aluminium alloy powders: Processing, microstructure, and properties,” *Prog. Mater. Sci.*, vol. 74, pp. 401–477, Oct. 2015, doi: 10.1016/j.pmatsci.2015.03.002.
[62] Y. Wang, H. Tang, Y. Fang, and H. Wang, “Microstructure and mechanical properties of hybrid fabricated 1Cr12Ni2WMoVNb steel by laser melting deposition,” *Chin. J. Aeronaut.*, vol. 26, no. 2, pp. 481–486, Apr. 2013, doi: 10.1016/j.cja.2013.02.027.
[63] P. L. Blackwell, “The mechanical and microstructural characteristics of laser-deposited IN718,” *J. Mater. Process. Technol.*, vol. 170, no. 1–2, pp. 240–246, Dec. 2005, doi: 10.1016/j.jmatprotec.2005.05.005.
[64] D. Zhang, W. Niu, X. Cao, and Z. Liu, “Effect of Standard Heat Treatment on the Microstructure and Mechanical Properties of Selective Laser Melting Manufactured Inconel 718 Superalloy,” *Mater. Sci. Eng.*, vol. A 644, p. 32, 2015.
[65] H. Kim, Z. Liu, W. Cong, and H.-C. Zhang, “Tensile Fracture Behavior and Failure Mechanism of Additively-Manufactured AISI 4140 Low Alloy Steel by Laser Engineered Net Shaping,” *Materials*, vol. 10, no. 11, p. 1283, Nov. 2017, doi: 10.3390/ma10111283.
[66] Y. Xiong, W. Zhuang, and M. Zhang, “Effect of the thickness of cold sprayed aluminium alloy coating on the adhesivebondstrengthwithanaluminiumalloysubstrate,” *Surf Coat Technol*, no. 270, pp. 259–265, 2015.
[67] K. Zhang, W. Liu, and X. Shang, “Research on the processing experiments of laser metal deposition shaping,” *Opt Laser Technol*, vol. 39, pp. 549–557, 2007.
[68] A. Frenk, M. Vandyoussefi, J. D. Wagniere, W. Kurz, and A. Zryd, “Analysis of the Laser-Cladding Process for Stellite on Steel,” *Metall. Mater. Trans.*, vol. B 28, no. 3, pp. 501–508, 1997.
[69] M. Wolf, “Improving the Efficiency of the DMLD Process: How particle size and laser spot size influence process quality and efficiency,” *Laser Tech. J.*, vol. 13, no. 4, pp. 32–34, Sep. 2016, doi: 10.1002/latj.201600028.
[70] U. de Oliveira, V. Ocelík, and J. Th. M. De Hosson, “Analysis of coaxial laser cladding processing conditions,” *Surf. Coat. Technol.*, vol. 197, no. 2–3, pp. 127–136, Jul. 2005, doi: 10.1016/j.surfcoat.2004.06.029.
[71] R. J. Urbanic, S. M. Saqib, and K. Aggarwal, “Using Predictive Modeling and Classification Methods for Single and Overlapping Bead Laser Cladding to Understand Bead Geometry to Process Parameter Relationships,” *J. Manuf. Sci. Eng.*, vol. 138, no. 5, p. 051012, May 2016, doi: 10.1115/1.4032117.
[72] M. Schneider, “LASER CLADDING WITH POWDER,” p. 177.

[73] S. Zanzarin, “Laser Cladding with metallic powders,” University of Trento-Italy, 2015.
[74] S. M. Saqib, “Experimental Investigation of Laser Cladding Bead Morphology and Parameter Relationship for Additive Manufacturing Process Characterization,” University of Windsor, 2016.
[75] E. Díaz, J. M. Amado, J. Montero, M. J. Tobar, and A. Yáñez, “Comparative Study of Co-based Alloys in Repairing Low Cr-Mo steel Components by Laser Cladding,” *Phys. Procedia*, vol. 39, pp. 368–375, 2012, doi: 10.1016/j.phpro.2012.10.050.
[76] Y.-X. Li, P.-F. Zhang, P.-K. Bai, Z.-Y. Zhao, and B. Liu, “Analysis of Geometrical Characteristics and Properties of Laser Cladding 85 wt.% Ti + 15 wt.% TiBCN Powder on 7075 Aluminum Alloy Substrate,” *Materials*, vol. 11, no. 9, p. 1551, Aug. 2018, doi: 10.3390/ma11091551.
[77] M. Picasso, C. F. Marsden, J. D. Wagniere, A. Frenk, and M. Rappaz, “A simple but realistic model for laser cladding,” *Metall. Mater. Trans. B*, vol. 25, no. 2, pp. 281–291, Apr. 1994, doi: 10.1007/BF02665211.
[78] E. Toyserkani, A. Khajepour, and S. Corbin, “3-D finite element modeling of laser cladding by powder injection: effects of laser pulse shaping on the process,” *Opt. Lasers Eng.*, vol. 41, no. 6, pp. 849–867, Jun. 2004, doi: 10.1016/S0143-8166(03)00063-0.
[79] E. Toyserkani, A. Khajepour, and S. Corbin, “Recurrent neural network based analysis for laser cladding dynamic model identification,” in *International Congress on Applications of Lasers & Electro-Optics*, Scottsdale, Arizona, USA, 2002, p. 160610, doi: 10.2351/1.5066137.
[80] E. Toyserkani, A. Khajepour, and S. Corbin, “Application of experimental-based modeling to laser cladding,” *J. Laser Appl.*, vol. 14, no. 3, pp. 165–173, Aug. 2002, doi: 10.2351/1.1494079.
[81] R. Colaço, L. Costa, R. Guerra, and R. Vilar, “A Simple Correlation Between the Geometry of Laser Cladding Tracks and the Process Parameters,” in *Laser Processing: Surface Treatment and Film Deposition*, J. Mazumder, O. Conde, R. Villar, and W. Steen, Eds. Dordrecht: Springer Netherlands, 1996, pp. 421–429.
[82] H. El Cheikh, B. Courant, S. Branchu, J.-Y. Hascoët, and R. Guillén, “Analysis and prediction of single laser tracks geometrical characteristics in coaxial laser cladding process,” *Opt. Lasers Eng.*, vol. 50, no. 3, pp. 413–422, Mar. 2012, doi: 10.1016/j.optlaseng.2011.10.014.
[83] P. Farahmand and R. Kovacevic, “Parametric Study and Multi-Criteria Optimization in Laser Cladding by a High Power Direct Diode Laser,” *Lasers Manuf. Mater. Process.*, vol. 1, no. 1–4, pp. 1–20, Dec. 2014, doi: 10.1007/s40516-014-0001-0.
[84] G. C. Onwubolu, J. P. Davim, C. Oliveira, and A. Cardoso, “Prediction of clad angle in laser cladding by powder using response surface methodology and scatter search,” *Opt. Laser Technol.*, vol. 39, no. 6, pp. 1130–1134, Sep. 2007, doi: 10.1016/j.optlastec.2006.09.008.
[85] P. Alvarez, M. Á. Montealegre, J. F. Pulido-Jiménez, and J. I. Arrizubieta, “2 Analysis of the process parameter influence in laser 3 cladding of 316L stainless steel,” p. 11, 2018.
[86] R. L. Keeney, “Common Mistakes in Making Value Trade-Offs,” *Oper. Res.*, vol. 50, no. 6, pp. 935–945, Dec. 2002, doi: 10.1287/opre.50.6.935.357.
[87] B. C. Salzbrenner *et al.*, “High-throughput stochastic tensile performance of additively manufactured stainless steel,” *J. Mater. Process. Technol.*, vol. 241, pp. 1–12, Mar. 2017, doi: 10.1016/j.jmatprotec.2016.10.023.
[88] L. Carter, C. Martin, P. Withers, and M. Attallah, “The influence of the laser scan strategy on grain structure and cracking behaviour in SLM powder-bed fabricated nickel superalloy,” *J. Alloys Compd.*, vol. 615, pp. 338–347, Dec. 2014.
[89] D. R. Leuser, C. K. Syn, and O. D. Sherby, “Nano-subgrain strengthening in ball-milled iron,” *Mater. Sci. Eng. A*, no. 463, pp. 54–60, 2007, doi: 10.1016/j.msea.2006.07.161.
[90] T. Kurzynowski, K. Gruber, W. Stopyra, B. Kuźnicka, and E. Chlebus, “Correlation between process parameters, microstructure and properties of 316 L stainless steel processed by selective laser melting,” *Mater. Sci. Eng. A*, vol. 718, pp. 64–73, Mar. 2018, doi: 10.1016/j.msea.2018.01.103.
[91] P. Susan and R. Brooks, “Porosity in Stainless Steel LENS Powders and Deposits,” presented at the International Solid Freeform Fabrication Symposium, 2000, p. 8.
[92] H. V. Atkinson and S. Davies, “Fundamental aspects of hot isostatic pressing: An overview,” *Metall. Mater. Trans. A*, vol. 31, no. 12, pp. 2981–3000, 2000, doi: 10.1007/s11661-000-0078-2.